Ph.D. Thesis, PhD no. 000699

Electrohydrodynamic aspects of two-fluid microfluidic systems: theory and simulation

Goran Goranović

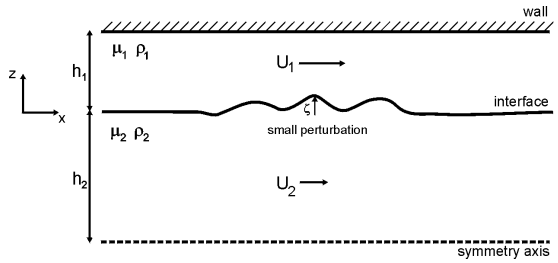

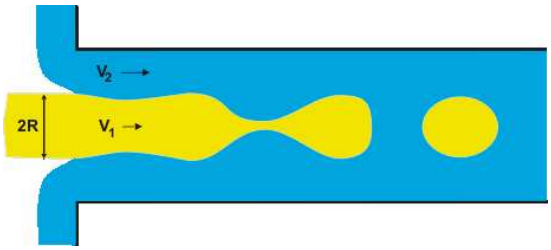

Supervisor: Henrik Bruus

Mikroelektronik Centret (MIC)
Technical University of Denmark

15 August 2003

Abstract

The goal of this thesis has been to explore fundamental theoretical principles behind micro Total Analysis Systems (μTAS), also known as lab-on-a-chip systems, as well as to make use of computer simulations as an evaluation technique in the process of developing and optimizing μTAS devises. This involves fundamental physics and computer science as well as interpreting experimental input provided by others.

Most of the work has been documented in 4 peer reviewed papers, 7 conference proceedings, one chapter in a text book, and one patent. The results comprise simulations of the two-liquid chimney device and the cascade EO-pump, discovery of how to pump non-polar liquids by electroosmosis, theory of clogging pressures of large bubbles in microchannel contractions, and a theoretical analysis of the stability conditions for the interface between two different dielectric liquids under influence of external electric fields.

A significant effort has been devoted to the creation of a new group at MIC, the Microfluidcs Theory and Simulation Group (MIFTS). During the first year of this PhD-study, simulation of lab-on-a-chip systems was the main topic. Later, as students were attracted to the group the activities expanded to include the theoretical studies. At present MIFTS consists of two postdocs, four PhD students and a number of undergraduate students, under the leadership of prof. Henrik Bruus.

Resumé

Målet med dette ph.d.-studium har været at undersøge fundamentale teoretiske principper bag lab-on-a-chip systemer og at benytte computer simulationer til hjælp for udviklingen og optimeringen af sådanne systemer. Studierne har især været koncentreret om mikropumper baseret på elektroosmose, dynamikken af gasbobler i mikrokanaler samt stabilitetsundersøgelser af skillefladen mellem to dielektriske væsker under påvirkning af ydre elektriske felter.

Det meste af arbejdet er blevet publiceret internationalt i løbet af studiet i form af 4 forskningsartikler, 7 konferenceartikler, 1 patent, og 1 kapitel i en lærebog. Især to hovedresultater kan fremhæves. Det første er den nu patenterede opdagelse af hvorledes elektroosmose i en særligt designet to-væske mikropumpe kan benyttes til at pumpe ikkepolære væsker. Det andet er påvisningen af hvorledes selv moderate elektriske spændingsforskelle i mikrofluide to-væske systemer kan føre til instabiliteter, et fænomen som ikke iagttages i makrosystemer. Hertil kommer en række analyser og simuleringer af forskellige konkrete mikrofluide systemer, som kolleger har fabrikeret og målt på.

Endelig skal det fremhæves, at meget arbejde i løbet studiet er blevet brugt på at bidrage til etableringen af MIC's nye gruppe, Microfluidics Theory and Simulation (MIFTS). I dag fremstår MIFTS som en velfungerende gruppe med to postdocs, fire ph.d.-studerende og et antal ingeniørstuderende under ledelse af lektor Henrik Bruus.

Preface

The present thesis is one of the requirements for obtaining the PhD degree from the Technical University of Denmark (DTU). The PhD program has been completed during the period 1 May 2000 - 15 Aug 2003 at Mikroelektronik Centret, MIC.

The first half of the PhD program was conducted within the μTAS group mainly with regard to the applications, and the second half was finalized within the MIFTS group mainly with regard to theory.

My engagement began in early 2000 as the need for simulation efforts arose in the multidisciplinary project assigned to develop lab-on-chip platform in Denmark. At the time, there were no similar efforts done at the institute, so many different areas in both theory and experiment needed to be initiated from the beginning. It was an exciting and on occasions tough experience but most of all nicely unpredictable. In the meantime, both of the groups have developed significantly.

Many people have contributed in supporting me on the way and I am using this occasion to thank them. I would also like to thank my first supervisor Jörg Kutter for giving the necessary support and "open hands" in the first part of the studies. I would then express my gratitude to my second and current supervisor Henrik Bruus for the tremendous help, patience and enthusiasm that he provided in the critical stages of the studies. A special acknowledgement deserve my resourceful master students (Anders, Flemming, Lennart, and Mads - the "four aces") whom I co-supervised during 2001/2002.

Finally, I would like to thank my family, friend Ivana and girlfriend Helle for their non-wavering faith and support throughout the period.

Goran Goranović
Mikroelektronik Centret (MIC)
Technical University of Denmark
15 August 2003

Contents

List of figures **xiv**

List of tables **xv**

1 Introduction **1**
1.1 Publications during the project . . . 2
1.1.1 Research papers . . . 2
1.1.2 Conference proceedings . . . 2
1.1.3 A chapter in a text book . . . 3
1.1.4 Co-supervision of four M.Sc. theses . . . 3

2 Aspects of microfluidics **5**
2.1 Descriptive overview of microfluidic systems . . . 5
2.2 The Continuum Hypothesis . . . 8
2.3 Conservation of mass and momentum . . . 9
2.4 Conservation of energy . . . 9
2.5 Electrostatic fields . . . 10
2.6 Reynolds and Bond number . . . 10

3 Electroosmotic driven microflows **13**
3.1 The Electric Double Layer . . . 13
3.2 Thickness λ_D of the Double layer . . . 14
3.3 The Electric Potential . . . 16
3.4 The Helmholtz-Smoluchowski velocity . . . 18
3.5 The Zeta Potential . . . 20
3.6 Flow in a Circular Capillary . . . 22

4 Simulations of interfaces in two-fluid systems **25**
4.1 Miscible streams in micro cell sorters . . . 25
4.2 Bubbles in microchannels . . . 26
4.2.1 Formation of bubbles . . . 26
4.2.2 Clogging of microchannels . . . 28
4.2.3 Passive bubble trap . . . 29
4.3 Two-liquid viscous pump . . . 30

4.3.1 Submerged jets . . . 30
4.3.2 EOF induced viscous drag . . . 30
4.3.3 Instability problem . . . 31

5 Fluid dielectrics and the Maxwell stress tensor 35
5.1 The Maxwell stress tensor in free space . . . 35
5.2 Fluid dielectrics in electric field . . . 38
5.2.1 The internal and the free energy of a dielectric . . . 38
5.2.2 The Maxwell stress tensor in fluid dielectrics . . . 40
5.2.3 Electric force in fluid dielectrics . . . 41
5.2.4 Alternative form of the force density . . . 43
5.2.5 The boundary between two dielectrics . . . 44

6 Hydrodynamic stability analysis: basics 47
6.1 General concepts . . . 48
6.2 Standard procedure in linear stability analysis . . . 50
6.3 Example: The Rayleigh-Taylor instability . . . 52
6.3.1 A note on viscosity . . . 54

7 Interfaces in electrohydrodynamics: theory 57
7.1 Two immiscible liquids between infinite planes . . . 57
7.1.1 The governing equations . . . 59
7.1.2 General boundary conditions: rigid boundaries . . . 59
7.1.3 General boundary conditions: the interface . . . 60
7.2 Perturbation equations and boundary conditions . . . 61
7.2.1 The stationary solution for still liquids . . . 61
7.2.2 Linearization of the perturbed equations . . . 62
7.2.3 Linearization of the perturbed boundary conditions . . . 63
7.2.4 Expansion into normal modes . . . 66
7.2.5 Summary of solutions and linearized boundary conditions . . . 67

8 Interfaces in electrohydrodynamics: applications in microfluidics 71
8.1 Zero viscosity and perpendicular E-field . . . 71
8.1.1 Dispersion relation $\omega(\mathbf{k})$: general case . . . 72
8.1.2 The onset of instability: limiting cases for infinite planes . . . 75
8.1.3 The onset of instability: general case for infinite planes . . . 78
8.1.4 Instability voltages for infinite planes, $kL \gg 1$ (macrofluidic limit) . . . 80
8.1.5 Instability voltages for infinite planes, $kL \ll 1$, (microfluidic limit) . . . 80
8.1.6 Finite-size effect on instability in microfluidics . . . 81
8.1.7 Instability voltages in microfluidic channels . . . 83
8.1.8 Low aspect-ratio microchannels, $L_y \gg L_0$ . . . 85
8.2 Zero viscosity and parallel E-field . . . 86

9 Conclusion 87
9.1 Outlook . . . 88

A Paper published in J. Micromech. Microeng. 91

B Paper published in Sens. Actuators B Chem. 101

C Paper published in J. Micromech. Microeng. 109

D Paper published in Proc. microTAS 2002 119

E Paper published in Proc. NanoTech 2003 123

F Book chapter published by Wiley-VCH 2003 129

Bibliography 131

List of Figures

2.1 Integrated-chemiluminescence-detector chip 6
2.2 The race-track effect 7

3.1 The structure of an electric double layer. 14
3.2 Electric potentials in a circular channel and between parallel plates. 18
3.3 EOF and the electric field. 20
3.4 Structure of the electric potential in the double layer. 21
3.5 Chemical reactions for silanol groups. 21

4.1 Micro cell sorter 26
4.2 Micro cell-sorter 27
4.3 Sudden and tapered channel constrictions 28
4.4 Passive bubble trap 29
4.5 Viscous-drag pumps 31
4.6 Two-liquid viscous pump: our new design 32
4.7 Two-liquid viscous pump: simulation 33

5.1 Normal and tangential electric stresses 36
5.2 Interface between two liquid dielectrics 44

6.1 Potential energy of a conservative system 48
6.2 Instability of a bent rectangular beam 49
6.3 Two liquids between infinite planes 52
6.4 The Rayleigh-Taylor (gravitational) instability 54

7.1 Instabilities in electrohydrodynamics 58
7.2 Interface perturbations in normal and tangential **E**-field 60

8.1 Instability: phase velocities and frequencies 75
8.2 Instability: dependency on We_{el} and Bo 77
8.3 The onset of instability as function of Bo 79
8.4 Two liquids in finite size microfluidic channels 82
8.5 Instability voltages in finite microchannels - small and large k 84
8.6 Instability voltage in finite size channels - general case. 85
8.7 Vertically superposed layers in a low-aspect-ratio microchannel. 86

List of Tables

4.1 Comparison between the circuit model and a CFD simulation 33

8.1 Parameters for the oil-water system 72

In Chap. 6 basics of hydrodynamic stability analysis are presented with a simple example of gravitational instability.

In Chap. 7 linear stability theory is applied to the problem of stability of the interface between two still, immiscible dielectrics placed in an electric field (normal or tangential). The chapter contains full derivation of the linearized perturbed equations of motion and boundary conditions.

Chap. 8 presents the solutions of the equations derived in Chap. 7 applied to the cases of normal and tangential **E**-fields. The interface instability is discussed with respect to two microfluidic cases where either one or two characteristic lengths are of micron dimensions.

Chap. 9 concludes the report and outlines the future directions.

Finally, the most relevant publications have been attached in the Appendix.

1.1 Publications during the project

The following list comprises all of the publications that I have contributed to during my PhD study at MIC.

1.1.1 Research papers

1. *PIV measurements in a microfluidic 3D-sheathing structure with three-dimensional flow behavior*,
   Henning Klank, Goran Goranović, Jörg P. Kutter, Henrik Gjelstrup, Jess Michelsen, Carsten Westergaard,
   J. Micromech. Microeng. **12**, 862-869 (2002).

2. *Integrating advanced functionality in a microfabricated high-throughput flourescent-activated cell sorter*,
   A. Wolff, I.R. Perch-Nielsen, U.D. Larsen, P. Friis, G. Goranović, C.R. Poulsen, J.P. Kutter, P. Telleman,
   Lab. Chip **3**, 22-27 (2003).

3. *Theoretical analysis of the low-voltage cascade electroosmotic pump*,
   Anders Brask, Goran Goranović, and Henrik Bruus,
   Sens. Actuators B Chem. **92**, 127-132 (2003).

4. *The clogging pressure of bubbles in hydrophilic microchannel contractions*,
   Mads Jakob Jensen, Goran Goranović, and Henrik Bruus,
   J. Micromech. Microeng. 14 (2004), (8 pages, www.mic.dtu.dk/research/MIFTS)

1.1.2 Conference proceedings

5. *Three-dimensional single step flow sheathing in micro cell sorters*,
   Goran Goranović, Ivan R. Perch-Nielsen, Ulrik D. Larsen, Anders Wolff, Jörg P. Kutter, Pieter Telleman,
   Proc. MSM 2001, Hilton Head Island (SC) USA, March 2001, p. 242-245.

6. *Computer modeling as a design tool for microfluidic structures*,
Ivan R. Perch-Nielsen, Goran Goranović, Henning Klank, Ulrik D. Larsen, Anders Wolff, Jörg P. Kutter, Pieter Telleman,
Proc. MSM 2001, Hilton Head Island (SC) USA, March 2001, p. 629-630.

7. *Characterization of flows in laser-machined polymeric microchannels*,
Goran Goranović, Henning Klank, Carsten Westergaard, Oliver Geschke, Pieter Telleman, and Jörg P. Kutter,
Proc. μTAS 2001, Monterey (CA) USA, October 2001.

8. *Electroosmotically driven two-liquid viscous pump for nonconducting liquids*,
Anders Brask, Goran Goranović, and Henrik Bruus,
Proc. μTAS 2002, Nara, Japan, November 2002, vol. **1**, p. 45-47.

9. *The low-voltage cascade EOF pump: comparing theory with published data*,
Anders Brask, Goran Goranović, and Henrik Bruus,
Proc. μTAS 2002, Nara, Japan, November 2002, vol. **1**, p. 79-81.

10. *Dynamics of bubbles in microchannels*,
Mads Jakob Jensen, Goran Goranović, and Henrik Bruus,
Proc. μTAS 2002, Nara, Japan, November 2002, vol. **2**, p. 733-735.

11. *Electroosmotic pumping of nonconducting liquids by viscous drag from a secondary conducting liquid*,
Anders Brask, Goran Goranović, and Henrik Bruus,
Proc. NanoTech 2003, San Francisco (CA) USA, March 2003, vol. **1**, p. 190-193.

12. *Quasi-static motion of bubbles in microchannel contractions*,
Mads Jakob Jensen, Goran Goranović, and Henrik Bruus,
Proc. NanoTech 2003, San Francisco (CA) USA, March 2003, vol. **1**, p. 258-261.

1.1.3 A chapter in a text book

13. *Simulations in microfluidcs*
Goran Goranović and Henrik Bruus,
Chap. 5 (38 pages, 21 figs., 25 refs.) in *Microsystem Engineering of Lab-on-a-Chip Devices*. Eds. O. Geschke, H. Klank, and P. Telleman, (Wiley-VCH, New York, autumn 2003)

1.1.4 Co-supervision of four M.Sc. theses

- *Principles of electroosmotic pumps*
Anders Brask
M.Sc. thesis, 156 pages, MIC, DTU, 2002 (www.mic.dtu.dk/research/MIFTS)

- *Bubbles in microchannels*
Mads Jakob Jensen
M.Sc. thesis, 155 pages, MIC, DTU, 2002 (www.mic.dtu.dk/research/MIFTS)

- *Blood flow in microchannels*
  Lennart Bitsch
  M.Sc. thesis, 111 pages, MIC, DTU, 2002 (www.mic.dtu.dk/research/MIFTS)

- *Dispersion in electrokinetically and pressure driven microflows*
  Flemming Rytter Hansen
  M.Sc. thesis, 121 pages, MIC, DTU, 2002 (www.mic.dtu.dk/research/MIFTS)

Chapter 2

Aspects of microfluidics

In this chapter we give important aspects of microfluidics.

2.1 Descriptive overview of microfluidic systems

This section is adapted from my text-book chapter *Simulations in Microfluidics*[13]. When designing new microfluidic devices, one must have a proper understanding of the physical aspects of the problem. Some of these are given below.

- **Dimensions**
  A microfluidic system is a network of fluidic channels and other components such as valves and pumps. It typically occupies an area of one square centimeter, with the typical channel widths on the order of 10 - 100 μm. For comparison, a human hair has a thickness of approximately 50 μm and the diameter of red blood cells are about 7 μm. From a practical point of view even smaller dimensions in a lab-on-a-chip are not necessarily advantageous, since the requirement for easier handling as well as measurements can impose some restrictions. However, if the goal is to develop systems for single molecule detection, the sub-micrometer is unavoidable, and one enters the new and exciting field of nanofluidics.

- **Geometry**
  The basic component in a microfluidic network is a channel. Main features include length, cross-section and surface properties such as roughness. After a channel is made in a substrate it is covered with a bonded lid that can be made from a different material. Long channels are usually needed if a reaction of several mixed chemicals is to occur (in laminar flow regime diffusion is the main mixing mechanism and it takes time). Also, when a chemical compound consisting of several components needs to be analyzed, usually by electrical separation techniques, the separation channel is made longer in order to allow for the proper separation of the components. Since microchips are confined to a small area, the extra length is achieved by meander or spiral structures, Fig. 2.1. Such channel bending, however, induces dispersion of

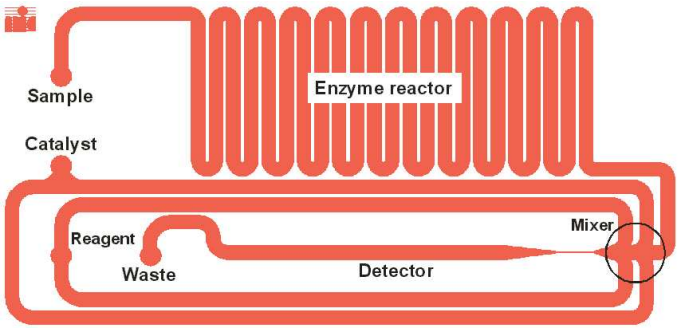

Figure 2.1: (a) A mask of an integrated microsystem for detecting chemical reactions via chemiluminescence. Before entering the mixing region, a sample is passed through the long spiral for a prolonged reaction with immobilized enzyme. Then, a product, usually H_2O_2, is entering the mixing region and in catalyzed reaction with reagent produces light. Back-side photodiodes, used for the light detection, are not shown. The dimensions of the chip are 20 mm $\times$ 10 mm, and width of the enzyme reactor is 400 μm. Courtesy of A. M. Jørgensen.

a chemical species since molecules travel different distances inside the turn (race-track effect, Fig. 2.2. The dispersion lowers the concentration resulting in reduced resolution, i.e. larger overlaps of the concentration peaks, and diminished detection signals. Another common source of the geometrical dispersion are interconnections, such as tubings, between a chip and external liquid reservoirs.
Channels can have different cross-sections depending on the material in which they are embedded. In silicon, the typical profiles are rectangular, or actually slightly trapezoid due to underetching. In polymers, laser beams can produce rectangular, triangular and Gaussian-like shapes. Circular cross-sections as in capillaries are also encountered. In addition, channels can have various degrees of surface roughness depending on the fabrication process. Geometrical features are important since they determine the characteristic resistances of a channel. The hydraulic resistance, a concept used in the uniform flow regime, relates an applied pressure to the corresponding flow rate, while the electrical resistance of a channel filled with a conducting liquid relates an applied voltage to the passing current.

- **Surface**
  Chemical groups at the surface of channel walls, such as silanol (SiOH) groups in glass, can react with the ions in an electrolyte solution and create very thin polarized layer. This electric double layer, or Debye layer, has a length scale of 1-10 nm and is responsible for electroosmotic flow (EOF) in an applied electric field. Surface double-layers are characterized by the zeta potential. Different surfaces, such as the lid and the bottom of a channel, can have different zeta potentials. The characteristic EOF velocity depends on the zeta potential through electroosmotic mobility which is largely an empirical value.

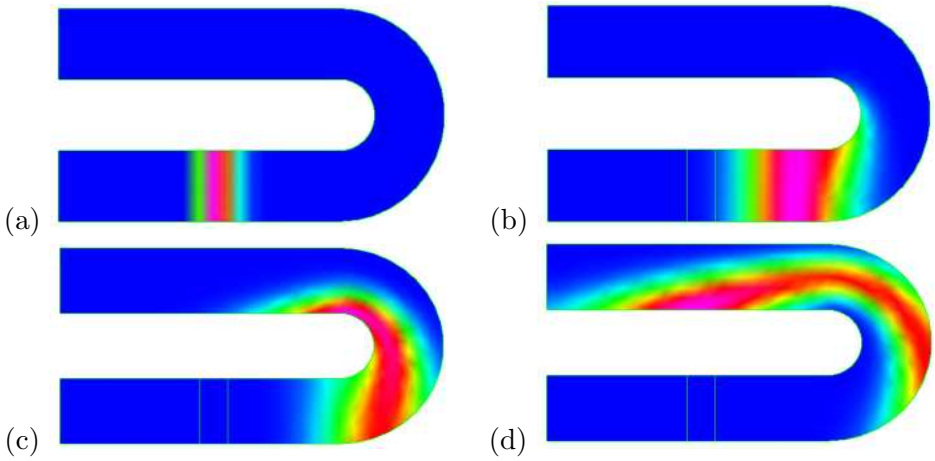

Figure 2.2: The race-track effect in a turn in an electrokinetically driven flow, with a voltage ∼10 V applied at the ends. The width of the channel is 50 μm. The motion starts at the top left figure and goes clockwise. The concentration contours of a sample are displayed, obtained from a simulation. The inside track has shorter path as well as higher electrical field inducing faster movement of the inner molecules, and therefore enhancing sample dispersion.

- **Fluid properties**
  The channels are filled with liquids which can have different properties such as density, viscosity, electrical and thermal conductivity, diffusion coefficients, surface tension etc. In many cases there are two types of liquids in the system - a buffer and a sample. The buffer is usually the transporting liquid resisting the changes in pH-value which can for example be induced close to electrodes or in chemical reactions. A sample is a liquid of interest which needs to be analyzed. Both buffer and sample are usually placed on the chip through separate reservoirs, with the buffer finally surrounding the sample. A sample confined to a specific region is called a sample plug. In separation science, the sample consists of several chemical species such as a positively charged, a negatively charged and a neutral. As mentioned above, the sample plug lowers its initial concentration by dispersing through the system. In addition to the geometrical constrictions, dispersion is caused by velocity profiles, such as the parabolic in the pressure driven flows, and by diffusion. Fluids such as blood or gels are so-called non-Newtonian liquids, for which the viscosity is not constant but is a function of the local shear stress. Since the shear stresses are pronounced at the walls more than in the middle of the channels, the resulting flow profile is a blunted one rather than the usual parabolic one.

- **Heating**
  Joule heating is generated when an electrical current flows through a channel. In some applications such heating may destroy biological samples. It may also induce changes in viscosity and thus affect the velocity profile. Moreover, due to enhanced

the Brownian motion, heating may increase the dispersion of a sample plug. Heating may also increase the mobility of the ions in electric double layers leading to enhanced flow rates in electroosmotic flows. Finally, heating will stimulate production of bubbles of the gases dissolved in the liquid. The bubbles are usually unwanted and can block the flow if getting stuck in narrow contractions.

2.2 The Continuum Hypothesis

In this thesis all fluids discussed are Newtonian and are generally treated as continuous isotropic matter (mean molecular fields). The continuum description could however be questioned because of the small length scales present in microfluidics.

A way of defining deviations from the continuum description is through the Knudsen number [58]

$$Kn = \frac{\lambda}{L}, \tag{2.1}$$

where λ is the mean-free-path of the molecules and L is a characteristic length scale. L should be chosen to include gradients in the velocity field. For liquids λ is approximately the intermolecular length L_{mol} (bond length). The volume occupied by one molecule L_{mol}^3 is easily approximated, yielding

$$L_{\text{mol}} = \left(\frac{M_{\text{mol}}}{\rho N_A}\right)^{1/3}, \tag{2.2}$$

where ρ is the density, M_{mol} the molar mass, and N_A is Avogado's number. For water $\lambda = L_{mol} \approx 0.31$nm. The Knudsen number identifies the continuum regimes and the governing equations.[1]

A more intuitive way of justifying the use of the continuum approximation is through a precision criterion. At sufficiently high precision fluids are never continuous. The concept of a continuous velocity field does, e.g., only makes sense for small changes in the center of mass, of a small characteristic volume, due to random fluctuations in velocities. Another example could be to determine the mass density to a certain relative precision r.

- **Example**
  Determining the mass density $\rho = mN/V$ to the relative precision r, with N the number of molecules of mass m in a small volume V. There are only fluctuations in the relative number of molecules ΔN due to random walk which is typically $\Delta N \approx \sqrt{N}$. For $r = 1\%$ the requirement $\Delta N/N < r$ yields $N > 1/r^2 = 10^4$. The given volume hence needing dimensions $L > 22L_{\text{mol}}$. For the case of water $L > 7$nm which is a factor 10^3 smaller than the geometric dimensions of the microfluidic systems analyzed in this thesis.

[1] For $0 < Kn < 0.01$ the continuum approximation is applicable and the Navier-Stokes equation usable, this regime is generally in use in microfluidic flows. For $0.01 < Kn < 0.1$ the Navier-Stokes equation is still applicable however with use of so-called slip conditions to account for microscopic phenomenon at solid boundaries.

2.3 Conservation of mass and momentum

Let us consider a volume V on which external forces f act. The equations of motion can be derived by considering the flow of fluid out of the volume, Landau-Lifshitz [14]. Integral conservation laws of mass and momentum are respectively

$$\frac{d}{dt}\int_V \rho \, dV + \int_S \rho \mathbf{u}\cdot\mathbf{n} \, dS = 0, \tag{2.3}$$

$$\frac{d}{dt}\int_V \rho\mathbf{u} \, dV + \int_S [\rho\mathbf{u}(\mathbf{u}\cdot\mathbf{n}) - \tau'\mathbf{n}] \, dS = \int_V f \, dV, \tag{2.4}$$

where $\mathbf{u}(x,y,z,t) = (u,v,w)$ is the velocity field, ρ is mass density and $\mathbf{n}$ a normal vector directed out of the volume. For Newtonian fluids the stress tensor τ' is

$$\tau'_{ik} = -p\delta_{ik} + \tau_{ik}, \tag{2.5}$$

where the normal component p is pressure and τ the viscous stress tensor

$$\tau_{ik} = \mu\left(\partial_k u_i + \partial_i u_k\right) + (\lambda - \frac{2}{3}\mu)\partial_l u_l \delta_{ik}. \tag{2.6}$$

The scalars μ and λ are called coefficients of viscosity.

By applying Gauss' theorem to Eqs. (2.3) and (2.4) we obtain the equation of continuity and the Navier-Stokes equation

$$\frac{D\rho}{Dt} = -\rho\boldsymbol{\nabla}\cdot\mathbf{u}, \tag{2.7}$$

$$\rho\frac{D\mathbf{u}}{Dt} = -\boldsymbol{\nabla}p + \boldsymbol{\nabla}\cdot\tau + \mathbf{f}, \tag{2.8}$$

with $D/Dt = \partial_t + \mathbf{u}\cdot\boldsymbol{\nabla}$ being the convective derivative.

In case of incompressible fluids $D\rho/Dt = 0$ and Eqs. (2.7) and (2.8) simplify to

$$\boldsymbol{\nabla}\cdot\mathbf{u} = 0, \tag{2.9}$$

$$\rho\frac{D\mathbf{u}}{Dt} = -\boldsymbol{\nabla}p + \mu\nabla^2\mathbf{u} + \mathbf{f}. \tag{2.10}$$

while the viscous stress tensor becomes

$$\tau_{ik} = \mu\left(\partial_k u_i + \partial_i u_k\right). \tag{2.11}$$

2.4 Conservation of energy

In viscous flows the energy is dissipated through irreversible processes into heat. The temperature of the system will increase until an equilibrium between heat generation and heat transport is obtained. The conservation of energy is given by, Landau-Lifshitz, [14],

$$\partial_t\Big(\frac{1}{2}\rho u^2 + \rho e\Big) = -\boldsymbol{\nabla}\cdot\left[\rho\mathbf{u}(\frac{1}{2}u^2 + h) - \mathbf{u}\cdot\tau - \kappa\boldsymbol{\nabla}T\right], \tag{2.12}$$

Here e and h are respectively internal energy and enthalpy per unit mass, $\kappa(T)$ thermal conductivity and T temperature. The left hand side of Eq. (2.12) is the rate of change in mechanical and thermal energy respectively, while the right hand side is the divergence of the energy flux. The first term in the brackets represents the mass transfer due to the fluid motion (kinetic energy $\rho u^2/2$ and enthalpy ρh, per unit volume); the second term is the internal friction due to the viscosity. The last term represents the heat conduction due to temperature gradients.

The thermodynamic relations for e and h are

$$de = Tds - pdV = Tds + \frac{p}{\rho^2}d\rho, \tag{2.13}$$

$$dh = Tds + Vdp = Tds + \frac{1}{\rho}dp, \tag{2.14}$$

s being the entropy per unit mass and $V = 1/\rho$ specific volume. If these expressions are used together with the continuity and momentum equations, Eq. (2.12) can be transformed into the equation of heat transfer, [14]

$$\rho\frac{Dq}{Dt} = \Psi + \boldsymbol{\nabla}\cdot(\kappa\boldsymbol{\nabla}T), \tag{2.15}$$

Left side of Eq. (2.15) represents the amount of heat gained per unit volume. The term Ψ

$$\Psi = \tau\cdot\boldsymbol{\nabla}\mathbf{v} \tag{2.16}$$

is called the dissipation function and gives the amount of energy dissipated into heat by viscosity. It is always positive and for incompressible fluids equal to

$$\Psi = \mu\frac{1}{2}(\partial_k u_i + \partial_i u_k)^2. \tag{2.17}$$

2.5 Electrostatic fields

In the thesis we will treat phenomena where only electrostatic fields are applied. When external magnetic fields are absent, magnetic effects can be completely ignored, [15]. Maxwell equations for electric fields reduce to

$$\boldsymbol{\nabla}\cdot\mathbf{D} = \rho^e, \tag{2.18}$$

$$\boldsymbol{\nabla}\times\mathbf{E} = 0, \tag{2.19}$$

where $\mathbf{D} = \epsilon\mathbf{E}$ is the electric displacement vector. Thorough discussion of the electric forces in dielectrics will be made in Chap. 5.

2.6 Reynolds and Bond number

A measure for the ratio between inertial and viscous forces is the Reynolds number defined as

$$Re = \frac{L\ u}{\nu}, \tag{2.20}$$

where L and u is a characteristic length and velocity, respectively. The Reynolds number at the transition between laminar and turbulent flow is of the order 10^3, depending on the geometry and type of flow[2]. For a Poiseuille flow in a tube the critical Reynolds number $Re_{\text{crit}} > 2000$. In microfluidics the flow is almost always laminar due to the micro length scales $L \approx 100$ μm, small velocities $u \approx 1$ mm/s and kinematic viscosity 1.00×10^{-6} m^2/s yielding a Reynolds number of $Re = 0.1$.

If the flow is free of vorticity, the governing equations simplify considerably. This type of flow is called potential flow. Viscous flow is generally not potential flow, but in some special cases it may be described as such. Given the appropriate boundary conditions electroosmotic flow can be described as potential flow independent of the Reynolds number, [16].

A measure of the surface tension force to the gravitational force is given by the Bond number

$$Bo = \frac{\rho g L^2}{\sigma} \tag{2.21}$$

The characteristic length L may, for example, be the height of meniscus, the curved upper surface of a column of liquid. When the Bond number is large the surface pressure effects may be neglected in the liquid at rest.

A length scale for surface tension governed phenomenon is derived from the Bond number Eq. (2.21). Having

$$L \ll \left(\frac{\sigma}{\rho g}\right)^{\frac{1}{2}} \equiv \Delta_c \Rightarrow Bo \ll 1 \tag{2.22}$$

where Δ_c is the so-called capillary length. For $L = \Delta_c$ the Bond number is 1. Δ_c provides a measure (length scale) for when phenomena are either controlled by gravity ($> \Delta_c$) or surface tension $< \Delta_c$.

We will return to characteristic dimensionless numbers for the problem of two dielectric fluids places in **E**-field in Chap. 8.

[2]For example, the wave boundary layer in an ocean wave may not be fully turbulent before $Re = 10^6$

Chapter 3

Electroosmotic driven microflows

In this chapter[1] we will present the phenomena behind the electroosmotic (EO) microflows [18, 19, 20, 21]. It was already mentioned that surface reaction between electrolytes and glass walls lead to the charge separation close to the walls. In an axial **E**-field these charges will move and by viscous drag set the bulk liquid in motion as well.

In microsystems, surface-to-volume ratios are large. Since EOF is governed by surface reactions, it will be more efficient than ordinary pressure driven flows, a feature exploited in EO pumps [17]. Micropumps play a key role in the quest for fabricating versatile, cheap, and highly efficient microfluidic lab-on-a-chip devices. In particular, EO pumps are attractive since they contain no moving parts and are relatively easy to integrate in microfluidic circuits during fabrication [22, 23, 24, 25, 26, 27]. Design of these pumps requires the understanding of the underlying physical theory outlined below. We have used our theoretical insight to analyze the low-voltage EO pump invented by Takamura et al. [23]. Our results are presented in a research paper [3] enclosed in Appendix B.

3.1 The Electric Double Layer

As a starting point, we consider the charge transport in a liquid. The flux **J** of a charged species is driven by the gradient of a general potential, which is a function of pressure, temperature, electric state, concentrations, composition of phases, etc. An analytical description, however, is not feasible due to the nonlinear characteristics of this potential. However, if the electrolyte is dilute this is not a problem, because then the transport effects may be linearly superposed.

The involved transport processes are electromigration due to electrical fields, diffusion due to density gradients, and convection due to velocity fields. If we neglect the effects of external and induced magnetic fields, we obtain for dilute concentrations the following form of the Nernst-Planck equation [18]

$$\mathbf{J}_i = -\alpha_i z_i c_i \boldsymbol{\nabla}\phi - D_{\mathrm{mass,i}} \boldsymbol{\nabla} c_i + c_i \mathbf{u}, \tag{3.1}$$

[1]The chapter is adapted from the M.Sc. thesis by A. Brask [17], supervised by Goranović and Bruus.

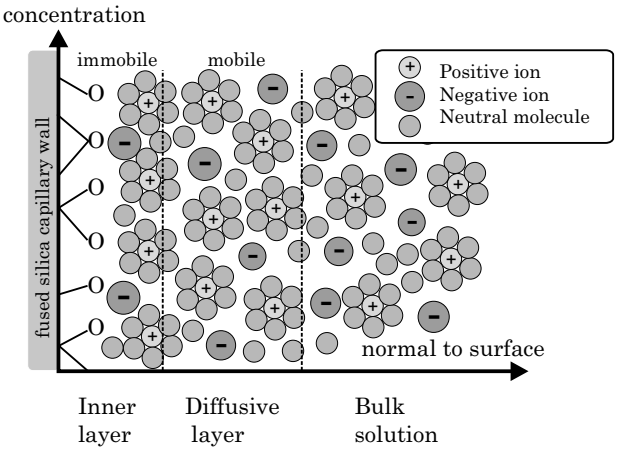

Figure 3.1: The structure of an electric double layer with an inner immobile layer. The system consisting of wall and liquid is electrical neutral. The diffuse layer is mobile and can therefore be manipulated by an external electric field. The positive ions are hydrated. Some of the negative ions are specifically adsorbed at the surface [60]

where $\mathbf{J}_i$ is the molar flux of the i-th species due to electromigration, mass diffusion, and convection, respectively. The i-th mobility α_i is related to the mass diffusivity $D_{\text{mass,i}}$ and the thermal energy kT as $\alpha_i = eD_{\text{mass,i}}/(kT)$. In the following analysis the electrolytes are assumed to be dilute.

If we consider a charged surface in contact with a dilute, fully dissociated salt, the charged surface will attract the ions of the opposite charge, the so-called counterions. Hence, a region will exist where the concentration of counterions is larger than that of the coions [2]. This phenomena leads to the formation of an electric double layer, or Debye layer. In Fig. 3.1 the wall charge is assumed negative. The term "double" refers to the fact that there are two layers: the inner layer, which is immobile due to strong electrical forces, and the outer layer (the diffusive layer) which may be affected by an external electric field. The surface charge arises from chemical reactions as discussed in Sec. 3.5.

3.2 Thickness λ_D of the Double layer

The thickness λ_D of the electrical double layer is governed by a balance between diffusion and electrical forces. The λ_D is also known in the literature as the Debye length. It is a characteristic length scale for the electrical screening. First we introduce the electrochemical potential $\overline{\mu}_{\text{chem},i}$, which is the free energy of the last arrived particle. It consists of an electric and chemical potential. The gradient of the electrochemical potential must be zero in equilibrium. If this were not the case, a flow would be induced. The chemical potential is given as

$$\mu_{\text{chem},i} = \mu^0_{\text{chem},i} + kT \ln n_i, \tag{3.2}$$

where $n_i = c_i/c_i^0$ is the concentration of ions relative to a reference concentration. $\mu^0_{\text{chem},i}$ is the standard chemical potential which is equal to the chemical potential when $n_i = 1$.

[2] The charges of the coions have the same sign as the charges of the surface.

The Debye length is found by balancing repulsive diffusive forces with attractive electrical forces, which is the same as requiring $\boldsymbol{\nabla}\overline{\mu}_i = 0$.

$$\boldsymbol{\nabla}\overline{\mu}_i = \boldsymbol{\nabla}\mu_{\text{chem,i}} + z_i e\boldsymbol{\nabla}\phi, \tag{3.3}$$

$$\boldsymbol{\nabla}\mu_{\text{chem,i}} = -z_i e\boldsymbol{\nabla}\phi, \tag{3.4}$$

In one dimension we get

$$\frac{d\mu_{\text{chem}}, i}{dx} = -z_i e\frac{d\phi}{dx}. \tag{3.5}$$

Inserting Eq. (3.2) into Eq. (3.5) yields

$$\frac{1}{n_i}\frac{dn_i}{dx} = -\frac{z_i e}{kT}\frac{d\phi}{dx}. \tag{3.6}$$

Integrating this and requiring that $\phi = 0$ when $n_i = 1$ we obtain

$$n_i = \exp(-\frac{z_i e}{kT}\phi), \tag{3.7}$$

$$c_i = c_i^0 \exp(-\frac{z_i e}{kT}\phi). \tag{3.8}$$

The Debye layer is not electrically neutral because the neutralizing charges are at the wall. Hence, the Poisson equation,

$$\boldsymbol{\nabla}\cdot(\epsilon\boldsymbol{\nabla}\phi) = -\rho_E, \tag{3.9a}$$

is invoked. For simplicity the dielectric constant ϵ is assumed spatially invariant, and hence

$$\boldsymbol{\nabla}^2\phi = -\frac{\rho_E}{\epsilon} \tag{3.9b}$$

This approximation needs further discussion because of the strong polarization effects in the Debye layer, see Sec. 3.4. The charge density is now inserted in the Poisson equation Eq. (3.9b) along with the Boltzmann distribution, Eq. (3.8), which leads to

$$\frac{d^2\phi}{dx^2} = -\frac{1}{\epsilon}\sum c_i z_i e = -\frac{1}{\epsilon}\sum c_i^0 z_i e\ \exp(-\frac{z_i e}{kT}\phi). \tag{3.10}$$

This is a nonlinear differential equation, due to the exponential terms on the right-hand side. The general solutions will be discussed in Sec. 3.3. For now we will use the Debye-Hückel approximation $\frac{z_i\phi}{kT} \ll 1$, in which case $\exp(\frac{z_i\phi}{kT}) \approx 1 - \frac{z_i\phi}{kT}$ leading to

$$\frac{d^2\phi}{dx^2} = -\frac{1}{\epsilon}\sum c_i^0(1 - \frac{z_i e\phi}{kT}) \tag{3.11a}$$

$$= -\frac{1}{\epsilon}\big(\sum e c_i^0 z_i - \sum c_i^0 z_i^2 e^2\frac{\phi}{kT}\big) z_i e \tag{3.11b}$$

$$= \frac{e^2}{\epsilon kT}\big(\sum z_i^2 c_i^0\big)\phi \tag{3.11c}$$

$$= \kappa^2\phi. \tag{3.11d}$$

In Eq. (3.11b), the first sum is zero because the bulk liquid is electrically neutral. In the last equation, the factor κ^2 in front of ϕ is by definition related to the Debye length since $1/\kappa \equiv \lambda_D$:

$$\lambda_D = \frac{1}{\kappa} = \sqrt{\frac{\epsilon kT}{e^2 \sum z_i^2 c_i^0}} \tag{3.12a}$$

$$= \sqrt{\frac{\epsilon kT}{2e^2 z^2 c}} \tag{3.12b}$$

In Eq. (3.12b), the salt is assumed symmetric for simplicity, i.e. $-z_- = z_+ = z$ and $c_+^0 = c_-^0$.

The thickness of the double layer depends on the temperature T, concentration c and valence number z of the ions, but normally it is of the order 10 nm. At a distance of approximately $3\lambda_D$, the potential will be reduced to 2% of its near surface value.

At high temperatures the ions move quickly which leads to a decrease in the shielding since they are dispersed more. For high concentrations the shielding is more effective because the charge density is larger.

Moreover, since $\lambda_D \propto (z^2 c)^{-1/2}$ the double layer is compressed if the buffer concentration or the ionic strength[3] is increased. This affects the potential distribution, and the zeta potential is reduced.

The zeta potential is expected to become larger (in magnitude) for small electrolyte concentrations.

Example: *The thickness of the double Layer*
At a temperature of 25°C in water with $\epsilon = 78.3\epsilon_0$, the above expression computes to $\lambda_D = \left(9.61 \times 10^{-9}(z^2 c)^{-1/2}\right)$ nm, with c in units of mol/m^3. For a monovalent concentration of 10^2 mol/m^3 (0.1M), $\lambda_D = 0.961$ nm. So in this case, the EDL is no more than approximately 10 atomic diameters wide.

3.3 The Electric Potential

Consider a circular capillary filled with an aqueous solution. At the solid-liquid interface an EDL is formed. The ion concentrations c_i are connected with the electric potential ϕ through the Poisson equation, Eq. (3.9b). Adopting cylindrical coordinates with x as the axial coordinate, the $\frac{\partial^2}{\partial x^2}$-terms may be neglected because variation is very small compared to the radial variation. Furthermore, the solution is assumed symmetric, so the angular variation is also disregarded, so we get

$$\frac{1}{r}\frac{\partial}{\partial r}\left(r\frac{\partial \phi}{\partial r}\right) = -\frac{\rho_E}{\epsilon} \tag{3.13a}$$

$$= -\frac{Fz}{\epsilon}(c_+ - c_-). \tag{3.13b}$$

[3]Ionic strength is a quantity representing interactions of ions with water molecules and other ions in a solution $I = \frac{1}{2}\sum z_i^2 n_i$.

It is convenient to split up the potential in two parts: a radial component $\psi(x,r)$ and an axial component $\Phi(x)$,

$$\phi(x,r) = \Phi(x) + \psi(x,r). \tag{3.14}$$

In order to find the concentrations, the ion flux is considered. In equilibrium the radial flux of ions must be zero. This requirement is inserted into the Nernst-Planck equation, Eq. (3.1),

$$0 \quad = \quad \frac{\mp z}{RT} D_{\text{mass}} F c_{\pm} \frac{\partial \psi}{\partial r} - D_{\text{mass}} \frac{\partial c_{\pm}}{\partial r}. \tag{3.15}$$

By integration of this equation and using that the diffusivity is $D_{\text{mass}} = RT\alpha$, the Boltzmann distribution is obtained for $c_+(z)$ and $c_-(z)$,

$$c_{\pm} \quad = \quad c_0 \exp\left(\mp \frac{zF\psi}{RT} \right). \tag{3.16}$$

By inserting this result into Eq. (3.13b) and making the variable dimensionless according to

$$r^* = \frac{r}{a}, \qquad \lambda^* = \frac{\lambda_D}{a}, \qquad \text{and} \qquad \psi^* = \frac{zF\psi}{RT}, \tag{3.17}$$

the following nonlinear second order ordinary differential equation (ODE) arises:

$$\lambda^{*\,2} \frac{1}{r^*} \frac{\partial}{\partial r^*} \left(r^* \frac{\partial \psi^*}{\partial r^*} \right) = \sinh(\psi^*). \tag{3.18}$$

In combination with the boundary conditions this forms a nonlinear boundary value problem (BVP).

$$\frac{\partial \psi^*}{\partial r^*} = 0, \quad \text{at} \quad r^* = 0, \tag{3.19}$$

$$\psi^* = \zeta^*, \quad \text{at} \quad r^* = 1. \tag{3.20}$$

The zeta potential will be explained in Sec. 3.5 for now it is simply the potential at the wall interface. In Fig. 3.2 the potentials have been calculated numerically for different values of λ^* using a shooting algoritm in MatLab. Two geometries are considered. A circular capillary in Fig. 3.2(a), and a one dimensional parallel plate geometry in Fig. 3.2(b). In the case of large λ, the potential equals the zeta potential across the entire channel width. For small values of λ the potential is zero everywhere except near the boundaries. This illustrates the different shielding effects. For small ratios the bulk flow is completely shielded, refer to Sec. 3.2. This will often be the case, since the Debye length being less than 10 nm is very small compared to most capillaries.

An analytical solution for the potential may be obtained by linearizing the right-hand side of Eq. (3.18), and the double layer thickness $\lambda_D \ll a$ must be small compared to the radius of the capillary. Hence curvature effects can be neglected. This is termed the Debye-Hückel approximation. The result is a simple exponential function $\psi(r)$,

$$\psi(r) = \zeta \exp\left(- \frac{a-r}{\lambda_D} \right), \tag{3.21}$$

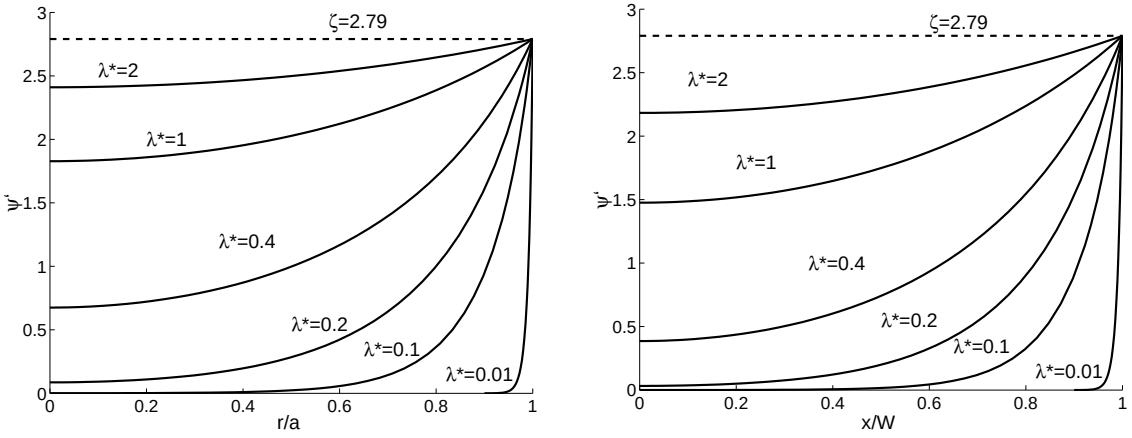

Figure 3.2: Nondimensional screening potential ψ^* in two different geometries: (a) In a radial channel where the length scale is the radius of the channel. (b) Potentials between two planes where the length scale is half the spacing of the planes.

a result that also emerges from the linearized parallel planes case, since the curvature effects here are manifestly zero.

3.4 The Helmholtz-Smoluchowski velocity

The purpose of this section is to find the velocity as a function of an external electric field. The concepts introduced here are essential for a description of electroosmotic flow. Electroosmosis is the movement of liquid relative to a stationary charged surface (e.g., a capillary or porous plug) by an electric field. The pressure necessary to counterbalance electroosmotic flow is termed the electroosmotic pressure. The equation governing the flow is the Navier-Stokes equation (see Sec. 2.3).

Since the length scale of the Debye layer is very small $\lambda_D \approx 1-10$ nm the corresponding Reynolds number is very small for normal velocities and viscosities. Hence the inertial forces may be neglected here. For a further discussion of inertial forces and Reynolds numbers see Sec. 2.6. So the problem is reduced to a balance between electric forces and viscous forces. The maximum velocity in the boundary layer is then used as a boundary condition for the bulk flow. Introducing Poisons equation to eliminate the charge density ρ_E we obtain a relation between the velocity $\mathbf{u} = (u, v, 0)$ and the applied axial potential $\phi_a(x)$:

$$\mu \boldsymbol{\nabla}^2 \mathbf{u} = \rho_E \boldsymbol{\nabla} \phi_a \tag{3.22}$$

$$= -\epsilon \big(\boldsymbol{\nabla}^2 \phi \big) \boldsymbol{\nabla} \phi_a \tag{3.23}$$

To identify nonessential terms the x and y coordinates are scaled to ξ and η by the radius

a and the Debye length λ_D, respectively,

$$\xi = x/a, \tag{3.24}$$

$$\eta = y/\lambda_D. \tag{3.25}$$

The Laplace operator of the intrinsic potential ϕ_i and the gradient of the applied potential ϕ_a in Eq. (3.23) are computed separately in Eqs. (3.26b) and (3.26c) below. Note that the tangential term in the gradient of the intrinsic potential is expressed by means of the applied potential. Its magnitude is proportional to the applied field by the factor χ. This is a correction factor due to the polarization of the dielectric liquid within the Debye layer. The electric field in the Debye layer $E \approx 10^7$ V/m is much larger than the applied field $E \approx 10^4$ V/m. The terms computes to

$$\boldsymbol{\nabla}\phi_i = \left(\frac{\chi}{a}\frac{\partial\phi_a}{\partial\xi}, \quad \frac{1}{\lambda}\frac{\partial\phi_i}{\partial\eta}, \quad 0\right), \tag{3.26a}$$

$$\boldsymbol{\nabla}^2\phi_i = \frac{\chi}{a^2}\frac{\partial^2\phi_a}{\partial\xi^2} + \frac{1}{\lambda^2}\frac{\partial^2\phi_i}{\partial\eta^2}, \tag{3.26b}$$

$$\boldsymbol{\nabla}^2\mathbf{u} = \left(\frac{1}{a^2}\frac{\partial^2 u}{\partial\xi^2} + \frac{1}{\lambda^2}\frac{\partial^2 u}{\partial\eta^2}, \quad \frac{1}{a^2}\frac{\partial^2 v}{\partial\xi^2} + \frac{1}{\lambda^2}\frac{\partial^2 v}{\partial\eta^2}, \quad 0\right). \tag{3.26c}$$

A value of the χ-factor is difficult to obtain. A more detailed physical description of the Debye layer is required. This is beyond the scope of the this analysis, but the χ-factor can be incorporated in an suitable choice of the dielectric constant for the Debye layer, in the following just denoted ϵ.

Collecting terms in the axial direction x, and neglecting terms of order λ/a or higher Eq. (3.23) becomes

$$\mu\frac{\partial^2 u}{\partial\eta^2} = \epsilon E_x \frac{\partial^2\phi_i}{\partial\eta^2}, \tag{3.27}$$

where $E_x = -d\phi_a/dx$ is the applied electric field. Note that the gradient of the applied field is given in the x-y coordinates. By double integration with respect to η and use of the conditions $\frac{\partial u}{\partial\eta} = \frac{\partial\phi_i}{\partial\eta} = 0$ as $y \to \infty$ and that $\phi_i = \zeta$ at $u = 0$, the integrated equation yields the very important Helmholtz-Smoluchowski relation (see also Fig. 3.3),

$$u_{\text{eo}} \equiv u(\infty) = \frac{\epsilon\zeta}{\mu}\frac{d\phi_a}{dx} = \alpha_{\text{eo}}E_x, \tag{3.28}$$

$$\alpha_{\text{eo}} = -\frac{\epsilon\zeta}{\mu}, \tag{3.29}$$

where u_{eo} is the so-called electroosmotic velocity, and where α_{eo} is the EO mobility. Recent research has shown that the zeta potential is ambiguous in that sense that for one mobility there may be two corresponding zeta potentials [31]. It is therefore important to emphasize that it is the EO mobility α_{eo} that is important with respect to EO pumps.

The electric field is given by the potential and the electrode separation. If a dielectric is present the field is unchanged, but the charges at the electrodes are increased in magnitude.

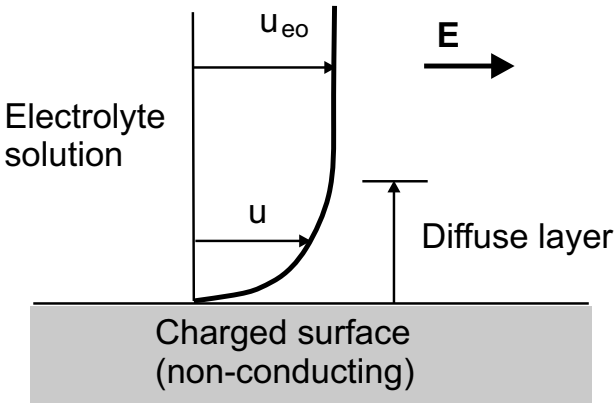

Figure 3.3: Flow produced by an electric **E** field acting on a charged diffuse double layer. The electroosmotic velocity $u_{\rm eo}$ is given by $u_{\rm eo} = \alpha_{\rm eo}\ E$. There is overall charge neutrality.

One should be careful not to confuse this setup with an isolated capacitor, with fixed charges, in which the field is reduced because of the dielectric.

Example: *EO velocity*
In an experiment conducted by Cummings *et al.* [16], the applied electric field is 50 V over 20 mm, thus $E_x = 2.5 \times 10^3$ V/m. The zeta potential, $\zeta = -100$ mV, the dielectric constant is $\epsilon = 78.3\ \epsilon_0$, and the dynamic viscosity $\mu = 1.0 \times 10^{-3}$ kg (m s)$^{-1}$ are those of water at room temperature. This yields $u_{\rm eo} = 200\ \mu$m/s

3.5 The Zeta Potential

The thickness of the double layer is given by the Debye length λ_D. The derivation of the Debye length was based on the assumption that the ions are points. In real life the ions are not that small compared with the Debye length. So when considering the boundary condition for the potential, we must have a more accurate description. The center of the inner most ions are in a finite distance from the surface. This inner layer is called the Stern layer, Fig. 3.4. This layer is bounded by strong electrostatic forces $E \approx 10^7 - 10^8$ V/m and hence is immobile. The counterions are attracted to the surface and in this way screening the surface charge. The zeta potential is defined as the potential difference across the Debye layer from the shear surface between the charged surface and the electrolyte to the far field (zero) [18]. The zeta potential is typically of the order $\zeta \approx 1 - 200$ mV. The system, liquid and surface, is electrically neutral. So the wall charge must equal that of the fluid charge with opposite sign. Far away from the wall, the fluid is electrically neutral [32].

We are considering glass as the main material that the capillaries are made of. Other materials such as polymers (e.g., PMMA) can also be used. Such materials are interesting with respect to mass production and fast prototyping, but glass/siliconoxide offers the highest level of refinement available, i.e., the most accurate and reproducible structures.

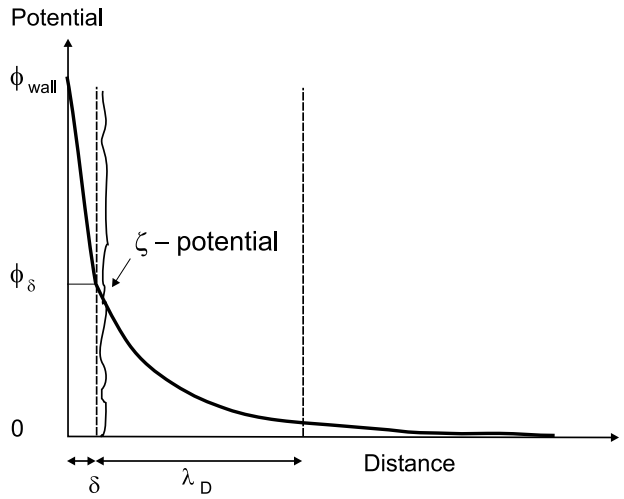

Figure 3.4: Structure of electric potential in the double layer with inner Stern layer. The thickness of the Stern layer is approximately the width of an atom $\delta \approx 0.1$ nm. The zeta potential is defined at the surface of shear, i.e. where the ions start to move [18].

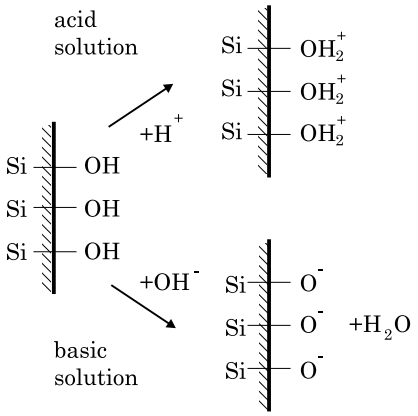

Figure 3.5: Chemical reactions for silicon in aqueous mediums with different pH. Silanol groups react with the ions in the aqueous solution, creating an excess of charge at the surface.

If siliconoxide (silica or quartz) is immersed in water, the potential is generated by a chemical reaction at the surface. The silanol groups SiOH are changed to either $SiOH_2^+$ or SiO^- depending on the buffers pH value, Fig. 3.5.

In this way the zeta potential may be varied by the pH of the buffer solution. At the some pH-level, point of zero charge, the wall potential is zero. For high pH levels the change in EO mobility is marginal. A suitable choice of the buffers pH-value must be considered in order to have effective electroosmotic pumping.

$$\mathrm{SiOH} + \mathrm{H}^+ \rightarrow \mathrm{SiOH}_2^+ \tag{3.30}$$

$$\mathrm{SiOH} + \mathrm{OH}^- \rightarrow \mathrm{SiO}^- + \mathrm{H_2O} \tag{3.31}$$

$$\mathrm{pK_a}(-\mathrm{SiOH}) \approx 6 \tag{3.32}$$

3.6 Flow in a Circular Capillary

In this section we shall find the velocity distribution $u(x, y)$ without the infinitely thin Debye layer assumption. An analytical solution is possible due to the simple geometry. The electric potential and the corresponding charge distribution were found in Sec. 3.3.

The Navier-Stokes equation is applied to derive the velocity distribution in a circular capillary. The inertia terms vanish identically due to the high symmetry of the problem: only $u_x \neq 0$, but $u_x = u_x(y)$ so $u_x \partial_x u_x \equiv 0$. Pressure on the other hand needs to be included, because the entire capillary flow may not be driven solely by electroosmosis. For stationary flow we therefore end up with

$$0 = -\boldsymbol{\nabla} p + \mu \boldsymbol{\nabla}^2 \mathbf{u} - F(z_+ c_+ + z_- c_-) \boldsymbol{\nabla} \phi_a, \tag{3.33}$$

where the electric field has been replaced by minus the gradient of the applied potential ϕ_a. Using cylindrical coordinates for the axisymmetric capillary, we adopt (r, θ, x) with x being the axial direction, i.e. the direction of the flow. The azimuthal and radial directions are described by the coodinates θ and r, respectively. We are solving for the velocity component u in x-direction, $\mathbf{u} = (0, 0, u)$.

Eq. (3.33) is a sexond order partial differential equation. Due to the rotational and translation invariance of both the differential equation and the boundary conditions, the solution u depends only on r, thus $u = u(r)$ and Eq. (3.33) becomes

$$\frac{\mu}{r} \frac{d}{dr} \left(r \frac{du}{dr} \right) = \frac{dp}{dx} + Fz(c_+ - c_-) \frac{d\phi_a}{dx}. \tag{3.34}$$

Using Eq. (3.13b) to eliminate the charge densities, one obtains the modified Navier-Stokes equation, which is then integrated with the appropriate boundary conditions.

$$\frac{\mu}{r} \frac{d}{dr} \left(r \frac{du}{dr} \right) = \frac{dp}{dx} - \frac{\epsilon}{r} \frac{d}{dr} \left(r \frac{d\psi}{dr} \right) \frac{d\phi_a}{dx}, \tag{3.35a}$$

$$\left. \frac{du}{dr} \right|_{r=0} = 0, \quad \text{and} \quad \left. \frac{d\psi}{dr} \right|_{r=0} = 0, \tag{3.35b}$$

$$u(a) = 0, \quad \text{and} \quad \psi(a) = \zeta. \tag{3.35c}$$

The solution is

$$u(r) = \Big[\psi(r) - \zeta \Big] - \frac{\epsilon}{\mu} \frac{d\phi_a}{dx} + \frac{r^2 - a^2}{4\mu} \frac{dp}{dx}. \tag{3.36}$$

Here the Debye-Hückel approximation Eq. (3.21) may be utilized for $\psi(r)$, or more correctly the potentials given in Fig. 3.4. If the Debye-Hückel approximation is used, the solution becomes

$$u(r) = \frac{\epsilon \zeta}{\mu} \Big[1 - \exp\Big(- \frac{a - r}{\lambda_D} \Big) \Big] \frac{d\phi_a}{dx} + \frac{r^2 - a^2}{4\mu} \frac{dp}{dx}. \tag{3.37}$$

From this the flow rate Q is easily obtained by integration

$$Q = \frac{\epsilon\zeta}{\mu}\frac{d\phi_a}{dx}\pi a^2\Big(1-2\frac{\lambda_D}{a}\Big) - \frac{\pi a^4}{8\mu}\frac{dp}{dx}. \tag{3.38}$$

Two important conclusions can be derived from Eq. (3.38):

(1) The flow rate, Q is reduced in the case of channel dimensions comparable with the Debye layer thickness. However Eq. (3.38) is not valid for $a \approx \lambda_D$.

(2) The flow rate induced by EO is proportional to $Q \propto a^2$, whereas the pressure driven flow is proportional to $Q \propto a^4$. Scaling of a capillary will therefore make EOF more effective in small capillaries. In the extreme case of uniform charge distribution (total Debye layer overlap), a parabolic flow profile will be induced, identical to that of pressure driven flow and $Q \propto a^4$.

Chapter 4

Simulations of interfaces in two-fluid systems

In this chapter we give an account on several microfluidic systems which make use of two-fluid interfaces in their operating principles. The applications are interesting since each comprises a number of phenomena characteristic for microfluidics - an advantage with respect to one aspect can sometimes mean a disadvantage with respect to another. All of these systems have been simulated on a CFD software. One device has been microfabricated and measurements performed in order to test the simulations. This chapter is an overview of principles described in my four publications [1, 4, 10, 11] in Appendices A, C, D, and E, respectively.

4.1 Miscible streams in micro cell sorters

The first example that we are going to consider is a type of device called micro-fabricated cell sorter (μFACS), Fig. 4.1 (a), which is used to focus a stream of cells inside a microfluidic system, [2, 33]. When three separate adjacent streams enter a long microchannel, the width of the middle stream can be regulated (focused) by adjusting the flow rates of two outer streams. The idea is to use the focusing effect so that cells, carried by the middle stream, can be better manipulated, e.g. counted and sorted in an easier manner.

In a traditional cell sorting system, the focusing is done only sidewise, while using a so-called chimney structure it is done from all sides i.e. coaxially, the middle stream being now completely surrounded by the outer liquid, Fig. 4.1 (b). The flows thus represent submerged jets of one viscous liquid within another, producing a viscous drag schematically shown in Fig. 4.2 (a). This issue will be discussed further below when viscous pumping is considered.

Since the two streams are miscible liquids, the boundary between them will be a diffused one. The focusing effect will be more pronounced as the difference of the flow rates between the outer and the middle streams is increased [5]. This is because the convective term, depending on the higher velocity of the outer stream, will dominate the lateral diffusion. This can be seen in Fig. 4.2 (b) where the cross-sections of the focused

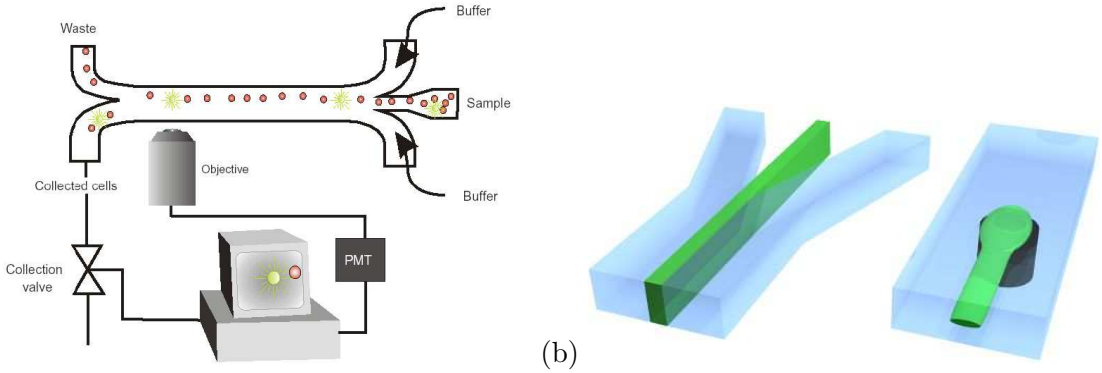

Figure 4.1: (a) A schematic view of a micro cell sorter, [2]. (b) Schematic differences in focusing of the middle stream. The sheathing from the sides (left) as compared with the coaxial sheathing using chimney (right). In a chimney set-up, only one sheathing stream is needed. Courtesy of I.R. Perch-Nielsen.

middle stream are shown for two sheath-to-samplestream flow rate ratios.

The middle stream coming out of chimney is peculiar in that it is not clear whether it will remain positioned vertically in the middle for all times. Issues such as stability and the Coanda effect deflecting the jet to nearby geometry, play important role. In Ref. [1], the chimney is embedded in a basin lowered from the main channel, see Appendix A. A pressure drop will occur inside the basin below the middle stream, causing the stream to be deflected downwards. Concentration contours extracted from simulations predict that the stream will tend to stick to the bottom wall Fig. 4.2 (b).

The measurements in microfluidic systems are hard to obtain due to their small size. In a set of experiments using microPIV (Particle-Image-Velocimetry) measurements, the velocity profiles obtained by simulations were compared with experiments. The results differ mainly due to numerical diffusion.

From a practical point of view, a chimney embedded in cavity-like basin will tend to collect bubbles which are unwanted. The reasons for this we address next.

4.2 Bubbles in microchannels

Another example of two-fluid interfaces in microfluidic systems are gas bubbles. Such bubbles present a significant problem: they can block the microchannels, disrupt the flow, and disturb measurements in an uncontrolled manner.

4.2.1 Formation of bubbles

The following are the most common reasons for bubble formation:

- Cavitation (or, nucleation). When the local pressure $p(x)$ drops below the vapor pressure p_v of a fluid, a bubble containing mainly the vapor molecules spontaneously develop. The liquid is said to "break" at the point of cavitation. The effect can be

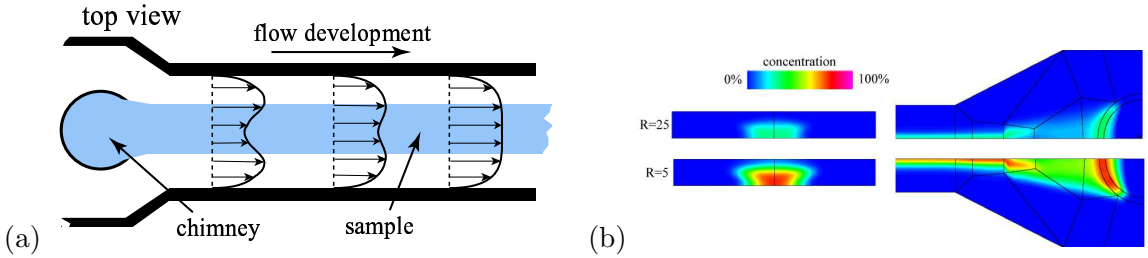

Figure 4.2: (a) Schematic view of the viscous drag by two outer streams. (b) Simulations of concentration contours for different focusing ratios R (R=sheath-flow rate/sample-flow rate). On the left, the cross-sections of the outer channel are shown with the middle stream being more (top) and less (bottom) focused. On the right, the corresponding top view of a part of the chimney structure, see Appendix A. The middle stream contains a sample species that can diffuse into the sheathing liquid. The focusing is better for higher R, and confined to the bottom of the channel.

enhanced either by raising the temperature and thus increasing the vapor pressure[1], or by decreasing the local pressure. The latter effect is particularly pronounced at junctions of microfluidic systems when changes in pressure occur due to sudden contractions/expansions.

- Solubility. The solubility of a gas in a liquid is governed by Henry's law, which states that the partial pressure of a gas above a solution is directly proportional to the concentration of that gas in the solution, [32]. The solubility decreases with increasing temperature. A common practice with respect to lab-on-chip systems is to push helium (which itself does not nucleate under ordinary conditions) through the system to lower the partial pressure of other gases and therefore their concentration inside the liquids. Such a degassing procedure is usually good for several hours.

- Electrolysis. In microfluidic systems containing electrodes and operating under DC voltages, e.g. some types of EO micropumps, gases will form next to the electrodes due to electrolysis. The buffers are usually water solutions, and so hydrogen and oxygen will develop. The problem will be circumvented if AC fields are applied (and design allows it).

- Heating. As mentioned, heating of devices will cause bubbles to form: liquid might evaporate or dissolved gases expand.

Apart from the degassing method, the removal of unwanted bubbles might involve high-frequency sound vibrations or control of surface tension. However, in spite of such efforts gas bubbles may still be present, and once there it often requires large driving pressures to push them out of the system, [35].

[1] At 20 °C the vapor pressure for water is 0.023 bar, but at 100 °C it is 1 bar and the water boils, [34].

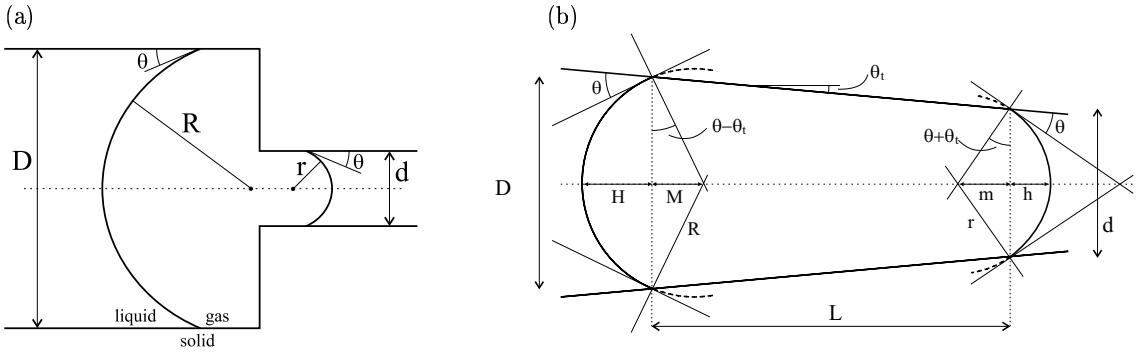

Figure 4.3: (a) A bubble passing through a sudden contraction. The curvatures at both ends are different and constant while the bubble is in the contraction. (b) A bubble in a tapered channel. Appropriate names have been given to different lengths and angles in use. The curvatures depend on the position of the bubble because of the tapering. See Appendix D.

4.2.2 Clogging of microchannels

If a slowly moving bubble is present in a circular capillary of diameter d, the gas-liquid interface has a spherical shape, [36], as sketched in Fig. 4.3. This is true as the spherical shapes provide a minimal pressure drop and thus a minimum surface energy. The pressure drop over each of the interfaces is given by Young-Laplace equation

$$\Delta P_i = \sigma \left(\frac{1}{R_1} + \frac{1}{R_1} \right) = 4\sigma \frac{\cos\theta}{d}, \tag{4.1}$$

where θ is the contact angle, and the two main curvatures are identical due to symmetry, $R_1 = R_2 = R$. In a straight channel the total pressure drop, due to curvature, over the bubble is obviously zero. ΔP_i is identical with different sign at each end of the bubble. To move the bubble through a straight channel only the friction needs to be overcome. The required pressure is

$$\Delta P_f = \frac{4\sigma_f}{d}, \tag{4.2}$$

where σ_f is a frictional surface tension parameter. However, if there is a sudden change in the capillary radius the pressures ΔP_i on two sides of the bubble will not balance each other. The pressure drop over the bubble is

$$\Delta P_b^{\text{sudden}} = 4\sigma \left(\frac{1}{d} - \frac{1}{D} \right), \tag{4.3}$$

and acts as a blocking pressure, in addition to ΔP_f, making it harder to push the bubble into the part of a smaller radius. A bubble in a sudden contraction is shown in Fig. 4.3 (a). If on the other hand the contraction is tapered, the pressure drop is given by

$$\Delta P_b^{\text{tapered}} = 4\sigma \Big(\frac{\cos(\theta + \theta_t)}{d} - \frac{\cos(\theta - \theta_t)}{D} \Big), \tag{4.4}$$

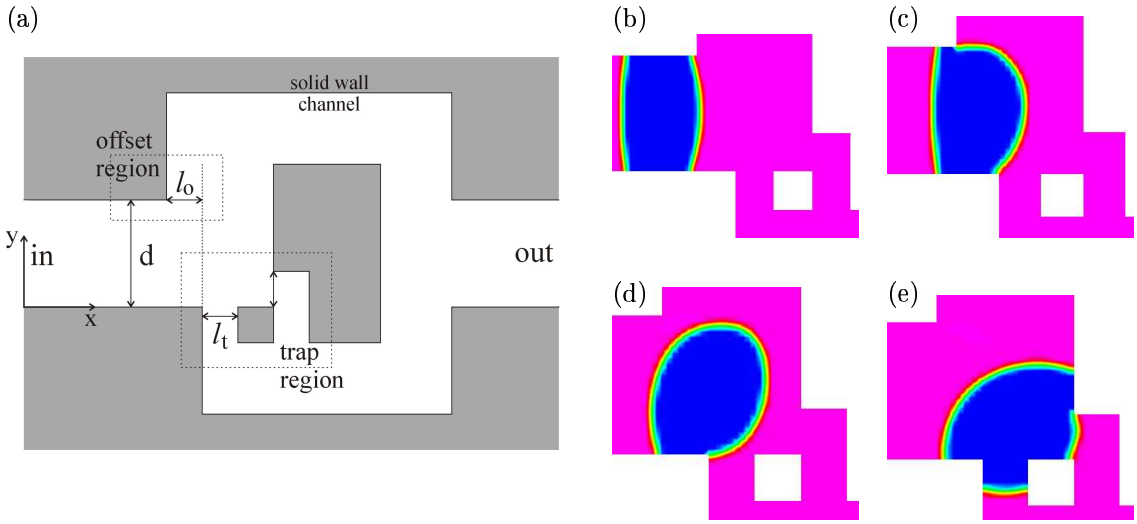

Figure 4.4: (a) A sketch of the trap geometry where the central length scales are marked: the width d of the main channel, the size l_0 of the offset between the upper and lower wall, and the width l_t of the narrow trapping channels. (b)-(e) Four snapshots of the simulated trapping procedure near the offset and trap regions. (b) A bubble moving towards the offset region. (c) Detaching of one side of the bubble by the offset effect. (d) The bubble is pushed towards the trapping region. (e) The bubble gets trapped. See also Appendix D.

where θ_t is tapering angle, Fig. 4.3 (b). The pressure contribution ΔP_b due to the curvature effects will be smaller in case of the tapered channels than in the case of sudden contraction. Therefore, it may be beneficial to use tapered constrictions in microfluidic networks where the presence of bubbles poses a problem.

However, some interesting and non-intuitive behavior appears when the full analysis is made about the dependence of $\Delta P_b^{\text{sudden}}$ on arbitrary tapering angle. A systematic study of a bubble passing through tapered constriction in a quasi-static motion has been conducted and presented in the paper enclosed as Appendix C.

4.2.3 Passive bubble trap

The curvature effects described above can be used to manipulate the bubbles by directing them away from the main flow into specific locations from which they could be removed. For this purpose a special passive bubble trap is developed, using a combination of geometry and surface tension effects. Fig. 4.4 (b)-(e) show a 2D CFD simulation of a bubble-trapping process allowing unhindered flow. In a real system, several bubble traps could be placed at locations where there is a tendency of bubble creation. Using special semi-permeable materials (e.g. Gore-Tex), the bubbles could then be extracted from the region and out of the system.

4.3 Two-liquid viscous pump

As a final example of systems with two fluid interfaces, we will present a device operating with two immiscible liquids such as water and oil; namely, a unique EO pump able to pump non-conducting liquids. Non-conducting liquids do not form the electric double layer at channel walls since they have very low conductivity ($< 10^{-6}$ S/m) i.e. very low amount of dissociated ions. Therefore, they cannot be pumped by ordinary EO pumps.

The device has been developed during the PhD project together with A. Brask, and is even patented (provisional US Patent application; see the conference paper enclosed in Appendix E.).

4.3.1 Submerged jets

Before the attempt to explain the mechanism of this two-liquid viscous pump, we will expose a known phenomenon called entrainment of one fluid by another, [37]. If a fluid jet, say water, is submerged in another fluid, say air, such as the stream from a water tap, the jet will drag with itself the air not only from the border where the fluids are in direct contact, but also the air within the boundary layer of a finite thickness. This phenomenon is exploited in so-called filter pump used in chemical laboratories, Fig. 4.5 (a). The more air is entrained with the streaming water, the more air will flow from the side channel to replace it, creating a significant suction. The emphasis here is on the viscous drag within the boundary layer. If a water jet is submerged within water the same phenomenon will appear; this is precisely what happens in μFACS using the chimney except that the outer, faster jets do the drag.

In microfluidics the boundary layer can occupy large portions of channels, so the same type of filter pump could, in principle, be possible to build in microsystems. The problem is, however, to pump the driving jet in the first place.

4.3.2 EOF induced viscous drag

An idea was proposed by O. Geschke, MIC, to possibly use an EOF as a driving mechanism to drag other liquids. The intention was to direct a conducting, so-called pumping liquid, through two side-channels, and then try to drag any, in particular non-conducting, working liquid into the main channel, Fig. 4.5 (b). The original design was not successful since it basically did not enable the pressure build-up, due to the equal flow resistances of the outer channels. Three features have been introduced in the improved design, Fig. 4.6.

- The EOF is more efficient than pressure in microflows, Eq. (3.38). By increasing the flow resistance of the side channels, the conducting pumping liquid is able to flow through them, while the working liquid is largely prevented from entering - a built pressure will not "leak" (as much) through these side pressure valves.
- The conducting liquid needs to be confined close to the walls to provide a free boundary to enable the entrainment effect i.e. to enhance the amount of working liquid through the main channel. This is achieved by lowering EO mobility in the side channels as compared to the main channel.

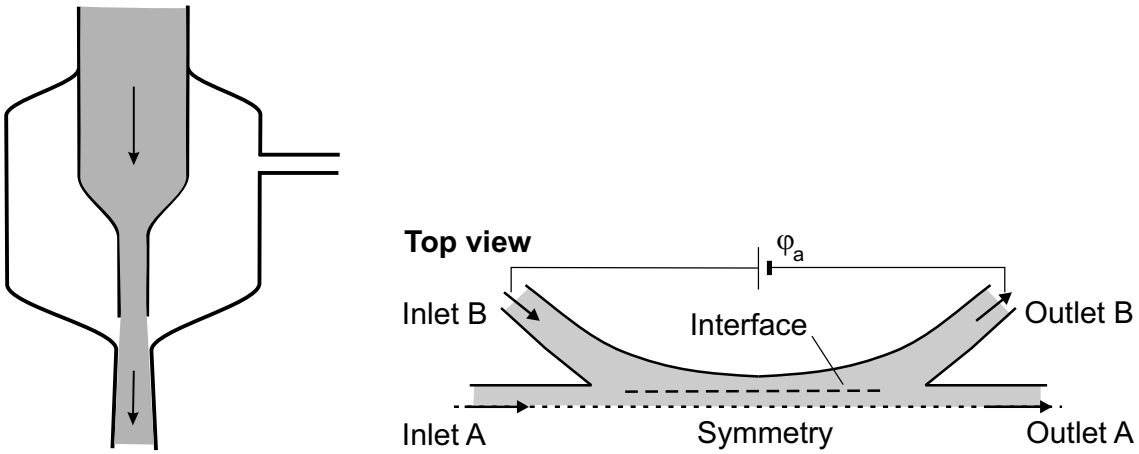

Figure 4.5: (a) The water-jet pump creates suction effect by entrainment of the air within the boundary layer at the free air-water interface, [37] (b) The original but not usable idea of a two-liquid viscous pump. The pumping liquid driven by EOF enters through inlet B and the working liquid at inlet A. Inlet/outlet B are connected to external reservoirs, [17].

- In order to achieve the largest possible **E**-field in the main channel, and thus to increase the driving velocity, Eq. (3.28), the pressure valves are made short (small electric resistances). This will enable a desirable low voltage operation.

The performance of the pump has been analyzed using two methods, [11]. The pressure and flow rates have been calculated by equivalent circuit theory, and in addition, a set of CFD simulations was carried yielding more detailed information on the distribution of pressures and velocities. The two methods were applied to the cases of both immiscible and miscible liquids. Pumping of an immiscible liquid is shown in Fig. 4.7. Three sets of resulting backpressures and corresponding flow rates are shown in Table 4.3.3. The generated pressures are not very large, but the pump Q-p characteristic largely depends on the geometrical factors and can be significantly enhanced by advanced etching techniques. The pump still works for miscible liquids, but here the working liquid gets mixed with the pumping liquid. Because of the possibility to pump all types of liquids, the described concept seems very promising.

4.3.3 Instability problem

Our analysis of the pump did not, however, include a stability analysis. The interface between two immiscible liquids will be subject to flow disturbances which are always present in the flow. It is therefore important to estimate the flow regimes under which the instabilities, that lead eventually to flow disruption, can develop in course of time.

The analysis, however, is a comprehensive task. It requires the understanding of electrohydrodynamics (EHD) i.e. the way how electric fields couple with hydrodynamics. We will dedicate the next four chapters to address to some extent the aspects of electrohydrodynamic instability. This is then applied to two-liquid microfluidic systems which bring

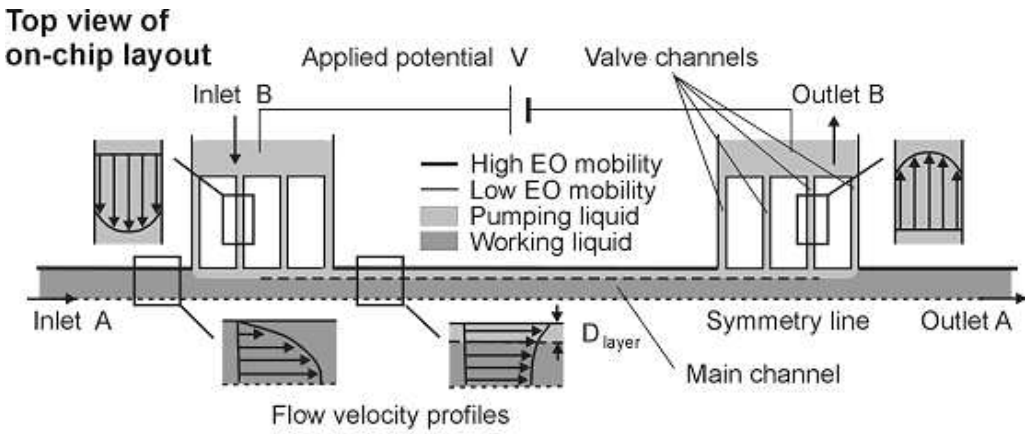

Figure 4.6: A schematic view of our two-liquid viscous pump, Appendix E. The pumping liquid and the working liquid are shown in light gray and dark gray, respectively. The expected velocity profiles are shown as inserts to give an idea of the overall flow. Internal friction gives rise to a counter pressure, which induces the parabolic flow profiles. The thickness of the pumping liquid layer is D_{layer}.

into light some interesting features.

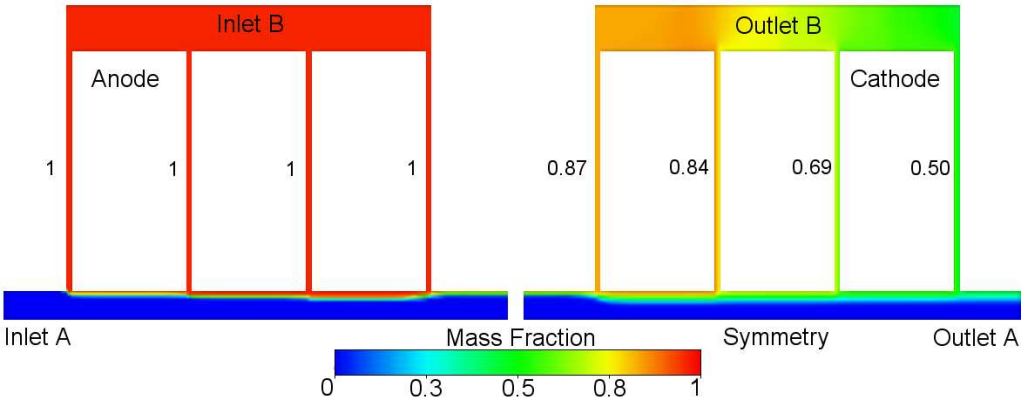

Figure 4.7: A CFD simulation of an immiscible two-phase flow. The pumping liquid of mass fraction 1 is introduced through inlet B. At outlet B the mass fraction drops to 0.87 and lower as shown, and a part of the pumping liquid continues in the main channel.

	EO mobility $\alpha_{\text{eo}}/\mu\text{m}^2(\text{V s})^{-1}$	Max flow rate Q / nL/s	Backpressure Pa
Model	0	0.296	31.6
Simulation	0	0.290	30.6
Deviation		2%	3%
Model	5000	0.267	28.5
Simulation	5000	0.260	27.4
Deviation		3%	4%
Model	10000	0.237	25.3
Simulation	10000	0.230	24.3
Deviation		3%	4%

Table 4.1: Comparisons between the circuit model and a CFD simulation. The results for three different EO mobilities in the valve channels are shown. The agreements are within 4%. Parameters: $\phi_a = 10$ V and $p_{\text{in}} = p_{\text{out}} = 0$.

Chapter 5

Fluid dielectrics and the Maxwell stress tensor

In the following chapter we investigate the effects of the electric fields on fluid dielectrics. In microfluidic systems large **E**-fields can be achieved by applying relatively small voltages, due to the smaller length-scales involved. The effect of **E**-fields, therefore, will be quite significant.

We first introduce the electrical, Maxwell, stress tensor in vacuum, a useful concept in expressing the electrical body forces, [15].

We then define thermodynamic properties of dielectrics placed in an electric field to understand how does the presence of the field affect these properties, Landau and Lifshitz [38].

The thermodynamical approach leads to important general expressions for the stress tensor and the resulting electrical force on a dielectric placed in an electric field. The various terms in the force equation are then explained.

Finally, the stress conditions on the boundary between two fluid dielectrics are discussed and the non-trivial condition on the pressure difference derived.

5.1 The Maxwell stress tensor in free space

Consider a system of stationary charges inside a volume V placed in an electrostatic field in vacuum. We assume that the volume is free of any neutral dielectric material. If ρ is the charge density, the force acting on it is

$$\mathbf{F}^e = \int_V \rho \mathbf{E}\, dV = \int_V \left[\boldsymbol{\nabla}\cdot(\epsilon_0 \mathbf{E})\right] \mathbf{E}\, dV. \tag{5.1}$$

By the following transformation, the integrand can be written as the divergence of a tensor. Since $\boldsymbol{\nabla}\times\mathbf{E} = 0$ we can subtract $\epsilon_0\mathbf{E}\times(\boldsymbol{\nabla}\times\mathbf{E})$ and obtain the i-th component of the force

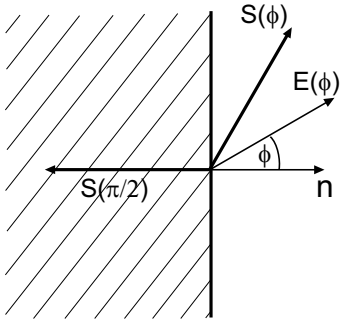

Figure 5.1: The electric stress $\mathbf{S}^e$ acting on a surface enclosing charges placed in an electric field. For an arbitrary angle θ, the **E**-field bisects the angle between the stress and the normal **n**. In a perpendicular **E**-field, the stress is normal to the surface, pointing outwards. In a tangential **E**-field, the stress is directed inwards.

per unit volume in the following form [15]

$$\frac{1}{\epsilon_0}\rho E_i = E_i(\boldsymbol{\nabla}\cdot\mathbf{E}) - [\mathbf{E}\times(\boldsymbol{\nabla}\times\mathbf{E})]_i \tag{5.2a}$$

$$= E_i\partial_k E_k - [E_j(\partial_i E_j - \partial_j E_i) - E_k(\partial_k E_i - \partial_i E_k)] \tag{5.2b}$$

$$= \partial_i\Big(E_i^2 - \frac{1}{2}E^2\Big) + \partial_j(E_i E_j) + \partial_k(E_i E_k) \tag{5.2c}$$

$$= \frac{1}{\epsilon_0}\partial_k T_{ik}^M. \tag{5.2d}$$

This is divergence of a tensor. Applying Gauss theorem, the i-th component of the total force can therefore be written as a surface integral

$$F_i^e = \int_V \rho E_i \, dV = \int_S T_{ik}^M \, df_k = \int_S T_{ik}^M n_k df, \tag{5.3}$$

where the normal vector $\mathbf{n} = (n_x, n_y, n_z)$ is directed out of the volume. The tensor T_{ik}^M is called the Maxwell stress tensor,

$$T_{ik}^M = -\frac{1}{2}\epsilon_0 E^2\delta_{ik} + \epsilon_0 E_i E_k. \tag{5.4}$$

Note that the force on an empty volume placed in a static **E**-field vanishes while the stress tensor T_{ik}^M does not. From Eq. (5.3) we see that the force on a stationary charge distribution can be determined by calculating the electric stress over a surface surrounding the charges. The force acting on a unit area of the volume in vector notation is

$$\mathbf{S}^e = -\frac{1}{2}\epsilon_0 E^2\mathbf{n} + \epsilon_0(\mathbf{n}\cdot\mathbf{E})\mathbf{E}. \tag{5.5}$$

It is useful to express the applied **E**-field in terms of the normal and tangential components with respect to the surface

$$\mathbf{E} = E\cos\theta\,\mathbf{n} + E\sin\theta\,\mathbf{t}, \tag{5.6}$$

where θ is the angle between the **E**-field and the normal, Fig. 5.1 (a). Inserting the above field into Eq. (5.5) we get

$$\begin{aligned}\mathbf{S}^e &= -\tfrac{1}{2}\epsilon_0 E^2\mathbf{n} + \epsilon_0(E\cos\theta)(E\cos\theta\,\mathbf{n} + E\sin\theta\,\mathbf{t}) \\ &= -\tfrac{1}{2}\epsilon_0 E^2(1-2\cos^2\theta)\,\mathbf{n} + \tfrac{1}{2}\epsilon_0 E^2\sin 2\theta\,\mathbf{t} \\ &= \tfrac{1}{2}\epsilon_0 E^2(\cos 2\theta\,\mathbf{n} + \sin 2\theta\,\mathbf{t}),\end{aligned} \tag{5.7}$$

so that **E** bisects the angle between the stress and the normal. The following cases are of special interest:

$$\mathbf{S}^e = \frac{1}{2}\epsilon_0 E^2\mathbf{n}, \qquad (\theta = 0,\pi), \tag{5.8a}$$

$$\mathbf{S}^e = -\frac{1}{2}\epsilon_0 E^2\mathbf{n}, \qquad (\theta = \pi/2), \tag{5.8b}$$

$$|\,\mathbf{S}\,| = \frac{1}{2}\epsilon_0 E^2, \qquad (\text{all}\quad \theta). \tag{5.8c}$$

If the **E**-field is perpendicular to the surface ($\theta = 0,\pi$), the stress is in the direction of the normal (and the field) pulling the element; if the field is parallel to the surface ($\theta = \pi/2$), the stress is directed *inwards* i.e., pushes the surface in the opposite direction of **n**. In all cases the total magnitude of the stress is constant and equal to $\epsilon_0 E^2/2$.

To understand the true meaning of the Maxwell stress tensor, one needs to consider the total force on a system of charges moving within variable EM-fields i.e. the Lorentz force

$$\mathbf{F}^e + \mathbf{F}^m = \int_V \rho(\mathbf{E} + \mathbf{v}\times\mathbf{B})\,dV = \frac{d}{dt}\mathbf{P}_{mech}. \tag{5.9}$$

$\mathbf{F}^e$ and $\mathbf{F}^m$ are electric and magnetic forces, respectively, and we have expressed the total force as the rate of change of linear *mechanical* momentum $\mathbf{P}_{mech}$. After somewhat involved transformations, similar to the one giving Eqs. (5.2a) - (5.2d), we arrive at [15]

$$\frac{d}{dt}\mathbf{P}_{mech} + \partial_t\int_V \epsilon_0\mathbf{E}\times\mathbf{B}\,dv = \int_V T_{ik}^M df_k, \tag{5.10}$$

where now T_{ik}^M includes also the magnetic contribution

$$T_{ik}^M = -\frac{1}{2}\left[\epsilon_0 E^2 + \mu_0 B^2\right]\delta_{ik} + \epsilon_0 E_i E_k + \frac{1}{\mu_0}B_i B_k. \tag{5.11}$$

From Eq. (5.10) we see that, unlike for the static fields, the time-varying fields will exert a force $\partial_t\int_V \epsilon_0\mathbf{E}\times\mathbf{B}\,dv$ over an empty volume, that is, when $\mathbf{F}^e = \mathbf{F}^m = 0$. The quantity

$$\mathbf{g} = \epsilon_0\mathbf{E}\times\mathbf{B}, \tag{5.12}$$

has dimension of momentum density and is interpreted as the momentum density of electromagnetic field. Eq. (5.10) now can be written

$$\frac{d}{dt}(\mathbf{P}_{mech} + \mathbf{P}_{field})_i = \int_V T_{ik}^M n_k df, \tag{5.13}$$

expressing the conservation of linear momentum of particles and fields. The term $T^M_{ik} n_k$ measures therefore the momentum flux per unit area into the volume.

We have seen that Maxwell stress tensor, T^M_{ik}, can be *used* to calculate the electric force on the system of particles and fields enclosed inside a volume V. However, an important aspect discussed in Ref. [39] is worth of attention. In the early days of electromagnetic theory, Maxwell and Faraday have considered these stresses primary over the fields in determining the electrical forces. In particular, propagation of electromagnetic fields through an empty space could not be conceived and an elastic medium, the ether, was postulated. The stresses in Eqs. (5.3) and (5.10), were then associated with deformations of the ether and the electric force propagated via the contact with it. It was then confirmed that electric fields are primary quantities and that the electric force in a point in space solely depends on the **E**-field at that point, without any underlying support. In that sense, the stress formulation is rather a convenience than (essential) physical reality. What Eqs. (5.3) and (5.10) really mean is that the bulk force on the system of charges can be correctly calculated assuming the existence of a fictitious state of stress at the surface, [39].

5.2 Fluid dielectrics in electric field

We will now investigate some of the interesting phenomena arising when a *dielectric* is placed in an electric field. Unlike with conductors, external **E**-fields do not vanish inside the dielectrics and that greatly affects their thermodynamic properties. Of a particular interest to us are electric forces acting on a dielectric material as well as stresses on boundaries between two dielectrics.

Because of its generality we will follow the free-energy approach developed in Landau and Lifshitz [38]. The formalism is rather comprehensive and instead of deriving it all, we will borrow some of the main results. When necessary, the terms will be explained in more detail.

5.2.1 The internal and the free energy of a dielectric

Let a thermally insulated dielectric be placed in an external electric field produced by a set of charged conductors. If now the field undergoes an infinitesimal change, due to a slight change in the charges on the conductors, a work done in the process is

$$\delta W = \int_V \phi \, \delta\rho \, dV \tag{5.14a}$$

$$= \int_V \phi \boldsymbol{\nabla}\cdot\delta\mathbf{D} \, dV \tag{5.14b}$$

$$= \int_V -\boldsymbol{\nabla}\phi\cdot\delta\mathbf{D} \, dV + \int_S \phi \, \delta\mathbf{D}\cdot\mathbf{n} \, da \tag{5.14c}$$

$$= \int_V \mathbf{E}\cdot\delta\mathbf{D} \, dV. \tag{5.14d}$$

where we made use of $\boldsymbol{\nabla}\cdot\mathbf{D} = \rho$ and the fact that the surface integral in Eq. (5.14c) vanishes for a localized charge density ρ when S is taken to infinity. The volume integration is over the whole volume outside the conductor including the vacuum if the dielectric does not occupy all the space.

The well-known integral Eq. (5.14d) represents the increment of energy stored in the electrostatic field. Now both the total energy and the total free energy of the dielectric (each including also the energy of the electric field), change by this amount. The change of the internal energy U and the free energy F per unit volume are then

$$dU = \ TdS - pdV + \mu_c d\rho + \mathbf{E}\cdot d\mathbf{D}, \tag{5.15a}$$

$$dF = -SdT - pdV + \mu_c d\rho + \mathbf{E}\cdot d\mathbf{D}, \tag{5.15b}$$

where μ_c is the chemical potential with respect to unit mass[1]. A Legendre transforamtion from variable $\mathbf{D}$ to variable $\mathbf{E}$ is performed to get the new thermodynamic potentials $\tilde{U}(\mathbf{E})$ and $\tilde{F}(\mathbf{E})$

$$\tilde{U} = U - \mathbf{E}\cdot\mathbf{D}, \tag{5.16a}$$

$$\tilde{F} = F - \mathbf{E}\cdot\mathbf{D}, \tag{5.16b}$$

for which the thermodynamic relations become

$$d\tilde{U} = \ TdS - pdV + \mu_c d\rho - \mathbf{D}\cdot d\mathbf{E}, \tag{5.17a}$$

$$d\tilde{F} = -SdT - pdV + \mu_c d\rho - \mathbf{D}\cdot d\mathbf{E}. \tag{5.17b}$$

To find the internal and free energies per unit volume stored in a field, Eqs. (5.15a) and (5.15b) have to be integrated from the initial state $\mathbf{D} = 0$ till the final $\mathbf{D}$. If the medium is linear, $\mathbf{D} = \epsilon\mathbf{E}$, we get

$$U = U_0(S, V, \rho) + \frac{1}{2\epsilon}\mathbf{D}^2, \tag{5.18a}$$

$$F = F_0(T, V, \rho) + \frac{1}{2\epsilon}\mathbf{D}^2, \tag{5.18b}$$

where U_0 and F_0 are zero-field quantities. In similar way

$$\tilde{U} = U_0(S, V, \rho) - \frac{1}{2}\epsilon\mathbf{E}^2, \tag{5.19a}$$

$$\tilde{F} = F_0(T, V, \rho) - \frac{1}{2}\epsilon\mathbf{E}^2. \tag{5.19b}$$

The total internal and free energies, U_{tot} and F_{tot}, are obtained by integration of Eqs. (5.18a) and (5.18b) over all space.

Various thermodynamic potentials describing a system acquire minimal values in a state of thermal equilibrium, with respect to infinitesimal changes in the state of the

[1] In Chap. 3 chemical potential $\mu_{\rm chem}$ was defined with respect to concentration. These two differ by a constant factor since $\rho = c\,m$, where concentration $c = n/V$ is the number of particles per unit volume and m the mass of one particle

system, Landau and Lifshitz [40]. The thermal equilibrium in an electric field will depend whether the changes of the state are happening at the constant charges or the constant potentials. When the charges (and temperature) are held constant, the state of thermal equilibrium is characterized by the minima of U and F; when the potentials are constant, the state of equilibrium is described by the minima of $\tilde{U}$ and $\tilde{F}$. By inspecting Eqs. (5.18a) and (5.19a) we note that for linear dielectrics

$$\delta\tilde{U} = -\delta U. \tag{5.20}$$

The usefulness of the formalism can be illustrated by considering the change in the internal energy if the dielectric constant ϵ is changed. From Eq. (5.18a) we get

$$\delta U_{tot} = \int_V \frac{1}{\epsilon}\mathbf{D}\cdot\delta\mathbf{D}\, dV - \int_V \frac{1}{2\epsilon^2}\delta\epsilon D^2\, dV \tag{5.21a}$$

$$= \int_V \mathbf{E}\cdot\delta\mathbf{D}\, dV - \frac{1}{2}\int_V \delta\epsilon\mathbf{E}^2\, dV. \tag{5.21b}$$

If the charges are held constant, the first term in Eq. (5.21b) vanishes, being the charge contribution from Eq. (5.14a), and we get

$$\delta U_{tot} = -\frac{1}{2}\int_V \delta\epsilon\mathbf{E}^2\, dV. \tag{5.22}$$

Eq. (5.22) says that an increase in the dielectric constant somewhere inside the system reduces the electrostatic energy (with charges being fixed). On the other hand, when the potentials are kept constant, the energy *increases* by the same amount, Eq. (5.20).

5.2.2 The Maxwell stress tensor in fluid dielectrics

We have seen in Sec. 5.1 that a force acting on a finite volume can be represented as a stress applied to the surface of the volume. This general fact stems from the conservation of linear momentum, since the rate of change of momentum inside a volume can be represented as the momentum flux through its surface [41]. To find the force on a fluid dielectric placed inside an electric field we will have identical approach; that is, we want to find the stress tensor σ_{ik}^M satisfying

$$\int_V f_i\, dV = \int_S \sigma_{ik}^M n_k df. \tag{5.23}$$

As before, $\sigma_{ik}^M df_k$ is the i-th component of the force acting on a surface element df, with $\mathbf{n}$ being directed out of the volume. Once σ_{ik}^M is determined the force f_i can be found as, Eq. (5.2d)

$$f_i = \partial_k \sigma_{ik}^M. \tag{5.24}$$

There are several approaches to determine the stress tensor σ_{ik}^M in dielectrics, [39, 42, 38]. The most general method is described in Landau and Lifshitz [38]. Here we briefly describe the procedure[2]. A fluid dielectric is placed between two conducting planes held at

[2]The terms appearing in the stress tensor and in the resulting force are discussed below.

a constant potential. The planes are then subjected to an isothermal virtual displacement which causes the homogeneous deformations within the dielectric. The work done on the conducting planes is equal to the decrease in the free energy $\tilde{F}$ of the dielectric. The result of the procedure is the stress tensor σ_{ik}^M, which in case of isotropic and linear media, becomes the symmetric tensor

$$\sigma_{ik}^M = -\tilde{P}_0\delta_{ik} - \frac{1}{2}\epsilon_r\epsilon_0\left[1 - \frac{\rho}{\epsilon_r}\left(\partial_\rho\epsilon_r\right)_T\right]E^2\delta_{ik} + \epsilon_r\epsilon_0 E_i E_k. \tag{5.25}$$

Here $\tilde{P}_0(\rho, T)$ is the pressure present in the dielectric when $\mathbf{E} = 0$, while ∂_ρ is the partial derivative with respect to mass density. If we consider vacuum, $\epsilon_r = 1$, and neglect the pressure we recover Eq. (5.4). The term

$$c_e = \frac{\rho}{\epsilon_r}\left(\partial_\rho\epsilon_r\right)_T, \tag{5.26}$$

is called the electrostriction term and is in connection with the deformations imposed by the electric field.

5.2.3 Electric force in fluid dielectrics

Differentiating Eq. (5.25) according to Eq. (5.24) we get for the force per unit volume

$$\mathbf{f}^e = -\boldsymbol{\nabla}\tilde{P}_0(\rho, T) + \frac{1}{2}\epsilon_0\boldsymbol{\nabla}\left[E^2\rho\left(\partial_\rho\epsilon_r\right)_T\right] - \frac{1}{2}\epsilon_0 E^2\boldsymbol{\nabla}\epsilon_r + \rho_e\mathbf{E}, \tag{5.27}$$

where ρ_e is the density of free (external) charge. Eq. (5.27) is a very important result and represents the most general expression for the force on dielectric media placed in an electric field. Therefore, it is worth now to investigate how the terms came about.

Pressure

Generally, the pressure in compressible fluids is a function of mass density and temperature and a separate equation of state is needed to fully characterize the fluid systems. By the additional equation the pressure value is completely determined. We will investigate only incompressible liquids and therefore the pressure will appear only in the pressure gradient term in the force density of Eq. (5.27). This means that any constant pressure added to $\tilde{P}_0$ would yield the same motion. If we look at Eq. (5.25) we realize that the pressure term does play a role in the determination of stresses on a boundary between two media (to be considered later); however, there again it will enter as a pressure difference.

In passing we remark that non-unique pressure solutions in incompressible liquids is a known problem from computational fluid dynamics. Numerical algorithms are thus devised to deduce the pressure field in an iterative process, starting with a guessed initial value until a converged solution is reached.

Electrostriction

The electrostriction term of Eq. (5.26) gives rise to the second term in Eq. (5.27). As pointed, it arises due to the deformations of a dielectric in an electrostatic field.

Let us assume that the dielectric constant depends on position as well as density, $\epsilon = \epsilon(\mathbf{r}, \rho)$. When a dielectric is placed in an electrostatic field it undergoes a deformation since material points are displaced due to dipole formation. As a result, the mass density changes.

We introduce the displacement field $\mathbf{s}(\mathbf{r})$; a point inside the dielectric at a position $\mathbf{r}$ before the deformation, finds itself at the new position $\mathbf{r} + \mathbf{s}(\mathbf{r})$ afterwards. An initial small volume dV becomes a deformed dV'

$$dV' = (1 + \boldsymbol{\nabla}\cdot\mathbf{s})\, dV, \tag{5.28}$$

where $\boldsymbol{\nabla}\cdot\mathbf{s}$ is the volume dilatation up to the first order in $\mathbf{s}$, [Stratton]. Since mass is conserved we have

$$\rho dV = \rho'(1 + \boldsymbol{\nabla}\cdot\mathbf{s})\, dV, \tag{5.29}$$

where ρ and ρ' are the densities before and after the deformation, respectively. For an infinitesimal change

$$\delta\rho = \rho' - \rho = -\rho(\boldsymbol{\nabla}\cdot\mathbf{s}), \tag{5.30}$$

which results in the corresponding change of the dielectric constant

$$\delta_\rho\epsilon = (\partial_\rho\epsilon)\delta\rho = -\rho(\partial_\rho\epsilon)\boldsymbol{\nabla}\cdot\mathbf{s}. \tag{5.31}$$

If the above variation is inserted into the change of the electrostatic energy, Eq. (5.22), we eventually obtain the second term in Eq. (5.27).

The electrostriction term c for liquids could be estimated from Clausius-Mossotti equation[3]

$$\epsilon_r - 1 = \frac{N\alpha}{1 - \frac{1}{3}N\alpha}, \tag{5.32}$$

where N is number of atoms per unit volume and α molecular polarizability. Since $N = \beta\rho$ is proportional to the density, after a quick manipulation we get

$$c_e = \frac{1}{3\epsilon_r}(\epsilon_r - 1)(\epsilon_r + 2). \tag{5.33}$$

The relative dielectric constant ϵ_r is always bigger than 1 resulting in a positive electrostriction term c. It is worth mentioning that in Ref. [43] performed a set of experiments with perpendicular and tangential electric fields imposed on the boundary between two liquid dielectrics. The electrostriction effects, although present, were much less than suggested by Eq. (5.33).

Generally, the electrostriction involves change in shape of the dielectric. For a slight deformation, that is for small **E**-fields, the first order effect include a volume expansion without the change in shape. Therefore, the effect can be described as an effective pressure on the dielectric. Due to the large **E**-fields present in microfluidic systems, order of 10^5 V/m, the effects of the electrostriction could be quite significant. In case of incompressible liquids, however, we can in first approximation treat the deformation as small

[3]For water, or polar molecules in general, the equation does not apply and the approach developed by Onsager must be used, [44].

(ρ = const.) and so group the electrostriction term with $\tilde{P}_0$ into a redefined pressure. As already mentioned, such a procedure will not affect the equations of motion. We can rewrite Eq. (5.27)

$$\mathbf{f} = -\boldsymbol{\nabla}\left[\tilde{P}_0 - \frac{1}{2}\epsilon_0 E^2 \rho \left(\partial_\rho \epsilon_r\right)_T\right] - \frac{1}{2}\epsilon_0 E^2 \boldsymbol{\nabla}\epsilon_r + \rho^e \mathbf{E}. \tag{5.34}$$

Inhomogeneity
The term proportional to $\boldsymbol{\nabla}\epsilon$ gives the force contribution due to the non-homogeneous dielectric constant. Since $\epsilon = \epsilon(\mathbf{r}, \rho)$, the small element of the dielectric positioned at $\mathbf{r}$ after the deformation was at the point $\mathbf{r} - \mathbf{s}$ before; the contribution to $\delta\epsilon$ due to the inhomogeneity is

$$\delta_r \epsilon = -\mathbf{s}\cdot\boldsymbol{\nabla}\epsilon, \tag{5.35}$$

which together with Eq. (5.22) leads to the third term in Eq. (5.27).

In general ϵ is a function of density, temperature and (mixture) concentration c which generally depends on position. We have

$$\boldsymbol{\nabla}\epsilon = (\partial_\rho \epsilon)_{T,c}\boldsymbol{\nabla}\rho + (\partial_T \epsilon)_{\rho,c}\boldsymbol{\nabla}T + (\partial_c \epsilon)_{\rho,T}\boldsymbol{\nabla}c. \tag{5.36}$$

For incompressible, non-homogeneous liquid at constant temperature the force will depend on the concentration gradient. In microfluidics, the systems used for analytical methods, for example separations, consist of usually two miscible liquids - a buffer and a sample. Due to diffusion, their interface will eventually acquire transitional dielectric constant (and conductivity), which will contribute to the force in proportion to Eq. (5.36).

5.2.4 Alternative form of the force density

The equation Eq. (5.27) has been derived from the energy principle. The derivation was first proposed by Korteweg and later developed by Helmholtz in 1881.

An alternative way to obtain the force on a dielectric placed in an **E**-field is to suppose that the electric forces exerted on free charge and polarization charge (dipoles) are transferred directly to the dielectric, [45, 46]. Since the force on a single dipole is $\mathbf{p}\cdot\boldsymbol{\nabla}\mathbf{E}$, then for single-species material with N_d dipoles per unit volume we have

$$\mathbf{f} = N_d\, \mathbf{p}\cdot\boldsymbol{\nabla}\mathbf{E} = \mathbf{P}\cdot\boldsymbol{\nabla}\mathbf{E}, \tag{5.37}$$

where $\mathbf{P} = N_d\, \mathbf{p}$ is the polarization density. Now, $\mathbf{P} = (\epsilon - \epsilon_0)\mathbf{E}$ and $\boldsymbol{\nabla}\times\mathbf{E} = 0$. With the use of known vector identities

$$\mathbf{V}\cdot\boldsymbol{\nabla}\mathbf{V} = (\boldsymbol{\nabla}\times\mathbf{V})\times\mathbf{V} + \frac{1}{2}\boldsymbol{\nabla}(\mathbf{V}\cdot\mathbf{V}), \tag{5.38a}$$

$$\boldsymbol{\nabla}(\phi\psi) = \phi\boldsymbol{\nabla}\psi + \psi\boldsymbol{\nabla}\phi, \tag{5.38b}$$

we can transform Eq. (5.37) into

$$\mathbf{f} = \frac{1}{2}\epsilon_0 \boldsymbol{\nabla}\left[(\epsilon_r - 1)E^2\right] - \frac{1}{2}\epsilon_0 E^2 \boldsymbol{\nabla}\epsilon_r. \tag{5.39}$$

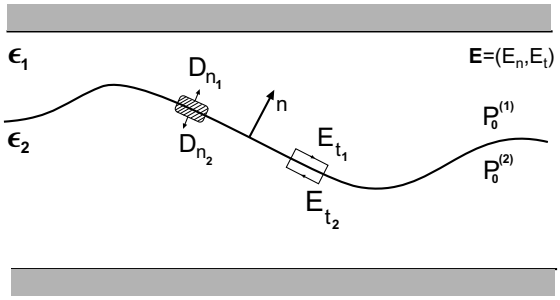

Figure 5.2: A disturbed interface between two liquid dielectrics. In case of perfect dielectrics, the stresses are normal to the interface causing a change in pressure, $\| P_0 \| = \| \frac{1}{2}\epsilon \left(E_n^2 - E_t^2 \right) \|$.

Comparing Eq. (5.27) (without the free-charge term) and Eq. (5.39) we see that they are not identical. It is not surprising since Eq. (5.27) is not restricted to dipoles - multipoles could in principle be present[4]. The two expressions will be equal when

$$\left(\partial_\rho \epsilon_r \right)_T = c_1 = \frac{\epsilon_r - 1}{\rho}, \tag{5.40}$$

or, when

$$\epsilon_r = 1 + c_1 \rho. \tag{5.41}$$

But Eq. (5.41) is just the first term in the expansion of ϵ_r in terms of ρ. So if the compressions are assumed small, the two equations could be made identical. This is in support of the previous statement that in the case of incompressible liquids, the deformations, manifesting themselves as a pressure, do not affect the motion.

However, if the compressibility is significant the approach leading to Eq. (5.39) will not give correct results. Once calculated, the polarization force could indeed be used to predict the corresponding deformation; but in turn the deformation affects the polarization, and if this change is not included the prediction will be only approximative. Such an erroneous attempt is discussed in Ref. [39]. If a force description is used it is important to account for all possible contributions which is usually difficult. The difficulties are circumvented in the (free) energy approach, used to obtain Eq. (5.27).

5.2.5 The boundary between two dielectrics

We will now consider the boundary conditions at the interface between two incompressible liquid dielectrics placed next to each other, Fig. 5.2. Let us first introduce a notation which will be of extensive use in later chapters. The "jump" in a function $f(x, y, z)$ at the boundary $z = z_0$ between two media represents the change in the function f across the

[4]The relationship between vectors $\mathbf{D}$ and $\mathbf{E}$ can be written as $D_i = \epsilon_0 E_i + (P_i - \sum_j \partial_j Q'_{ij} + ...)$, where Q'_{ij} is the macroscopically averaged electric quadrupole moment, [15]. The higher terms containing derivatives, however, are vanishingly small in comparison with the terms that do not contain them.

boundary

$$\| f \| \equiv f(x, y, z = z_0^+) - f(x, y, z = z_0^-) = (f_2 - f_1)_{z=z_0}, \tag{5.42}$$

where + and − refer to the different sides, 2 and 1 respectively, of the boundary.

If the normal vector $\mathbf{n}$ is directed from the medium 2 into the medium 1, we can write the known conditions imposed on $\mathbf{E}$ and $\mathbf{D}$ fields at the boundary between two media as

$$\mathbf{n} \times \| \mathbf{E} \| = \| E_t \| = 0, \tag{5.43}$$

$$\mathbf{n} \cdot \| \mathbf{D} \| = \| D_n \| = -q_s, \tag{5.44}$$

expressing the continuity of the tangential component E_t across the interface, and the jump in the normal component D_n due to a surface charge density.

The forces at each side of the interface are equal and opposite. In terms of the stress tensor σ_{ik}^M we have

$$\| \sigma_{ik}^M \| \, n_k = 0. \tag{5.45}$$

In Eq. (5.25) we can put the electrostriction term into a redefined pressure P_0, and express the $\mathbf{E}$-field in terms of normal and tangential components. We get for the normal stresses

$$\| P_0 \| = \| \frac{1}{2} \epsilon \left(E_n^2 - E_t^2 \right) \| = \frac{1}{2} \| \epsilon E_n^2 \| - \frac{1}{2} E_t^2 \, \| \epsilon \|, \tag{5.46}$$

and for the tangential stresses

$$\| E_t D_n \| = E_t \, \| D_n \| = -E_t q_s, \tag{5.47}$$

where the use has been made of Eqs. (5.43) and (5.44).

Several important remarks need to be underlined. We have already seen in Sec. 5.1 that an $\mathbf{E}$-field acts as an effective pressure with the normal and tangential components suppressing each other's contribution, and that is what the balance of normal stresses in Eq. (5.46) reveals.

In case of perfect dielectrics, $q_s = 0$, or in case when the interface is perfectly conducting, $E_t = 0$, the equality of tangential stresses in Eq. (5.47) is satisfied identically. This means, that for these cases the electric stresses are always perpendicular to the interface. Alterations of interface shape together with the surface tension serve to balance the electric stress.

If there are free charges accumulated at the interface, a tangential $\mathbf{E}$-field acting on the charge will produce a net tangential stress. In case of liquids, a *viscous* flow will result to produce the stresses to balance the action. This will be shown in Chap. 7. In other words, an inviscid approximation in the case of free charge at the interface will not be a valid one. This is the mechanism behind realistic, leaky dielectrics with small but finite conductivities, Saville [46].

Chapter 6

Hydrodynamic stability analysis: basics

By a dynamical system we mean any physical system that evolves in time; it could be an atom, a swinging pendulum or a general hydrodynamic flow to which we will focus our attention. A dynamical system is said to be unstable if a small perturbation of its equilibrium state increases exponentially in time [37].

For any viscous flow that is subject to steady conditions the equations of motion, Eq. (2.8), will yield in principle the exact steady solutions, Landau-Lifshitz [14]. Simple examples of the exact (analytical) steady solutions of the flow equations are Poiseuille and Couette flows. However, these stationary solutions exist only within certain range of the relevant flow parameters defined by Reynolds' or other dimensionless numbers. Within this *stable* range any fluctuation imposed on the stationary flow will decay in time leaving the steady solution unaltered. Outside the range, the small fluctuations which are always present within the flow will destabilize the flow and the stationary solution will seize to exist. The outside regime is termed *unstable*. Such transitions from stable to unstable regimes are the topic of hydrodynamic stability analysis and have been the centerpiece of enormous number of research studies dating all the way from 19-th century, [47, 48, 49, 50], to name a few.

The flow instabilities have a big practical impact. In large systems they result in turbulence and big energy losses associated with fluid transport, and are thus undesirable. In microfluidic systems, devices such as EOF pumps require operational stability while some of them, such as mixers or microdispensers, would benefit from the instability.

In this chapter we will try to introduce general concepts of the linear stability analysis. We would like to find a systematic way to quantitatively separate stable from unstable flow regimes. In later chapters, the analysis will be applied to a specific problem of interface stability between two immiscible liquids in microfluidic systems.

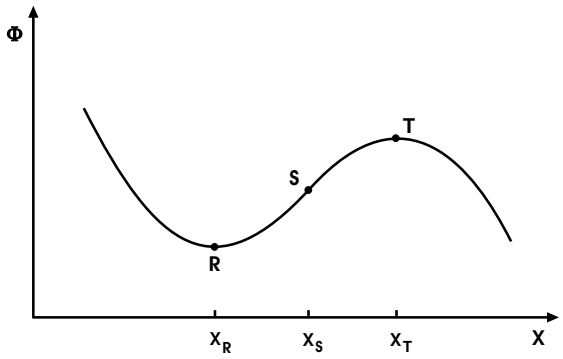

Figure 6.1: Typical potential energy ϕ of a conservative system. The points R, S, and T characterize the stable, neutral and unstable equilibrium, respectively.

6.1 General concepts

Conservative systems
If we consider a one-dimensional conservative system, its equation of motion is described by

$$m\frac{d^2x(t)}{dt^2} = f(x), \tag{6.1}$$

where m is a constant parameter having different meaning for different conservative systems and $f(x)$ is an analytical function.

In a mechanical system m represents a point mass and $f(x)$ force which can be expressed as negative gradient of the potential energy $\phi(x)$. Generally, the potential energy consists of local minima and maxima and can be depicted as in Fig. 6.1. The force appearing when a system is moved the distance δx_P away from an arbitrary but fixed point can be found by a Taylor expansion

$$(\partial_x\phi)_{x_P+\delta x_P} = (\partial_x\phi)_{x_P} + (\partial_{xx}\phi)_{x_P}\delta x_P + ... \tag{6.2}$$

Discarding the terms higher than linear and expanding around the points where $\partial_x\phi = 0$ (any of the three marked points in Fig. 6.1), we have

$$(\partial_x\phi)_{x_P+\delta x_P} \approx (\partial_{xx}\phi)_{x_P}\delta x_P, \tag{6.3}$$

which gives the equation of motion of a point mass in terms of small displacement δx_P:

$$m\partial_{tt}\delta x_P = -(\partial_{xx}\phi)_{x_P}x_P. \tag{6.4}$$

The solutions of the above equation can be expressed as

$$\delta x_P(t) = \pm\delta x_{P0}\exp(-i\omega_P t), \tag{6.5}$$

where ω_P is the frequency of oscillations given by

$$\omega_P^2 = \frac{1}{m}(\partial_{xx}\phi)_{x_P}. \tag{6.6}$$

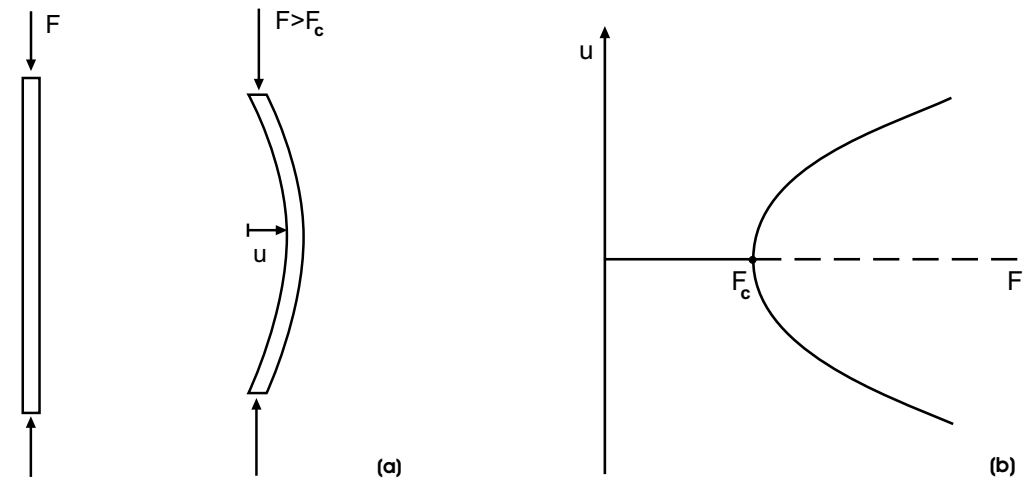

Figure 6.2: (a) Buckling of a solid rectangular beam upon exerting a vertical force. The displacement **u** increases with F. (b) "Pitchfork" bifurcation diagram: maximal displacement $\mathbf{u}(F)$ as function of the force F. After critical F_c, two stable states appear. The former stable (undistorted) state exists but has become unstable (dashed line).

From Eq. (6.6) we notice that the frequency ω_P depends on the curvature of the potential energy, given by the second derivative or generally the Laplacian. The point x_R in Fig. 6.1 is the local minimum, and so the curvature is positive resulting in real ω_R. The point mass m experiences an oscillatory behavior, since the restoring force is directed towards the stable equilibrium point x_R. For the point x_T, however, the curvature is negative and ω_T is a complex number. In this case (or whenever the imaginary part of the frequency is positive) Eq. (6.5) shows that the displacement δx_T will exponentially grow in time. At the point T the system is in an unstable state of higher energy, the restoring force now directed away from it.

A system can undergo a change from a stable to an unstable state, passing through the point of *marginal* or *neutral stability* where the frequency is equal to zero i.e., the curvature changes the sign. In our case this is valid for the point x_S. In order to find the force on the mass m at that point, we need to include the higher terms in the expansion of Eq. (6.2).

The instability transitions can be visualized in parameter space by means of *bifurcation* diagrams. For that we use another example of a solid beam on which a vertical force is applied. After a certain critical force (Euler force), the beam will buckle and will deform as depicted in Fig. 6.2 (a).

If we now plot the maximal displacement $\mathbf{u}(F)$ as a function of the force F, then the qualitative graph looks like the one in Fig. 6.2 (b). After a critical force F_c is applied two new stationary states appear; the former equilibrium state, although still exists, becomes unstable. This outlines the *principle of exchange of stabilities* manifested when at the onset of instability stationary solutions prevail [49].

Dissipative systems
Unlike the conservative systems, dissipative systems, such as viscous fluids, exchange energy, volumes, particles, etc. with their surroundings, resulting in fluctuations of these variables. The concept of stable and unstable equilibria is still valid, [37], with mass particles now being subjected to a dissipative retarding force; oscillations are damped, and the system, driven by fluctuations, cannot infinitely stay in an unstable state of highest energy.

In order for a flow to be stable, it has to be stable with respect to every possible disturbance to which it can be subject; contrary, it will be unstable if only one particular disturbance grows in time. The conditions under which instability starts are usually expressed in terms of some critical parameters governing the flow.

Of a special interest are marginal stability states marking the onset of instability and thus dividing stable from unstable regimes. Unlike the conservative systems, dissipative systems have two different types of the marginal states, depending on the way the flow perturbations grow/decay, [49]. In stationary marginal states perturbations grow/decay aperiodically and the principle of the exchange of stabilities is applicable - the instability is manifested as a secondary flow e.g. Bénard cells appearing in the case of thermal instability. In oscillatory marginal states perturbations oscillate with growing/decaying amplitudes. An oscillatory growth transition is termed *overstability*. A tangential electric field imposed on the boundary between two viscous, conducting liquids can cause the oscillatory marginal states.

6.2 Standard procedure in linear stability analysis

We will now summarize the usual procedure in hydrodynamic linear stability analysis in terms of four basic steps.

1. The equations are set for the initial, stationary (unperturbed) flow resulting in the velocity field $\mathbf{v}_0$. The hydrodynamic equations include the continuity equation, the momentum and energy equations. In case of electrohydrodynamics the Maxwell equations for electroquasistatic fields need to be included as well. The equations are simplified if incompressible liquids are considered.

2. A small (infinitesimal) perturbation $\mathbf{v}'$ is superposed to the main velocity $\mathbf{v}_0$ and the equations governing the perturbation are obtained. The equations and the boundary conditions are then linearized neglecting the terms with quadratic and higher terms in $\mathbf{v}'$ [1].

3. The small disturbance $\mathbf{v}'$ is expanded into a complete set of normal modes characteristic for the system with given boundary conditions. For example, if a system is confined between two infinitely long horizontal planes with normals in z direction, and the flow parameters (density, viscosity etc.) depend only on the z coordinate,

[1] The general case of finite disturbances would require inclusion of non-linear (higher order) terms.

the expansion in term of two-dimensional normal modes is

$$\mathbf{v}'(\mathbf{r},t) = \int d\mathbf{k}\, v_{\mathbf{k}}(z) \exp(-i\omega_{\mathbf{k}} t) \exp[i(\mathbf{k}\cdot\mathbf{r})]. \tag{6.7}$$

where we have separated the space and the time dependence of normal modes.

4. Finally, a normal mode

$$\mathbf{v}'_k(\mathbf{r},t) = v_{\mathbf{k}}(z) \exp(-i\omega_{\mathbf{k}} t) \exp[i(\mathbf{k}\cdot\mathbf{r})], \tag{6.8}$$

where $\mathbf{k}$ serves as a parameter, is put into the system of linearized equations. By choosing the solution in the form of Eq. (6.8), the linear PDE system of equations and boundary conditions describing $\mathbf{v}'$ becomes a simpler linear ODE system[2]. The problem is then transformed to an eigenvalue problem for $\omega_{\mathbf{k}}$ which is generally a complex number.

We have mentioned that in unstable systems the disturbances exponentially grow in time, whereas in stable systems they decay. Different stability regimes impose different conditions on $\omega_{\mathbf{k}}$. These can be found by considering the time dependence $\exp(-i\omega t)$ given by Eq. (6.8). If $\omega_{\mathbf{k}} = \operatorname{Re}\omega_{\mathbf{k}} + i \operatorname{Im}\omega_{\mathbf{k}}$ is inserted into Eq. (6.8), the stability regimes can be distinguished as follows:

$$\operatorname{Im}\omega_{\mathbf{k}} \begin{cases} > 0 & \rightarrow \text{ instability,} \\ = 0 & \rightarrow \text{ marginal (neutral) stability for } \mathbf{k}_{1c}, \\ < 0 & \rightarrow \text{ stability.} \end{cases} \tag{6.9}$$

The critical wave number $\mathbf{k}_c$ marks the border between the stable and unstable states, see Fig. 6.2 (b). We can also make the distinction between the oscillatory and the stationary marginal states. Let $\operatorname{Re}\omega_{\mathbf{k}} \neq 0$. Then in accordance with Eq. (6.9)

$$\operatorname{Re}\omega_{\mathbf{k}} \neq 0 \ \wedge\ \operatorname{Im}\omega_{\mathbf{k}} \begin{cases} > 0 & \rightarrow \text{ overstability,} \\ = 0 & \rightarrow \text{ stability or marginal overstability for } \mathbf{k}_{2c}, \\ < 0 & \rightarrow \text{ stability.} \end{cases} \tag{6.10}$$

An oscillatory marginal state exists when the real part of the frequency $\omega_{\mathbf{k}}$, which determines oscillatory behavior, is different from zero when the imaginary part is zero. If $\operatorname{Im}\omega_{\mathbf{k}} = 0$ for all $\mathbf{k}$-s, we are in a stable regime; when $\operatorname{Im}\omega_{\mathbf{k}} > 0$ at some value $\mathbf{k}_{2c}$, then overstability sets in. On the other hand, if $\operatorname{Im}\omega_{\mathbf{k}} = 0$ implies $\operatorname{Re}\omega_{\mathbf{k}} = 0$ for every $\mathbf{k}$, the marginal state is stationary and the principle of exchange of stabilities is valid [49].

Our main goal in the next chapters is to determine the characteristic frequency $\omega_{\mathbf{k}}$ as well as the critical wave number $\mathbf{k}_c$ manifested at the onset of instability. In electrohydrodynamics, the $\mathbf{k}_c$ will depend on the applied voltage.

[2]The formal analysis is presented in Chap. 7.

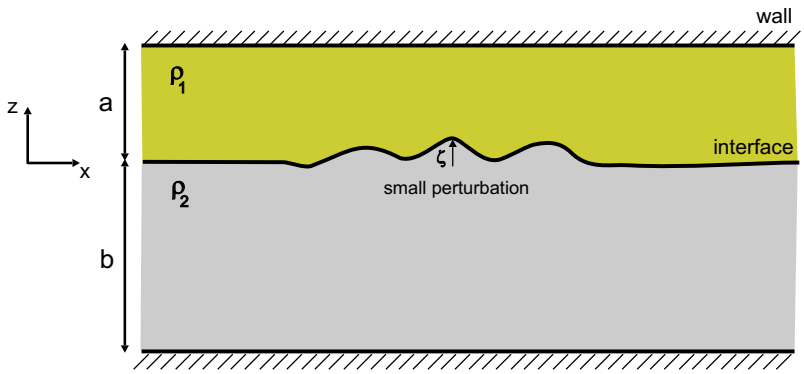

Figure 6.3: Two liquids of different densities confined between two infinite planes. The distances from the interface are a and b for the liquids 1 and 2, respectively. The vertical displacement of the interface during perturbations is $\zeta(x,t)$.

6.3 Example: The Rayleigh-Taylor instability

To illustrate some of the outlined ideas we will now give a simple example of gravitational instability. A note to the reader is that the boundary conditions on interface and wave numbers used here will be borrowed from the chapter ahead, where the general treatment is made.

Consider two ideal incompressible liquids on top of each other and confined between two infinitely long, horizontal planes, Fig. 6.3. The densities of the upper and lower liquids are $\rho^{(1)}$ and $\rho^{(2)}$, respectively, and the surface tension is σ. The liquids are assumed to be motionless in the beginning. We want to find the characteristic frequencies when the interface is slightly perturbed i.e. $z = \zeta(x,t)$.

The ideal liquids which are vorticity-free in the beginning, are vorticity-free in subsequent times by the conservation of circulation i.e. Kelvin's theorem, [14]. The flow is therefore potential and the velocity in each of the liquids given by

$$\mathbf{v}^{(i)} = \boldsymbol{\nabla}\phi^{(i)}, \tag{6.11}$$

where $i = 1, 2$ and $\phi = \phi(t)$. Inserting the above velocity into the Euler's equation for incompressible flow, Eq. (2.8) with zero viscosity, we get generalization of Bernoulli's theorem for time dependent flow

$$\rho^{(i)}\partial_t\phi^{(i)} + \frac{1}{2}\rho^{(i)}\mathbf{v}^{(i)2} + \rho^{(i)}gz + p(i) = f(t). \tag{6.12}$$

Since the potential $\phi(t)$ is not uniquely determined, it can be redefined by a time transformation $\phi(t) = \phi(t) + tf(t)/\rho$ without loss of generality[3]. We can thus eliminate $f(t)$ from Eq. (6.12). If the velocities are small the quadratic term can also be neglected and we get for the pressures anywhere in the liquids

$$p^{(i)} = -\rho^{(i)}gz - \rho^{(i)}\partial_t\phi^{(i)}. \tag{6.13}$$

[3]Adding an arbitrary function of time to ϕ in Eq. (6.11) does not change the velocity.

At the rigid boundaries a and b, the vertical velocities $w^{(1)}$ and $w^{(2)}$ are zero; from Eq. (6.11) we then find

$$\begin{aligned}\phi^{(1)} &= A\cosh k(z-a)\exp[i(kx-wt)],\\ \phi^{(2)} &= B\cosh k(z+b)\exp[i(kx-wt)],\end{aligned} \tag{6.14}$$

for the waves propagating in the x-direction.

The conditions at the interface $z=\zeta$, Eqs. (7.13a) and (7.13b), and Eq. (7.13e), become

$$\| w(0) \| = \| \partial_z \phi(0) \| = 0, \tag{6.15a}$$

$$\partial_z \phi^{(1)}(0) = \partial_z \phi^{(2)}(0) = \partial_t \zeta, \tag{6.15b}$$

$$\| -p \| = \sigma \nabla_s^2 \zeta, \tag{6.15c}$$

where we evaluated the derivatives at $z=0$ since the oscillations are small. Inserting the pressure from Eq. (6.13) into Eq. (6.15c) we get

$$\| \rho g \zeta + \rho\, \partial_t \phi(\zeta) \| = \sigma \nabla_s^2 \zeta, \tag{6.16}$$

which after differentiation with respect to time and using Eq. (6.15b), gives the condition on the potential ϕ

$$\| \rho g \partial_z \phi(0) + \rho \partial_{tt} \phi(0) \| = \sigma \partial_z \left[\partial_{xx}\phi(0) + \partial_{yy}\phi(0) \right]. \tag{6.17}$$

Inserting the solutions from Eq. (6.14) into the conditions Eqs. (6.15a) and (6.17) we arrive at two algebraic equations for two unknowns A and B. The frequency ω_k is determined when the determinant of the system vanishes:

$$\omega_k^2 = \frac{(\rho^{(2)} - \rho^{(1)})gk + \sigma k^3}{\rho^{(1)} \coth(ka) + \rho^{(2)} \coth(kb)}. \tag{6.18}$$

If $\rho^{(2)} > \rho^{(1)}$, ω is always positive and the oscillations are stable, Eq. (6.10). However, if $\rho^{(2)} < \rho^{(1)}$, the first term in Eq. (6.18) changes the sign and the system becomes unstable for a range of k-s. From the condition $\omega^2 = 0$ we find for the critical wave number and wavelength,

$$k_c = \sqrt{\frac{(\rho^{(1)} - \rho^{(2)})g}{\sigma}}, \tag{6.19}$$

$$\lambda_c = \frac{2\pi}{k_c} = 2\pi \sqrt{\frac{\sigma}{(\rho^{(1)} - \rho^{(2)})g}}. \tag{6.20}$$

For perturbations with $k < k_c$, or $\lambda > \lambda_c$, $\mathrm{Im}\omega_k < 0$ and the interface is unstable. From the energy point of view, the decrease in the gravitational potential energy is larger than the

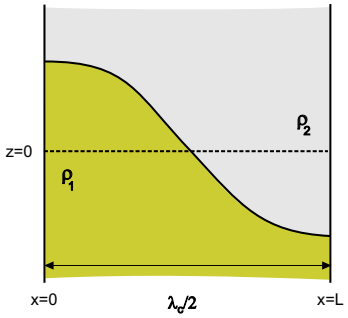

Figure 6.4: The onset of instability of the system with a heavier liquid on top of a lighter one. In a container of length L, the smallest non-zero wave number consistent with the boundary conditions is $k_L = \pi/L$ corresponding to $\lambda_L = 2L$. Instability starts when $\lambda_L = \lambda_c$, and is present when $\lambda_L > \lambda_c$ i.e. when L exceeds the critical length L_c, Eq. (6.21).

increase in the surface energy, and so the system goes into the more stable configuration. The elegant energy argument leading to the same Eqs. (6.19) and (6.20) is outlined in [37].

In finite-size systems not all of the wavelengths can be realized. The boundary conditions on possible wave numbers imposed in a rectangular channel are given by Eq. (8.27). We imagine now that the vertical boundaries are far apart, $ka, kb \gg 1$ in Eq. (6.18), and that the liquids are confined between walls at $x = 0$ and $x = L$, as in Fig. 6.4.

The wavelength associated with the smallest allowable wave number $k_L = \pi/L$ is $\lambda_L = 2L$. The instability will happen if this wavelength becomes greater than the critical λ_c i.e. if the length L of the system exceeds the smallest length enabling the onset of instability

$$L > L_c = \pi\sqrt{\frac{\sigma}{(\rho^{(1)} - \rho^{(2)})g}}. \tag{6.21}$$

For a water-oil system $L_c = 15$ mm, and for water-air $L_c = 8.9$ mm. In microfluidic channels typical widths are 100 μm while lengths can vary. For the systems shorter than L_c the Rayleigh-Taylor instability will not appear.

6.3.1 A note on viscosity

The stability analysis involving two superposed *viscous* fluids is substantially more involved. Here we only mention an important conclusion of the analysis made in Ref. [49] which says that the critical wavelength λ_c, Eq. (6.20), at which the gravitational instability sets in, is *not* affected by the presence of viscosity. In other words, "the wave numbers stabilized by the surface tension are independent of viscosity", [49].

In microfluidic regime gravity effects can be neglected since the surface tension is the dominant force. From Eq. (6.18) we see that the onset of instability in such case starts at $k = 0$ [4], with the other wave numbers being stabilized by the surface tension. It was just mentioned that these wave numbers are not affected by viscosity. In this limit also

[4] It will be more evident in Chap. 8.

the beginning of instability is independent of viscosity. Even though the viscous stresses are important in microfluidics, $Re \ll 1$, as far as the onset of instability is concerned, the inviscid approximation will suffice. For any realistic and thorough analysis, however, the viscosity must be included.

Chapter 7

Interfaces in electrohydrodynamics: theory

In this chapter we will apply the theory and concepts of the previous two chapters to the problem of hydrodynamic stability of the interface between two dielectric liquids. The results of the electrohydrodynamic (EHD) instability analysis will later be applied to two immiscible liquids placed in an **E**-field in a microfluidic devices. As already mentioned the influence of the electric fields is very important in microsystems since very large electric fields can be achieved with applying small voltages. To give an idea, a voltage of 10 V applied across the typical 100 μm will give 10^5 V/m. As far as the stability is concerned, the different situations will occur depending whether the E-field is applied perpendicular or tangential to the interface.

The problem of electrohydrodynamic (EHD) instability is not new. Many studies have been conducted over the years. The pioneering theoretical work started with Lord Rayleigh in 1882, [51], but the foundations of the EHD could be credited to Taylor and Melcher, namely for establishing the leaky dielectric model and extensively developing the theory, [52]. Many later contributions are listed in Saville [46]. With the development of microfluidic systems through 1990s, the EHD aspects are reappearing in the light of new applications.

7.1 Two immiscible liquids between infinite planes

In Chap. 4 we introduced a pump where a conducting liquid driven by EOF is used to pump a non-conducting liquid by viscous drag.

Although the actual design and characteristics of the pump have been investigated, no stability analysis has been performed yet. The full stability analysis of the system, however, is a rather involved procedure: the liquids differ in densities, viscosities, dielectric constants, and conductivities; they are moving and are subject to both normal and tangential **E**-fields in a finite-size system. In addition, the electrokinetic effects generally play the role since the pump is driven by EOF. Actually, the pump represents a jet of oil (i.e. the two interfaces) entering the surrounding water, Fig. 7.1 (a).

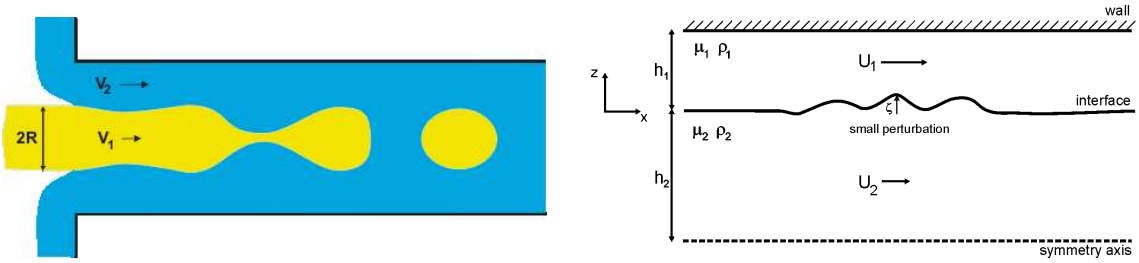

Figure 7.1: Two-liquid instabilities in electrohydrodynamics (a) Schematic view of the jet instability present in the two-liquid viscous pump. (b) Two moving or still liquids placed in an **E**-field between infinitely long planes spaced by $L_0 = a + b$.

In order to get the insight how various physical parameters affect the stability of the interface, we will restrict our initial analysis. This will give us a good starting point for a later, more realistic one.

As sketched in Fig. 7.1 (b) we will consider two immiscible, non-moving liquids one above the other, which are confined between two horizontal planes. Liquids are assumed incompressible and homogeneous perfect dielectrics separated by a plane interface. The effects of gravity, surface tension, the electrical and viscous forces will then successively be added. Each of these forces will eventually contribute a term in the characteristic equation for the normal mode frequencies. In this chapter we want to find general solutions and boundary conditions resulting when the interface is slightly perturbed.

The following notation will be in place: superscripts (1) and (2) are used for the two regions, while subscripts are used for vector components. The exceptions are the superscript $'$ indicating a perturbed variable, and the subscript 0 relating exclusively to the unperturbed variables.

Our analysis will distinguish two cases: the case in which the imposed **E**-field is normal to the (still) interface, and the case in which the **E**-field is tangential. To shorten the notation, the variables pertaining to the two cases will be presented in the curly brackets as

$$\begin{Bmatrix} N \\ T \end{Bmatrix} \tag{7.1}$$

where the upper values correspond to the case of normal **E**-field and the lower values to the case of tangential **E**-field.

Finally, in this chapter the symbol T_{ik}^M will be used for the Maxwell stress tensor containing only the electrical terms. We will lump together the electrostriction term into the zero-field pressure p which will be pulled out of Eq. (5.25) for the sake of transparency.

7.1.1 The governing equations

For each of the liquids in Fig. 7.1 (b), we summarize the equations of motion and of the electric fields

$$\rho^{(i)}\frac{D\mathbf{u}^{(i)}}{Dt} = -\boldsymbol{\nabla}p^{(i)} + \mu^{(i)}\nabla^2\mathbf{u}^{(i)} + \rho^{(i)}\mathbf{g} + \boldsymbol{\nabla}\cdot T^{M\,(i)}, \tag{7.2}$$

$$\boldsymbol{\nabla}\cdot\mathbf{u}^{(i)} = 0, \tag{7.3}$$

$$\boldsymbol{\nabla}\cdot(\epsilon^{(i)}\mathbf{E}^{(i)}) = 0, \tag{7.4}$$

$$\boldsymbol{\nabla}\times\mathbf{E}^{(i)} = 0, \tag{7.5}$$

where $\mathbf{u}^{(i)}(x,y,z) = (u^{(i)}, v^{(i)}, w^{(i)})$. In homogeneous perfect dielectrics the electric force per unit volume (inside the bulk) in Eq. (7.2) is zero. This can be seen from Eq. (5.27) as the terms including $\boldsymbol{\nabla}\epsilon$ and free charge ρ_e both vanish. So the coupling with the electric fields happens at the interface, and for that we will need to specify the boundary conditions. The only remaining body force in Eq. (7.2) is gravity.

7.1.2 General boundary conditions: rigid boundaries

On the rigid horizontal boundary planes at $z = a$ and $z = -b$ the no-slip condition is assumed for the velocities

$$\mathbf{u}^{(1)} = 0 \qquad (z = \quad a), \tag{7.6a}$$

$$\mathbf{u}^{(2)} = 0 \qquad (z = -b). \tag{7.6b}$$

The boundary conditions on **E** and **D**-fields are given by Eqs. (5.43) and (5.44), respectively. In case of a normal **E**-field, Fig. 7.2 (a), it is assumed that both rigid planes are perfectly conducting electrodes kept at a constant potential V, and in direct contact with the liquids. The two electrodes are large enough so that the fringing fields close to the edges are not important. For small microfluidic systems the electrodes could always be made in such a way as to ensure a uniform field. From Eq. (5.43),

$$\mathbf{n}\times\mathbf{E}^{(1)} = 0 \qquad (z = \quad a), \tag{7.7a}$$

$$\mathbf{n}\times\mathbf{E}^{(2)} = 0 \qquad (z = -b). \tag{7.7b}$$

In case of imposed tangential fields, Fig. 7.2 (b), the situation is different. We assume that the liquids are placed in a uniform horizontal field produced from two large electrodes spaced far apart. This is particularly valid for microfluidic case where the distance between the confining planes is very small. The plane boundaries are assumed insulating. Thus. the tangential component is continuous across all the boundaries and it will suffice to consider the normal E-field component

$$\mathbf{n}\cdot\mathbf{E}^{(1)} = 0 \qquad (z = \quad \infty), \tag{7.8}$$

$$\mathbf{n}\cdot\mathbf{E}^{(2)} = 0 \qquad (z = -\infty). \tag{7.9}$$

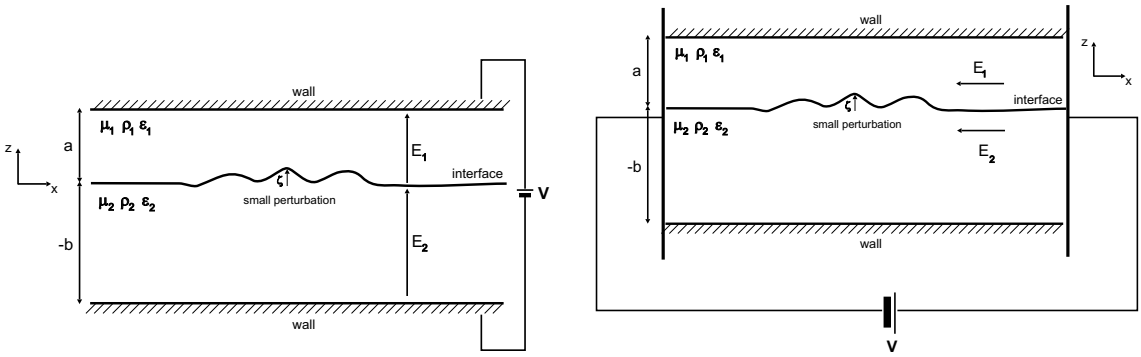

Figure 7.2: Two-liquid interface perturbations (a) in a normal **E**-field (b) and in a tangential **E**-field.

7.1.3 General boundary conditions: the interface

We will now describe main features of deformable interface between two fluids, Fig. 7.1 (b). General expressions provided below will be linearized later since we are interested in small deformations.

When unperturbed, the interface is described by the equation $z = 0$. Upon deformation it is given by

$$z = \zeta(x, y, t), \tag{7.10}$$

where ζ is the vertical displacement from the equilibrium position $z = 0$.

To determine the velocity of a particle which moves with the surface we evaluate the rate of change of ζ with respect to a fixed coordinate system

$$\frac{dz}{dt} = w(\zeta) = \frac{d\zeta}{dt} = (\partial_t \zeta + u\partial_x \zeta + v\partial_y \zeta)_{z=\zeta}. \tag{7.11}$$

At fixed coordinates x and y the surface (and particles on it) move up and down with velocity $\partial_t \zeta$. An important variable characterizing a surface deformation is vector normal to the surface. From differential geometry the unit vector $\mathbf{n}$ normal to the surface defined in Eq. (7.10) is

$$\mathbf{n} = \frac{1}{\sqrt{(\partial_x \zeta)^2 + (\partial_y \zeta)^2 + 1}}(-\partial_x \zeta, -\partial_y \zeta, 1). \tag{7.12}$$

We can now formulate the boundary conditions for velocities, electric fields and stresses at the interface between two dielectric viscous fluids. We will recall the notation and

discussion at the end of Chap. 5. At $z = \zeta$ we have,

$$\text{velocity BCs :} \qquad \| u \| = \| v \| = \| w \| = 0, \tag{7.13a}$$

$$w_1 = w_2 = \frac{d\zeta}{dt}, \tag{7.13b}$$

$$\text{electric fields BCs :} \qquad \mathbf{n} \times \| \mathbf{E} \| = 0, \tag{7.13c}$$

$$\mathbf{n} \cdot \| \mathbf{D} \| = \mathbf{n} \cdot \| \epsilon \mathbf{E} \| = 0, \tag{7.13d}$$

$$\text{stress BCs :} \qquad \| -p \| \, n_i + \| \tau_{ik} + T^M_{ik} \| \, n_k = \sigma \nabla_s^2 \zeta \, n_i, \tag{7.13e}$$

where ∇_s^2 is two-dimensional (surface) Laplacian expressing the surface curvature for small deformations.

The interface is characterized by a surface tension introduced through Young-Laplace equation. There is an abrupt change (jump) in liquid properties at $z = \zeta$. Formally, the surface tension is represented by a delta-function and the above boundary conditions obtained by integration of the bulk Eqs. (7.2) - (7.5) across the interface, Chandrasekhar, [49].

Eq. (7.13a) expresses the continuity of the velocities while Eq. (7.13b) follows from Eq. (7.11). The boundary conditions on the electric fields are Eqs. (5.43) and (5.44) with the surface charge density q_s equal to zero (no free charge present). Eq. (7.13e) represents the balance of the surface stresses. Pressure and surface tension contribute only to normal stresses while viscous and Maxwell stress tensors contribute also to tangential stresses.

7.2 Perturbation equations and boundary conditions

The procedure outlined in Sec. 6.2 will now be used to linearize equations of motion, Eqs. (7.2) - (7.5), and the boundary conditions Eqs. (7.6a) and (7.6b), Eqs. (7.7a) and (7.7b), and Eqs. (7.13a) - (7.13e).

7.2.1 The stationary solution for still liquids

We are considering the situation depicted in Fig. 7.2, i.e. two immiscible still liquids on top of each other with an electric field present. The vector $\mathbf{n}$ normal to the unperturbed interface is given by

$$\mathbf{n}_0 = (0, 0, 1), \tag{7.14}$$

while the stationary solutions in each region $i = 1, 2$ are

$$p_0^{(i)} = -\rho^{(i)} g x + P_0^{(i)}, \tag{7.15}$$

$$\mathbf{u}_0^{(i)} = 0, \tag{7.16}$$

$$\begin{Bmatrix} \mathbf{E}_0^{\mathrm{N}} \\ \mathbf{E}_0^{\mathrm{T}} \end{Bmatrix} = \begin{Bmatrix} (0, 0, E_{z0}^{(i)}) \\ (E_{x0}^{(i)}, 0, 0) \end{Bmatrix}. \tag{7.17}$$

$\mathbf{E}_0^{\mathrm{V}}$ and $\mathbf{E}_0^{\mathrm{H}}$ are the unperturbed vertical and horizontal fields shown in the two cases in Fig. 7.2, respectively. The curly brackets will be used throughout the chapter to represent the quantities corresponding to the two cases: the upper value always representing a quantity in the case of imposed vertical field (i.e. normal to the unperturbed interface) and the lower value always representing a quantity in the case of imposed horizontal field (i.e. tangential to the unperturbed interface).

As expected, the equilibrium pressure is the hydrostatic pressure resulting after the integration of Eq. (7.2). In motionless liquids there are only normal contributions to the stress, coming from pressure and electric fields. We can use results for electric stress obtained for a plane interface in Chap. 5. The stress balance at the interface is

$$\| P_0 \| \, n_{0x} = \| P_0 \| \, n_{0y} = 0, \tag{7.18a}$$

$$\| P_0 \| \, n_{0z} = \left\{ \begin{array}{c} \frac{1}{2} \| \epsilon E_{z0}^2 \| \\ -\frac{1}{2} \| \epsilon \| \, E_{x0}^2 \end{array} \right\}, \tag{7.18b}$$

where we have used the fact that in the case of imposed horizontal field, $\mathbf{E}_{x0}$ is the same in the two dielectrics.

7.2.2 Linearization of the perturbed equations

A slight disturbance of the interface corresponds to a small perturbation of the stationary solutions. Expanding the perturbed fields u, p and ϕ we get

$$\mathbf{u} = \mathbf{u}_0 + \mathbf{u}' + \dots, \tag{7.19a}$$

$$p = p_0 + p' + \dots, \tag{7.19b}$$

$$\phi = \phi_0 + \phi' + \dots, \tag{7.19c}$$

where we kept only linear terms in the increments $\mathbf{u}'$, p' and ϕ'. Putting the perturbed variables into the equations of motion, Eqs. (7.2) and (7.3), and subtracting the stationary solutions we get the equations for the perturbations:

$$\rho \partial_t \mathbf{u}' = -\boldsymbol{\nabla} p' + \mu \boldsymbol{\nabla}^2 \mathbf{u}', \tag{7.20}$$

$$\boldsymbol{\nabla} \cdot \mathbf{u}' = 0, \tag{7.21}$$

$$\nabla^2 \phi' = 0, \tag{7.22}$$

where $\mathbf{u}' = (u', v', w')$. By applying $\boldsymbol{\nabla}\cdot$ to Eq. (7.20) and using Eq. (7.21) we see that p' satisfies the Laplace equation

$$\nabla^2 p' = 0. \tag{7.23}$$

To get the equations for electric fields we apply ∂_x to Eq. (7.22),

$$\nabla^2 E_x' = 0. \tag{7.24}$$

The other components of $\mathbf{E}^{'}$ are determined from

$$\boldsymbol{\nabla}\times\mathbf{E}^{'} = 0, \tag{7.25}$$

which is a consequence of Eq. (7.5).

As can be noticed we have not considered the changes in the density or viscosity since in each region they are assumed constant.

7.2.3 Linearization of the perturbed boundary conditions

Rigid boundaries

At the rigid boundaries the normal vector is $\mathbf{n}_0$ from Eq. (7.14). When perturbed variables from Eqs. (7.19a) - (7.19c) are put into the boundary conditions, we get for the velocity perturbations

$$w' = u' = v' = 0 \qquad (z = a, -b), \tag{7.26}$$

and for the **E**-field perturbations

$$\left\{\begin{matrix} \mathbf{n}_0\times\mathbf{E}^{'} = 0 & (z = a, -b) \\ \mathbf{n}_0\cdot\mathbf{E}^{'} = 0 & (z = \pm\infty) \end{matrix}\right\}, \tag{7.27}$$

where in the case of imposed tangential field we evaluate the perturbations at the infinity, in accordance with Eqs. (7.8) and (7.9).

The perturbed interface

Linearization of the interface BCs is a more complicated procedure. The perturbed values given by Eqs. (7.19a) - (7.19c) have to be evaluated, strictly speaking, at $z = \zeta$. However, since ζ is assumed small, for the first order approximation it will suffice to consider the conditions at $z = 0$. For example, the approximation

$$E'_y(\zeta) = E'_y(0) + \partial_z E'_y(0)\zeta + ... \approx E'_y(0), \tag{7.28}$$

is valid if both E'_y and ζ remain small. In addition, the normal vector is now

$$\mathbf{n} = \mathbf{n}_0 + \mathbf{n}^{'}, \tag{7.29a}$$

where $\mathbf{n}^{'}$ is according to linearized Eq. (7.12)

$$\mathbf{n}^{'} = (-\partial_x\zeta, -\partial_y\zeta, 0). \tag{7.29b}$$

With the above remarks in mind the linearized BCs at the interface, $z = 0$, come as follows. The conditions on the velocities, Eqs. (7.13a) and (7.13b), become

$$\| u' \| = \| v' \| = \| w' \| = 0, \tag{7.30a}$$

$$w_1(0) = w_2(0) = \partial_t\zeta. \tag{7.30b}$$

The perturbed electric fields for the normal and tangential case in each of the regions are

$$\left\{\begin{matrix} \mathbf{E}^{\mathrm{N}} \\ \mathbf{E}^{\mathrm{T}} \end{matrix}\right\} = \left\{\begin{matrix} (E'_x, E'_y, E_{z0} + E'_z) \\ (E_{x0} + E'_x, E'_y, E'_z) \end{matrix}\right\}, \tag{7.31}$$

which together with Eqs. (7.29a) and (7.29b) yields

$$\left\{\begin{array}{rl} \| E_x' + E_{z0}\partial_x\zeta \| & = 0 \\ \| E_x' \| & = 0 \end{array}\right\}, \tag{7.32a}$$

$$\left\{\begin{array}{rl} \| \epsilon E_z' \| & = 0 \\ \| -\epsilon E_{x0}\partial_x\zeta + \epsilon E_z' \| & = 0 \end{array}\right\}, \tag{7.32b}$$

instead of Eqs. (7.13c) and (7.13d), respectively.

Linearized stresses

The perturbed stress condition is given by Eq. (7.13e). Expanding the pressure according to Eq. (7.19b), with p_0 defined in Eq. (7.15), we arrive at

$$-\| p' \| n_i - \| P_0 \| n_i + \| \rho \| g\zeta n_i + \| \tau_{ik} + T_{ik}^M \| n_k = \sigma\nabla_s^2\zeta n_i, \tag{7.33}$$

where, of course, $\mathbf{n}$ is given by Eq. (7.29a) and therefore has components in all three directions. A useful thing is now to consider the stress components from the above equation separately.

We have mentioned earlier that the variables at the interface $z = \zeta$ will be approximated with the values at $z = 0$. However, in the above term $\| \rho \| g\zeta$ we cannot immediately put $\zeta = 0$ since the time derivative of the displacement ζ equals the vertical velocity w, Eq. (7.30b). In other words, to account for the gravity effects, the above equation would first need to be differentiated with respect to time, after which we can put $\zeta = 0$. In terms of the components, both the gravity and the surface tension term have only z components up to the first order.

We saw in Eq. (7.18b) that $\| P_0 \| n_i$ has only the z component in the stationary case. It will however have the first-order components in x and y directions after the interface is perturbed

$$\| P_0 \| n_x = \left\{\begin{array}{r} \frac{1}{2}\| \epsilon E_{z0}^2 \| \\ -\frac{1}{2}\| \epsilon \| E_{x0}^2 \end{array}\right\} (-\partial_x\zeta), \tag{7.34a}$$

$$\| P_0 \| n_y = \left\{\begin{array}{r} \frac{1}{2}\| \epsilon E_{z0}^2 \| \\ -\frac{1}{2}\| \epsilon \| E_{x0}^2 \end{array}\right\} (-\partial_y\zeta), \tag{7.34b}$$

$$\| P_0 \| n_z = \left\{\begin{array}{r} \frac{1}{2}\| \epsilon E_{z0}^2 \| \\ -\frac{1}{2}\| \epsilon \| E_{x0}^2 \end{array}\right\}. \tag{7.34c}$$

Comparing the above equations with the Eqs. (7.18a) and (7.18b) we see that after the stationary solution is subtracted from the perturbed pressure, the only contributions that are left from the pressure P_0 will be in x and y direction! It is crucial to realize the importance of the P_0 contribution, if the stress balance is to match consistently.

Since the stationary velocity $\mathbf{u}_0$ is zero, the perturbed velocity $\mathbf{u}$ from Eq. (7.19a) is just u'. The perturbed viscous stresses reduce to the stresses for perturbations

$$\tau_{ik} = \tau_{ik}' = \mu(\partial_k u_i' + \partial_i u_k'). \tag{7.35}$$

We now wish to linearize the components of the stress in the three directions. Up to the first order we have

$$\tau_{xk}n_k = \mu(\partial_z u' + \partial_x w'), \tag{7.36a}$$
$$\tau_{yk}n_k = \mu\left(\partial_z v' + \partial_y w'\right), \tag{7.36b}$$
$$\tau_{zk}n_k = 2\mu\partial_z w', \tag{7.36c}$$

in x, y and z direction, respectively.

In similar way the perturbed components of the Maxwell stress tensor are

$$T^M_{ik} = -\frac{\epsilon}{2}E^2 n_i + E_i D_k n_k. \tag{7.37}$$

In this case the stationary stresses have non-zero values, Eqs. (7.18b) and (7.18a). After the linearization of Eq. (7.37) the perturbation components are

$$T^{M'}_{xk}n_k = \begin{Bmatrix} \frac{1}{2}\epsilon E^2_{z0}\partial_x\zeta + \epsilon E_0 E'_x \\ -\frac{1}{2}\epsilon E^2_{x0}\partial_x\zeta + \epsilon E_0 E'_z \end{Bmatrix}, \tag{7.38a}$$

$$T^{M'}_{yk}n_k = \begin{Bmatrix} \frac{1}{2}\epsilon E^2_{z0}\partial_y\zeta + \epsilon E_0 E'_y \\ \frac{1}{2}\epsilon E^2_{x0}\partial_y\zeta \end{Bmatrix}, \tag{7.38b}$$

$$T^{M'}_{zk}n_k = \begin{Bmatrix} \epsilon E_{z0}E'_z \\ -\epsilon E_{x0}E'_x \end{Bmatrix}. \tag{7.38c}$$

All of the above stresses are to be evaluated at $z = 0$.

Grouping the above perturbation stress components together, we have in x, y and z direction, respectively,

$$\begin{Bmatrix} \| \epsilon E^2_{z0} \| \\ -\| \epsilon \| E^2_{x0} \end{Bmatrix} (\partial_x\zeta) + \| \mu\left(\partial_z u' + \partial_x w'\right) \| + \begin{Bmatrix} \| \epsilon E_{z0}E'_x \| \\ \| \epsilon E_{x0}E'_z \| \end{Bmatrix} = 0, \tag{7.39a}$$

$$\begin{Bmatrix} \| \epsilon E^2_{z0} \| \\ 0 \end{Bmatrix} (\partial_y\zeta) + \| \mu\left(\partial_z v' + \partial_y w'\right) \| + \begin{Bmatrix} \| \epsilon E_{z0}E'_y \| \\ 0 \end{Bmatrix} = 0, \tag{7.39b}$$

$$-\| p' \| + \| 2\mu\partial_z w' \| + \begin{Bmatrix} \| \epsilon E_{z0}E'_z \| \\ \| -\epsilon E_{x0}E'_x \| \end{Bmatrix} + (\| \rho \| g - \sigma\nabla^2_s)\zeta = 0. \tag{7.39c}$$

7.2.4 Expansion into normal modes

We will now expand the perturbations into the normal modes, assuming the two liquids are confined between two infinite planes having the normal in z direction (see Chap. 6):

$$\zeta = \hat{\zeta}\exp[i(k_x x + k_y y) - i\omega t], \tag{7.40a}$$

$$\mathbf{u}' = \hat{\mathbf{u}}(z)\exp[i(k_x x + k_y y) - i\omega t], \tag{7.40b}$$

$$p' = \hat{p}(z)\exp[i(k_x x + k_y y) - i\omega t], \tag{7.40c}$$

$$E'_x = \hat{E}_x(z)\exp[i(k_x x + k_y y) - i\omega t]. \tag{7.40d}$$

The above solutions are put into the governing Eqs. (7.2) and (7.3)

$$-i\omega\rho\hat{u} = -ik_x\hat{p} + \mu(-k^2 + \partial_z^2)\hat{u}, \tag{7.41a}$$

$$-i\omega\rho\hat{v} = -ik_y\hat{p} + \mu(-k^2 + \partial_z^2)\hat{v}, \tag{7.41b}$$

$$-i\omega\rho\hat{w} = -\partial_z\hat{p} + \mu(-k^2 + \partial_z^2)\hat{w}, \tag{7.41c}$$

$$ik_x\hat{u} + ik_y\hat{v} + \partial_z\hat{w} = 0, \tag{7.41d}$$

and into the stress boundary conditions Eqs. (7.39a) - (7.39c)

$$\begin{Bmatrix} \|\,\epsilon E_{z0}^2\,\| \\ -\|\,\epsilon\,\|\,E_{x0}^2 \end{Bmatrix}(ik_x\hat{\zeta}) + \|\,\mu\,(\partial_z\hat{u} + ik_x\hat{w})\,\| + \begin{Bmatrix} \|\,\epsilon E_{z0}\hat{E}_x\,\| \\ \|\,\epsilon E_{x0}\hat{E}_z\,\| \end{Bmatrix} = 0, \tag{7.41e}$$

$$\begin{Bmatrix} \|\,\epsilon E_{z0}^2\,\| \\ 0 \end{Bmatrix}(ik_y\hat{\zeta}) + \|\,\mu\,(\partial_z\hat{v} + ik_y\hat{w})\,\| + \begin{Bmatrix} \|\,\epsilon E_{z0}\hat{E}_y\,\| \\ 0 \end{Bmatrix} = 0, \tag{7.41f}$$

$$-\|\,\hat{p}\,\| + \|\,2\mu\partial_z\hat{w}\,\| + \begin{Bmatrix} \|\,\epsilon E_{z0}\hat{E}_z\,\| \\ \|\,-\epsilon E_{x0}\hat{E}_x\,\| \end{Bmatrix} + (\|\,\rho\,\|\,g + \sigma k^2)\hat{\zeta} = 0, \tag{7.41g}$$

where $k = \sqrt{k_x^2 + k_y^2}$. Note that the above equations do not have the time dependence. In addition, from Eqs. (7.40c) and (7.23) we get

$$-k^2\hat{p} + \partial_z^2\hat{p} = 0. \tag{7.42}$$

Let us now obtain the form of solutions. Eqs. (7.40c) and (7.42) give for pressure $\hat{p}$

$$\hat{p}(z) = \exp(\pm kz), \tag{7.43}$$

which together with Eq. (7.41c) gives for $\hat{w}$

$$\hat{w} = \exp\pm(kz) \text{ and } \exp\pm(qz), \tag{7.44}$$

where $q = \sqrt{k^2 - \frac{i\omega}{\nu}}$. In case of inviscid liquids the terms with q vanish. Finally, Eqs. (7.24) and (7.25) give for $\hat{\mathbf{E}}$

$$\hat{E}_x = \exp(\pm kz), \tag{7.45a}$$

$$\hat{E}_y = \frac{k_y}{k_x} E_x, \tag{7.45b}$$

$$\hat{E}_z = \frac{1}{ik_x} \partial_z E_x. \tag{7.45c}$$

Elimination of $\hat{u}$, $\hat{v}$, $\hat{p}$
We will now simplify Eqs. (7.41a) - (7.41g) by eliminating dependence on $\hat{u}$, $\hat{v}$ and $\hat{p}$.

From Eq. (7.41d) the conditions imposed on $\hat{u}$ and $\hat{v}$ can be expressed by conditions imposed on $\partial_z \hat{w}$, since $\mathbf{k}$ is a continuous variable. The no-slip conditions at rigid boundaries, Eqs. (**??**) and (**??**), and the continuity of velocities at the interface, Eq. (7.30a), now become

$$\hat{w} = 0 = \partial_z \hat{w} \qquad (z = a, -b), \tag{7.46a}$$

$$\| \hat{w} \| = 0 = \| \partial_z \hat{w} \| \qquad (z = 0). \tag{7.46b}$$

Multiplying Eqs. (7.41c) and (7.41g) by k^2 and ∂_z, respectively, adding them and making use of Eq. (7.41d) we get for the stress in z direction

$$\| [i\omega\rho + \mu(\partial_z^2 - 3k^2)] \partial_z \hat{w} \| - k^2 \left[(\| \rho \| \, g + \sigma k^2) \hat{\zeta} + \begin{Bmatrix} \| \epsilon E_{z0} \hat{E}_z \| \\ \| -\epsilon E_{x0} \hat{E}_x \| \end{Bmatrix} \right] = 0. \tag{7.47}$$

Finally, we multiply Eqs. (7.41e) and (7.41f) by ik_x and ik_y, respectively, and add them together. Using Eqs. (7.41d) and (7.22) we arrive at

$$- \| \mu(k^2 + \partial_z^2) \hat{w} \| + \begin{Bmatrix} \| -\epsilon E_{z0}^2 k^2 \hat{\zeta} - \epsilon E_{z0} \partial_z \hat{E}_z \| \\ \| \epsilon E_{x0}^2 k_x^2 \hat{\zeta} + ik_x \epsilon E_{x0} \hat{E}_z \| \end{Bmatrix} = 0, \tag{7.48}$$

which comprises the continuity of x and y stresses across the interface.

7.2.5 Summary of solutions and linearized boundary conditions

For the sake of easier reading we will now finally summarize relevant solutions and all of the linearized boundary conditions.

Solutions
velocities:

$$\hat{w}_1 = A_1 \exp(kz) + A_2 \exp(-kz) + A_3 \exp(qz) + A_4 \exp(-qz), \tag{7.49a}$$

$$\hat{w}_2 = B_1 \exp(kz) + B_2 \exp(-kz) + B_3 \exp(qz) + B_4 \exp(-qz), \tag{7.49b}$$

E fields:

$$\hat{E}_{x1} = C_1 \exp(kz) + C_2 \exp(-kz), \tag{7.49c}$$

$$\hat{E}_{z1} = \frac{k}{ik_x} \left[C_1 \exp(kz) - C_2 \exp(-kz) \right], \tag{7.49d}$$

$$\hat{E}_{x2} = D_1 \exp(kz) + D_2 \exp(-kz), \tag{7.49e}$$

$$\hat{E}_{z2} = \frac{k}{ik_x} \left[D_1 \exp(kz) - D_2 \exp(-kz) \right]. \tag{7.49f}$$

BCs at rigid boundaries
velocities:

$$\hat{w}_1(a) \quad = 0 = \partial_z \hat{w}_1(a), \tag{7.50a}$$

$$\hat{w}_2(-b) = 0 = \partial_z \hat{w}_2(-b), \tag{7.50b}$$

E fields:

$$\left\{ \begin{matrix} \hat{E}_{x1}(a) = \hat{E}_{y1}(a) = 0 \\ \hat{E}_{z1}(\infty) = 0 \end{matrix} \right\}, \tag{7.50c}$$

$$\left\{ \begin{matrix} \hat{E}_{x2}(-b) = \hat{E}_{y2}(-b) = 0 \\ \hat{E}_{z2}(-\infty) = 0 \end{matrix} \right\}. \tag{7.50d}$$

BCs at interface z=0
velocities:

$$\| \hat{w}(0) \| = 0 = \| \partial_z \hat{w}(0) \|, \tag{7.50e}$$

surface displacement:

$$\hat{\zeta} = i \frac{\hat{w}_1(0)}{\omega}, \tag{7.50f}$$

E and **D** fields:

$$\left\{ \begin{matrix} \| ik^2 E_{z0} \frac{\hat{w}_1(0)}{\omega} + \partial_z \hat{E}_z(0) \| = 0 \\ \| \hat{E}_x(0) \| = 0 \end{matrix} \right\}, \tag{7.50g}$$

$$\left\{ \begin{matrix} \| \epsilon \hat{E}_z(0) \| = 0 \\ \| k_x \epsilon E_{x0} \frac{\hat{w}_1(0)}{\omega} + \epsilon \hat{E}_z(0) \| = 0 \end{matrix} \right\}, \tag{7.50h}$$

(7.50i)

stresses:

$$\| [i\omega\rho + \mu(\partial_z^2 - 3k^2)]\partial_z \hat{w}(0) \| - k^2 \left[i(\| \rho \| \, g + \sigma k^2) \frac{\hat{w}_1(0)}{\omega} + \begin{Bmatrix} \| \epsilon E_{z0} \hat{E}_z(0) \| \\ \| -\epsilon E_{x0} \hat{E}_x(0) \| \end{Bmatrix} \right] = 0, \tag{7.50j}$$

$$- \| \mu(k^2 + \partial_z^2)\hat{w}(0) \| + \begin{Bmatrix} \| -i\epsilon E_{z0}^2 k^2 \frac{\hat{w}_1(0)}{\omega} - \epsilon E_{z0} \partial_z \hat{E}_z(0) \| \\ \| \, i\epsilon E_{x0}^2 k_x^2 \frac{\hat{w}_1(0)}{\omega} + i k_x \epsilon E_{x0} \hat{E}_z(0) \| \end{Bmatrix} = 0. \tag{7.50k}$$

Chapter 8

Interfaces in electrohydrodynamics: applications in microfluidics

Having summarized the solutions and the boundary conditions we can now start solving some special cases. It is important to say that many aspects of the electrohydrodynamic instability of two-inviscid-dielectric systems have already been discussed, [42]. The equations Eqs. (7.49a) - (7.50k) include the viscous effects and for zero viscosity recover the results stated in [42].

We will consider three types of regimes in our analysis: re-derived macro regime considered in [42], as a reference point for comparison, with no micro length-scales involved; microfluidic-plane regime with only one micro dimension L_0 (the case of two infinitely long planes spaced by L_0); and microfluidic-channel regime, with two or even three micro dimensions involved - L_0, L_x and L_y - being the height, length and width of a channel, respectively. The analysis will provide reasonable estimates with respect to the onset of instability in case of two-liquid viscous pump previously considered.

All numerical calculations will include the oil-water system from Table 8.1. Notation will follow Chap. 7.

We will treat only the case which is stable when $\mathbf{E} = 0$. This means that oil will be always upper liquid 1 of thickness a, and water the lower liquid 2 with thickness b.

8.1 Zero viscosity and perpendicular E-field

In the inviscid case the viscous stresses are neglected. The **E**-field is perpendicular to the interface and therefore the upper values in the curly brackets in Chap. 7 need to be

	ρ kg/m^3	ϵ_r	λ_c S/m	σ J/m^2
corn oil	920	3.1	5×10^{-11}	–
water, distilled	1000	80.1	2×10^{-4}	–
copper	–	∞	5.8×10^{7}	–
oil-water interface	–	–	–	18×10^{-3}

Table 8.1: Parameters for the oil-water system. ρ is mass density, ϵ_r is the relative dielectric constant, λ_c is the conductivity, and σ is the surface tension, [45].

considered. From Eqs. (7.50a) - (7.50d) velocities and fields are of the form

$$\hat{w}^{(1)} = A \sinh k(z-a), \tag{8.1a}$$

$$\hat{w}^{(2)} = B \sinh k(z+b), \tag{8.1b}$$

$$\hat{E}_x^{(1)} = C \sinh k(z-a), \tag{8.1c}$$

$$\hat{E}_x^{(2)} = D \sinh k(z+b). \tag{8.1d}$$

The four constants A, B, C and D can be determined from the interface BCs, Eqs. (7.50e) - (7.50j), which reduce to

$$\| \hat{w}(0) \| = 0, \tag{8.2a}$$

$$\| k^2 E_{z0} \frac{\hat{w}^{(1)}(0)}{n} + D\hat{E}_z(0) \| = 0, \tag{8.2b}$$

$$\| \epsilon \hat{E}_z(0) \| = 0, \tag{8.2c}$$

$$\| -\rho n D \hat{w}(0) \| - k^2 \left[(\| \rho \| \, g + \sigma k^2) \frac{\hat{w}^{(1)}(0)}{n} + \| \epsilon E_{z0} \hat{E}_z(0) \| \right] = 0. \tag{8.2d}$$

8.1.1 Dispersion relation $\omega(\mathbf{k})$: general case

Inserting the solutions Eqs. (8.1a) - (8.1d) into Eqs. (8.2a) - (8.2d) defines an eigenvalue problem from which we can determine the eigenfrequency. From the condition that the determinant of the system vanishes we obtain

$$\omega^2 = k^2 \left[\frac{(\rho^{(2)} - \rho^{(1)})}{\rho} \frac{g}{k} + \frac{\sigma k}{\rho} - \frac{1}{\rho} \frac{(\epsilon^{(2)} - \epsilon^{(1)})^2}{\epsilon^{(1)} \tanh(kb) + \epsilon^{(2)} \tanh(ka)} E_{z0}^{(1)} E_{z0}^{(2)} \right], \tag{8.3}$$

where $\rho = \rho^{(1)} \coth(ka) + \rho^{(2)} \coth(kb)$. As a reminder, the electrostriction effect does not appear in the above equation since we included it into the pressure term, see Sec. 5.2.

Eq. (8.3) can be cast into the non-dimensional form by introducing the following set of variables marked with a prime

$$\begin{aligned} a' &= \tfrac{a}{L_0}, & \rho'^{(i)} &= \tfrac{\rho^{(i)}}{\rho_0}, \\ b' &= \tfrac{b}{L_0}, & E'^{(i)} &= \tfrac{E_{z0}^{(i)} L_0}{V_0}, \\ k' &= kL_0, & \omega' &= \omega\sqrt{\tfrac{\rho_0 L_0^3}{\sigma}}, \end{aligned} \tag{8.4}$$

which lead to

$$\omega'^2 = \frac{k'}{\rho'}\left(k'^2 - \varepsilon'(k')W_{el}k' + Bo\right) = \frac{k'}{\rho'}Y(k'). \tag{8.5}$$

In Eq. (8.5) we have

$$\rho' = \rho'^{(1)}\coth(k'a') + \rho'^{(2)}\coth(k'b'), \tag{8.6a}$$

$$\varepsilon'(k') = \frac{(\epsilon_r^{(2)} - \epsilon_r^{(1)})^2 E'^{(1)} E'^{(2)}}{\epsilon_r^{(1)}\tanh(k'b') + \epsilon_r^{(2)}\tanh(k'a')}, \tag{8.6b}$$

with the non-dimensional (measures of) electric fields

$$E'^{(1)} = -\frac{\epsilon_r^{(2)}}{\epsilon_r^{(1)}b' + \epsilon_r^{(2)}a'}, \tag{8.7a}$$

$$E'^{(2)} = -\frac{\epsilon_r^{(1)}}{\epsilon_r^{(1)}b' + \epsilon_r^{(2)}a'}. \tag{8.7b}$$

The two characteristic non-dimensional numbers which appear are

$$We_{\,\mathrm{el}} = \frac{\epsilon_0 E_0^2 L_0}{\sigma} = \frac{\epsilon_0 V_0^2}{\sigma L_0}, \tag{8.8a}$$

$$Bo = \frac{(\rho^{(2)} - \rho^{(1)})gL_0^2}{\sigma}. \tag{8.8b}$$

The "electrical" Weber number[1] $We_{\,\mathrm{el}}$ and the BOnd number Bo represent the ratio between the corresponding energy density, electric and gravitational respectively, and the surface energy density. For a typical voltage $V_0 = 1\,\mathrm{kV}$ and a length $L_0 = 100\,\mu\mathrm{m}$, we find for the oil-water system $We_{\,\mathrm{el}} \sim 5$ and $Bo \sim 4 \times 10^{-4}$. The effect of gravity can be completely ignored in microfluidics. For the (capillary) length $L_0 = 4.8\,\mathrm{mm}$ the Bond number $Bo = 1$.

It is worth to highlight four main aspects of Eq. (8.3).

[1]The electrical Weber number is obtained from the ordinary Weber number by substituting the kinetic energy density $\frac{1}{2}\rho v^2$ with the electric energy density $\frac{1}{2}\epsilon_0\epsilon_r E^2$. The dependence on ϵ_r we have included in Eqs. (8.7a) and (8.7b).

1. The dimension of each of the terms in brackets is $[(l/t)^2]$. Each of the factors represents the square of the corresponding phase velocity for the gravity waves, V_g^2, the surface-tension or capillary waves, V_c^2, and the electrohydrodynamic (EHD) waves, V_e^2, respectively. If the field is zero we have only the gravity and the capillary waves, the situation described in Chap. 6. A non-zero normal **E**-field produces stresses which result in the third term in Eq. (8.3). There will be a contribution only if two fluids with different dielectric constants are present.

2. For a given wave vector **k** the **E**-field can be made large enough so that its phase velocity contribution, V_e^2, prevails over those of gravity and capillary waves. Conversely, for a given field strength (before the instability sets in), there is always a **k** value for which either gravity or capillary waves prevail. The effects of electric fields on long or short waves, therefore, cannot be considered without the inclusion of gravity or capillary forces in one of the two important limits, $\mathbf{k} \to 0$ and $\mathbf{k} \to \infty$.

   The phase velocities for $Bo = 39$ are shown in Fig. 8.1 (a). The increase in voltage increases V_e^2; at $V = 5.83\,\mathrm{kV}$, V_e^2 is just slightly smaller than $(V_g^2 + V_c^2)$, meaning that the frequency ω is just slightly positive, see Fig. 8.1 (c). For $Bo = 4 \times 10^{-5}$, both V_g^2 and V_e^2 are constant for the k-range shown in Fig. 8.1 (b). If the voltage is increased in small steps from the value $V = 0.1\,\mathrm{V}$, there will come a point when the two phase velocities exactly cancel each other. This happens when

$$V^2 = \frac{\epsilon_r^{(1)} b + \epsilon_r^{(2)} a}{(\epsilon_r^{(1)} - \epsilon_r^{(2)})^2\, \epsilon_r^{(1)} \epsilon_r^{(2)} \epsilon_0} (\rho^{(2)} - \rho^{(1)}) g \tag{8.9}$$

$$\approx \frac{a^3}{\epsilon_r^{(1)} \epsilon_0} (\rho^{(2)} - \rho^{(1)}) g, \tag{8.10}$$

   where the approximation holds if $\epsilon_r^{(2)} \gg \epsilon_r^{(1)}$, and yields $V = 0.17\,\mathrm{V}$.

3. Each of the three terms in the brackets, V_g^2, V_c^2 and V_e^2, have dependence on the wave vector **k** i.e. the waves are dispersive. We have just seen in Fig. 8.1 (b) that for $ka, kb \ll 1$ (and small Bo values), the gravity and the EHD waves both become dispersionless. But also, the EHD waves become dispersionless in the short-wavelength limit when $ka, kb \gg 1$. This effect can be seen in Fig. 8.1 (a) or directly from Eq. (8.3). An important conclusion is that in the limits when a phase velocity becomes constant, the minimum of the total phase velocity does not depend on that particular contribution. Furthermore, the wave vector $k_{\min}$ for which the total phase velocity is both *minimal* and *zero* also does not depend on the constant phase-velocity contributions.

4. The point when instability sets in is when the total phase velocity, and therefore ω, becomes zero. If the **E**-field is not present there can only be the gravitational instability if a heavier liquid is on top of a lighter one, Sec. 6.3. However, Eq. (8.3) shows that the normal field always *destabilizes* the interface by reducing the phase velocity; this happens even in the absence of the ordinary gravitational instability.

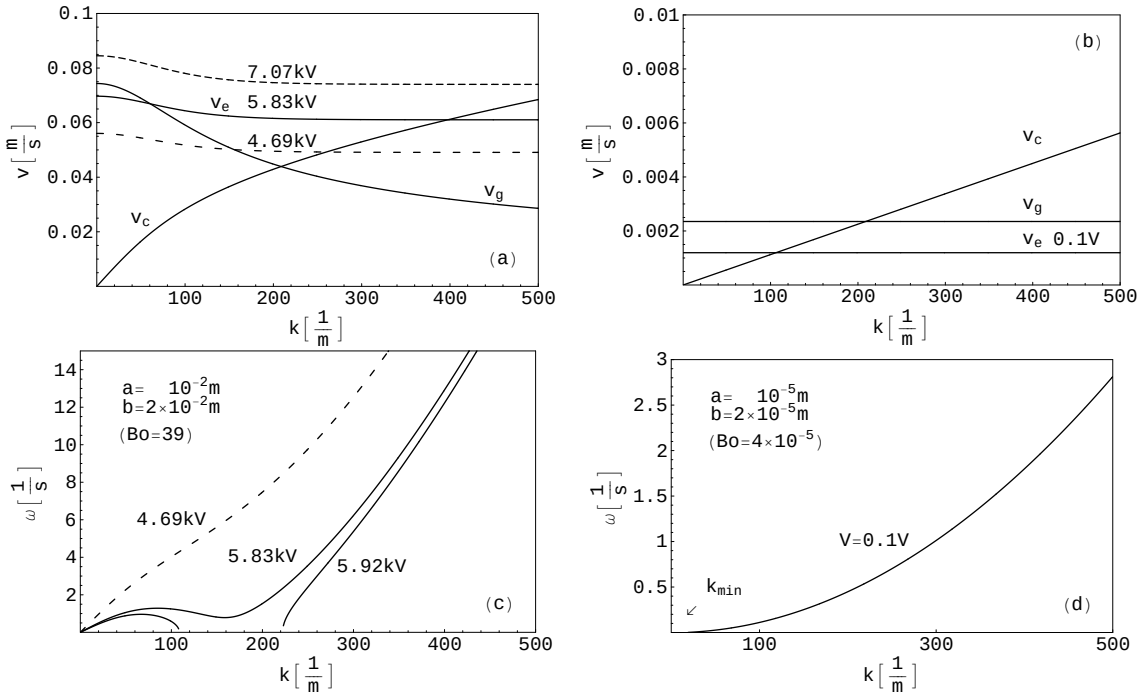

Figure 8.1: Phase velocities and eigenfrequencies as function of wave number for the two-lquid oil-water system with parameters given in Table 8.1 and layer thickness denoted a and b, respectively. (a) Phase velocities for large $Bo = 39$ corresponding to the limit $ka, kb \gg 1$. The velocity V_e is dispersionless for large k. For $V = 5.83\,\mathrm{kV}$, $V_e^2 < V_g^2 + V_c^2$ just before the instability sets in, see panel (c). (b) Phase velocities for microfluidic $Bo = 4 \times 10^{-5}$ corresponding to the limit $ka, kb \ll 1$. Both V_e and V_g are dispersionless. Instability starts for $V = 0.17\,\mathrm{V}$ when $V_e = V_g$. (c) The frequency ω for $Bo = 39$. For $V = 5.92\,\mathrm{V}$ there is a range of k-values yielding instability. Note the region of negative group velocity $d\omega/dk$. (d) The frequency ω for $Bo = 4 \times 10^{-5}$. The instability sets in at $k = 0$, a characteristic of microfluidic systems.

If the **E**-field is increased beyond the onset of instability, the frequency becomes negative for a range of k values. In Fig. 8.1 (c) this happens for $V = 5.92\,\mathrm{V}$. Comparing Fig. 8.1 (c) with Fig. 8.1 (d) we notice that in the case of very small Bond number the position of the $k_{\min}$ is shifted towards very long wavelengths (smaller k's). This is one of the characteristics of the microfluidic regime - instability starts from the limit $k = 0$. This, of course, is to be expected since the surface tension, which is the dominant force, has negligible effect on the long wavelengths.

8.1.2 The onset of instability: limiting cases for infinite planes

We will now quantify the conditions for the onset of instability by considering Eq. (8.5). To observe the change in the sign of the frequency ω' it is sufficient to consider the behavior

of $Y(k')$

$$Y(k') = k'^2 - \varepsilon'(k')\, We_{\rm el}\; k' + Bo. \tag{8.11}$$

If there is no **E**-field, $We_{\rm el} = 0$ and $Y(k')$ becomes a parabola displaced vertically by Bo, Fig. 8.2 (a). $Y(k')$ acquires the negative values only if $Bo < 0$. The instability is present for the k' values smaller than $k'_c = \sqrt{-Bo}$ which is just the critical wave number for the Rayleigh-Taylor instability, Eq. (6.19).

The effect of the field is described by the EHD term $-\varepsilon'(k')\, We_{\rm el}\; k'$ which acquires different values in the two limits of short and long wavelengths. If $a'/b' \sim 1$, we have

$$\varepsilon'(k') = \begin{cases} \frac{\epsilon_r^{(1)}}{a'^2}\varepsilon_\infty^{\rm corr} & k'a', k'b' \gg 1, \\ \frac{1}{k'}\frac{\epsilon_r^{(1)}}{a'^3}\varepsilon_0^{\rm corr} & k'a', k'b' \ll 1. \end{cases} \tag{8.12}$$

The factors $\varepsilon_\infty^{\rm corr}$ and $\varepsilon_0^{\rm corr}$ are functions of $\epsilon_r^{(1)}/\epsilon_r^{(2)}$ and b'/a', and they are close to 1 for $\epsilon_r^{(1)}/\epsilon_r^{(2)} \ll 1$. When the thickness-ratio a'/b' differs significantly from 1 we need to evaluate Eq. (8.5) numerically.

Using Eq. (8.12) we can easily determine the function $Y(k')$ in the limits:

$$Y(k') = \begin{cases} k'^2 - \alpha_\infty k' + Bo & k'a', k'b' \gg 1, \\ k'^2 - \alpha_0 + Bo & k'a', k'b' \ll 1, \end{cases} \tag{8.13}$$

where $\alpha = \alpha(We_{\rm el})$ is independent of k'. The two parabolas will have the extremum (minimum) at the point

$$T(k'_{\rm min})) = \begin{cases} \left(\frac{\alpha_\infty}{2}, Bo - \frac{\alpha_\infty^2}{4}\right) & k'a', k'b' \gg 1, \\ (0,0) & k'a', k'b' \ll 1. \end{cases} \tag{8.14}$$

The onset of instability happens when $Y(k'_{\rm min})$ in Eq. (8.13) first becomes zero, i.e.

$$\begin{aligned} \alpha_\infty &= 2\sqrt{Bo} && k'a', k'b' \gg 1, \\ \alpha_0 &= Bo && k'a', k'b' \ll 1. \end{aligned} \tag{8.15}$$

In terms of $We_{\rm el}$ Eqs. (8.14) and (8.15) give

$$k'_{\rm min} = \sqrt{Bo}, \quad We_{\rm el} = \frac{2\sqrt{Bo}}{\varepsilon'_\infty} \qquad k'a, k'b \gg 1, \tag{8.16}$$

$$k'_{\rm min} = 0, \qquad We_{\rm el} = \frac{Bo}{\varepsilon'_0} \qquad k'a, k'b \ll 1, \tag{8.17}$$

where ε'_0 and ε'_∞ are constants given in Eq. (8.12).

In Fig. 8.2 (b), $Y(k')$ is plotted for a large Bond number, $Bo = 25$, and different values of $We_{\rm el}$. Eq. (8.16) predicts $k'_{\rm min} = 5$ for $We_{\rm el} = 0.97$. The actual $k'_{\rm min} = 4.535$ is obtained numerically, see Fig. 8.3 (a). Further increase in $We_{\rm el}$ leads to negative $Y(k')$ values.

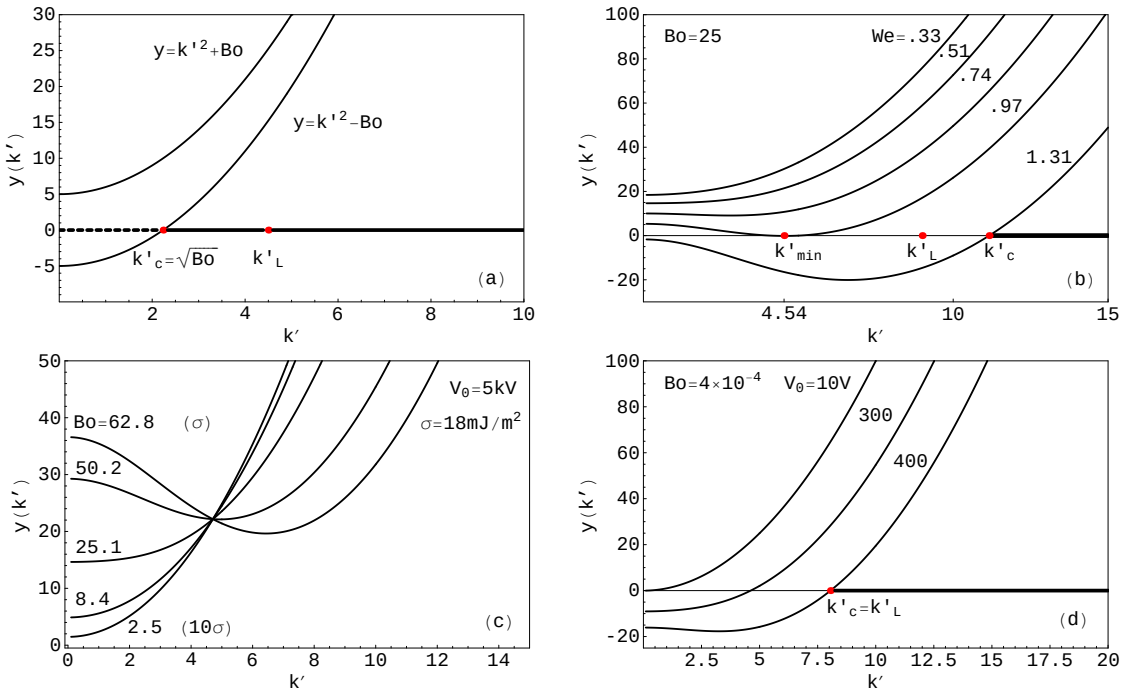

Figure 8.2: Dependence of $Y(k')$ on $We_{\rm el}$ and Bo. (a) Without **E**-field present, instability is possible when the heavier liquid is on top of the lighter one (negative Bo). The unstable wave numbers are $k' < k'_c = \sqrt{Bo}$ (dashed region). If a finite-size system is characterized by a k'_L, the system will be stable as long as $k'_L > k'_c$ (bold region). (b) For a large Bond number the onset of instability happens at $k'_{\rm min} \sim \sqrt{Bo}$. Further increase in the voltage causes a range of unstable k'-s. For $We_{\rm el} = 1.31$, the k'_L shown is within the unstable region. (c) Shifting of $k'_{\rm min}$ towards zero as the Bond number is lowered, Eq. (8.17). To make the effect more apparent, the surface tension has been varied (not the length scale) at a constant voltage. (d) The effect of the voltage increase in microfluidic regime. Instability starts at longer wavelengths. In order to reach the size-dependent k'_L, the applied voltage has to be increased substantially .

Small Bond numbers correspond to the the large values of surface tension. If the Bond number is lowered the minimum is shifting towards smaller k'-values. As mentioned earlier, in terms of $Y(k')$ this is shown in Fig. 8.2 (c)[2]. The larger surface tension stabilizes small wavelengths pushing the instability to the longer ones. We can apply Eq. (8.17) which shows that the instability begins at $k'_{\min} = 0$ when the Bond number exactly cancels the electric term. This corresponds to the cancellation of the V_e and V_g phase velocities in this limit as already discussed earlier. If the Bond number is lowered beyond that point, the electric term will prevail over Bo and there will be a range of k'-values for which $Y(k')$ is negative.

So if we have a small Bond number to begin with, as in microfluidic systems, raising the voltage from zero to the value giving $\varepsilon'_0 We_{\rm el}$, the instability is first induced at the infinitely long wavelength; raising the voltage further, more and more of the longer wavelengths become unstable - a situation completely analogous to the negative Bond number (heavier liquid on top of the lighter one) without **E**-field, as shown in Fig. 8.2 (d) and (a).

We have seen in Chap. 6 that finite size microfluidic systems impose constraints on the possible wavelengths. In order to generate the instability, the voltage will need to be raised so that the unstable wave numbers fall in the range below the critical k_c. We will return to this important point later where the finite-size effects in microfluidics are considered in detail.

8.1.3 The onset of instability: general case for infinite planes

We will now numerically determine the value $k'_{\min}$ for which the instability first occurs. The wave number satisfies the requirements

$$Y(k'_{\min}) = 0, \tag{8.18a}$$

$$\frac{dY(k'_{\min})}{dk'} = 0; \qquad \frac{d^2Y(k'_{\min})}{dk'^2} < 0. \tag{8.18b}$$

As an illustration consider two boundaries equally spaced from the interface, i.e. $a' = b' = 0.5$, then Eq. (8.11) can be written in the form

$$Y(k') = k'^2 - \alpha k' \coth(0.5k') + Bo, \tag{8.19a}$$

where $\alpha = \alpha_0/2$ and $\alpha = \alpha_\infty$ in the respective limits. Applying the conditions Eqs. (8.18a) and (8.18b) on Eq. (8.19a) yields

$$\alpha = \frac{k'^2_{min} + Bo}{k'_{\min} \coth(0.5\, k'_{\min})}, \tag{8.19b}$$

$$\sinh(k'_{\min}) \left(k'^2_{min} - Bo\right) + k'_{\min} \left(k'^2_{min} + Bo\right) = 0, \tag{8.19c}$$

which in the limits of short and long wavelengths, $k'a' \gg 1$ and $k'a' \ll 1$, recover Eq. (8.15).

[2]To emphasize the effect the voltage is kept constant and the Bond number was lowered by increasing the surface tension.

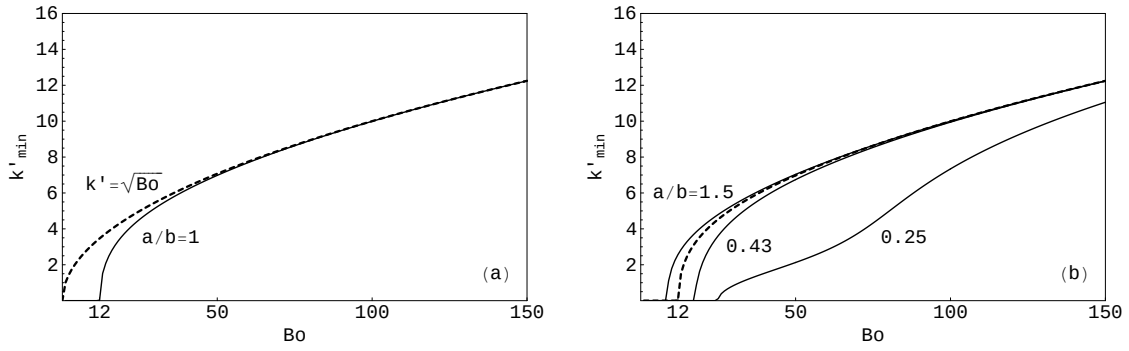

Figure 8.3: Wave number $k'_{\min}$ of marginal stability as function of Bo, Eq. (8.19a). Stable and unstable wave numbers cannot be directly deduced. (a) Equal layer thicknesses, $a = b$. For $Bo < 12$ the onset of instability starts at $k' = 0$ (b) Unequal layer thicknesses, $a \neq b$. The case $a = b$ shown as a dashed line. Due to the stronger field thin-oil configurations are less stable, see the discussion in the text.

The dependence of $k'_{\min}$ on Bo obtained from Eqs. (8.19b) and (8.19c) is shown in Fig. 8.3 (a). The solid curve approaches $\sqrt{Bo}$ (zero) for large (small) Bo as it should. The numerical analysis shows that at a particular finite value of the Bond number, $Bo = 12$, the Bond number exactly cancels the EHD term, and the onset of instability is shifted to $k' = 0$. To emphasize this point we write:

$$\text{for } \frac{a}{b} = 1 \text{ and } Bo = 12 \quad \Rightarrow \quad -\varepsilon'(k')\, We_{\rm el}\, k' = Bo \quad \Rightarrow \quad Y(k') = k'^2. \tag{8.20}$$

The graph in Fig. 8.3 (a) (solid line) represents the wave numbers of the states with marginal stability, and yet it does not divide stable from unstable k'-values.

It is important to note that the stable and unstable k'-values cannot be deduced directly from Fig. 8.3 (a). For example, for $Bo > 12$, the onset of instability happens at a $k'_{\min}$ (a value on the solid line) while the values of k' both above and below $k'_{\min}$ are stable (analogous to the k' values left and right from $k'_{\min}$ in Fig. 8.2 (b) for $We_{\rm el} = 0.97$). Unstable wave numbers exist after the voltage is raised further, and need to be found by solving the condition $Y(k') < 0$, where $Y(k')$ is given by Eq. (8.11). In case of $Bo < 12$, unstable wave numbers are present when the EHD term exceeds the Bond number, similar to Fig. 8.2 (b) for $V =$ 300 or 400 V.

The governing factor in the EHD term from Eq. (8.11) is the **E**-field inside the dielectric with smaller ϵ_r. In Fig. 8.3 (b), the dependence of $k'_{\min}$ on Bo is shown for four different layer-thickness ratios. If the oil layer is thicker than the water layer, $a/b = 1.5$, the **E**-field within the oil layer is smaller compared to the case of equal thicknesses $a/b = 1$ [3]. This yields a smaller EHD term - a smaller Bond number is required to cancel the EHD contribution. If the oil layer is slightly thinner than the water layer, the Bond number needed to cancel now larger EHD term is larger. The graphs will be shifted left or right, respectively, from the case $a/b = 1$.

[3] Keeping the voltage constant.

To see (qualitatively) which of the two configurations (represented by the curves left or right from the $a/b = 1$ curve) is more stable, we now apply a voltage to bring the thicker-oil ("left") configuration to the onset of instability for e.g. $Bo = 12$. The same voltage will produce a range of unstable wave numbers for the thinner-oil ("right") configurations, since in this case the EHD contribution in Eq. (8.11) prevails over the Bond number $Bo = 12$, making $Y(k') < 0$. The discussion will be illuminated further when the instability voltages are found.

8.1.4 Instability voltages for infinite planes, $kL \gg 1$ (macrofluidic limit)

The limits $ka, kb \gg 1$ correspond to the cases where the wavelength is much shorter than the distances a and b between the interface and the boundaries. In other words, there is a small interaction between the short-wavelength disturbances at the interface and the electrodes. In this limit surface tension is the dominant force.

Large values of the Bond number correspond to the small values of surface tension (or large distance between the electrodes). As the Bond number is increased we expect that stability border is shifted further towards larger k'-s, i.e. smaller wavelengths, where the stabilizing effect of the surface tension is still significant (or where the more pronounced gravity effect did not yet take over). This is revealed in Eq. (8.16).

From Eq. (8.16) we further observe that the wavelength $\lambda_{min} = 2\pi/k_{\min}$ at which the instability sets in is the same as in the ordinary gravitational instability i.e. given by the Rayleigh-Taylor condition, Eq. (6.20). This is a consequence of the fact that V_e^2 is dispersionless in this limit, as already mentioned earlier, see Fig. 8.1 (a). From Eq. (8.16) we also obtain the voltage at the onset of instability:

$$V_0 = L_0 \left[\frac{4\sigma(\rho^{(2)} - \rho^{(1)})}{\epsilon_0^2 \varepsilon_\infty'^2} \right]^{\frac{1}{4}}. \tag{8.21}$$

Since microfluidics is characterized with extremely low Bond numbers this voltage is irrelevant for microfluidic regime. For the sake of comparison we evaluate the above voltage for the symmetric, oil-water system: for $L_0 = 2a = 2\,\text{cm}$, $V_0 = 5.76\,\text{kV}$.

In [43], a set of the instability experiments was performed in a large apparatus in the regime of $Bo \sim 25$. The dimensions were confined basically in one direction by electrodes whose distance ($\sim$ cm) could be adjusted to remove the boundaries from the interface. The instability in the short-wavelength limit could then be well tested; both λ_{min} given by Eq. (6.20) and the linear dependence on L_0 in Eq. (8.21) were confirmed.

8.1.5 Instability voltages for infinite planes, $kL \ll 1$, (microfluidic limit)

We now turn to the limit relevant for microfluidics. When $ka, kb \ll 1$, the wavelengths are much longer than the boundary distances and there will be a strong interaction between the waves and the electrodes.

We can investigate this limit by lowering the characteristic distance $L_0 = a + b$ which corresponds to the regime of small Bond numbers. We have seen in Fig. 8.3 that for small

Bond numbers instability is shifted towards longer wavelengths (since destabilizing effects of gravity become less and less pronounced).

When $a' = b'$, Fig. 8.3 (a) shows that for $Bo = 12$ ($L_0 = 1.66\,\mathrm{cm}$), instability starts at the infinitely long wavelength. For the oil-water system this happens when $V_0 = 4.45\,\mathrm{kV}$. We wish to find the condition on the voltage causing the onset of instability for any Bond number smaller than 12. For all these Bond numbers we are in the limit where the results of Eq. (8.17) hold, and so the voltage condition is obtained by equalizing the EHD term with the given Bond number. The result is Eq. (8.9), or slightly rewritten

$$V_0 = L_0^{\frac{3}{2}} \sqrt{\frac{(\rho^{(2)} - \rho^{(1)})g}{\epsilon_0 \varepsilon_0'}}. \tag{8.22}$$

For $Bo = 4 \times 10^{-4}$ ($L_0 \sim 100\,\mu\mathrm{m}$), Eq. (8.22) gives the voltage on the order of 2 V.

Inducing the instability in microfluidic systems with a small voltage can be used to enhance the mixing of fluids. Although the above analysis is based on still, perfectly insulating (immiscible) liquids, the order of magnitude cannot be far off. An active micromachined mixer applying the electrical fields has already been realized in literature, [53]. The electrodes were arranged so that a normal field could act on the surface of two conducting, streaming fluids. The characteristic distance was $L_0 = 200\,\mu\mathrm{m}$. At a flow rate of $10\,\mu\mathrm{l/min}$, two liquids, one with a low and the other one with much higher conductivity, were fully mixed with a low voltage of 7 V (over a distance of $500\,\mu\mathrm{m}$).

The instability experiments in microfluidic regime have not yet been performed systematically. To illustrate how could the instability manifest itself for dielectric liquids we quote Melcher, [42], who performed the experiments with rounded electrodes down to $a = 0.4\,\mathrm{cm}$: "For close plate-interface spacings, the surface remains rounded until the interface arcs over to the electrode."

8.1.6 Finite-size effect on instability in microfluidics

So far we have been concerned with the instability between two infinitely long plates. But microfluidic systems, or actually the channels, are always finite in size, usually long and narrow, and behave more like resonators, Fig. 8.4. We have seen already, Sec. 6.3, that the finite size will impose restriction on the possible wavelengths and therefore on the instability requirements.

In some microfluidic systems, such as micro cell-sorters, liquid streams are parallel to each other, and gravity does not play any role. The Bond number does not enter the equations. However, the shape of the interface between such immiscible streams (in a closed microchannel) will be curved due to the strong capillary forces, Fig. 8.4 (b). The same reasoning goes if a gas bubble is stuck inside a channel in which an **E**-field is present. The meniscus will be especially pronounced in the smaller dimensions. The assumption of a field normal to the interface in such case will therefore not be a valid one, to say at least. Also, small parasitic capillary waves will develop on the surface of the meniscus.

A more thorough analysis is needed to address these issues. For now, in order to get some estimates, we will proceed as though the field is normal to the interface and the

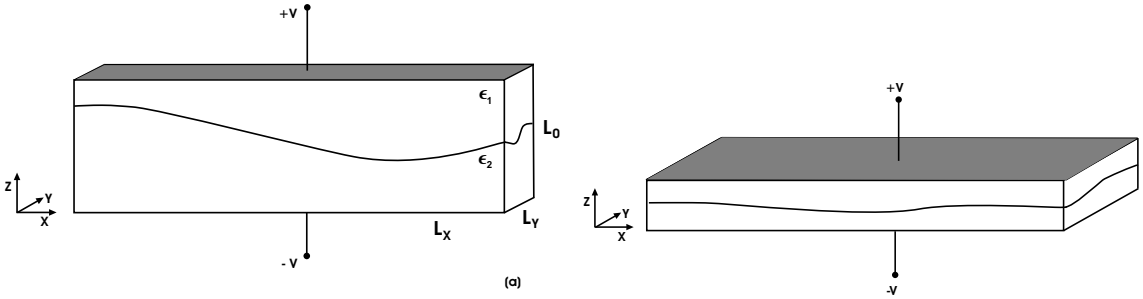

Figure 8.4: Two liquids in finite size microfluidic channels. The liquids will align themselves to minimize the surface free energy. (a) High aspect ratio microfluidic channel, $L_0 > L_y$. Capillary effects will be pronounced in the smaller dimension i.e. y direction. **E**-field produced by the electrode configuration is not normal to the meniscus shown. The voltages inducing instability in y direction are substantially larger, since the allowed smaller wavelengths are stabilized by surface tension. (b) Low aspect ratio microfluidic channel, $L_0 < L_y$. The two liquid configuration is similar to the two-infinite-planes case. However, the configuration shown is unstable due to increased interface area, and the liquids will spontaneously position themselves next to each other.

contact angle does not affect the unstable wavelengths. The latter approximation would be of some validity at least for the waves propagating in x direction, Fig. 8.4 (a).

Our analysis from Chap. 7 included the disturbances in both x and y-direction, but did not impose any restrictions on the wave numbers. To establish the conditions on k_x and k_y we consider the normal modes of Eqs. (7.40b) and (7.40c) in a rectangular cavity of length L_x, width L_y and height L_0.

Consider the perturbation pressure p' in the top [4] layer filling the cavity. The pressure satisfies the Laplace equation Eq. (7.23) with the solution given by Eq. (7.40c). Because of the inviscid approximation, the perpendicular velocities at each of the walls vanish; that is, u' and v' vanish at the boundaries $x = 0, L_x$ and $y = 0, L_y$, respectively, and w' vanish at $z = a$. By Eqs. (7.41a) - (7.41c) these conditions are equivalent to

$$\partial_x p' = 0 \quad (x = 0, L_x), \tag{8.23}$$

$$\partial_y p' = 0 \quad (y = 0, L_y), \tag{8.24}$$

$$\partial_z p' = 0 \quad (z = a). \tag{8.25}$$

We therefore choose the solution for p' in the form

$$p' = \cos x \cos y \cosh k(z - a). \tag{8.26}$$

Inserting the above solution into the Laplace equation Eq. (7.23) with the boundary conditions Eqs. (8.23) and (8.24) lead to the familiar relations

$$\begin{aligned} k_x &= \pm\tfrac{n\pi}{L_x}, \qquad n = 0, 1, 2, 3... \\ k_y &= \pm\tfrac{m\pi}{L_y}, \qquad m = 0, 1, 2, 3... \end{aligned} \tag{8.27}$$

[4] The layer with thickness a in z-direction.

The magnitude of the total wave number k is given by

$$k^2 = k_x^2 + k_y^2 = \pi^2 \left[\left(\frac{n}{L_x} \right)^2 + \left(\frac{m}{L_y} \right)^2 \right], \tag{8.28}$$

where integers n, m differ from zero at the same time. For any given mode defined by n and m, the wave numbers k_x and k_y, and therefore k are fixed. The dispersion relation for $\omega(\mathbf{k})$, Eq. (8.3), shows that for a given (n, m) mode ω^2 is linearly proportional to V_0^2.

8.1.7 Instability voltages in microfluidic channels

We will identify two different instability voltages for $L_x \gg L_0 > L_y$: V_{x0} and V_{y0} in the x and y directions, respectively.

The instability will occur when the voltage is raised so that the size dependent k_L falls in the range of unstable k-values, see Fig. 8.2 (b). For a given k_L from Eq. (8.28), the onset of instability starts when

$$Y(k_L') = k_L'^2 - \varepsilon'(k_L')\, We_{\,\mathrm{el}}\; k_L' + Bo = 0, \tag{8.29}$$

where $k_L' = k_L L_0$. Inserting $We_{\,\mathrm{el}}$ from Eq. (8.8a) into Eq. (8.29) we obtain for the impending voltage

$$V_0 = \sqrt{\frac{\sigma L_0 \left(k_L'^2 + Bo\right)}{\epsilon_0 \varepsilon'(k_L')\, k_L'}}. \tag{8.30}$$

To evaluate Eq. (8.30) in the long- and short-wavelength limits, we consider disturbances in a long and narrow rectangular microchannel with $L_x \gg L_0 > L_y$, Fig. 8.4 (a). As before, it is filled with an oil (liquid 1) of thickness a in the z-direction, and the water of thickness b.

The k-mode $(1, 0)$ represents the wave travelling down the channel in x-direction i.e. $k = k_x$. From Eqs. (8.4) and (8.27) we get the value of k' for which the onset of instability is reached

$$k_L' = \frac{\pi}{L_x} L_0. \tag{8.31}$$

To catch the essential features, we will assume that $a = b$ and $\epsilon_r^{(1)} \ll \epsilon_r^{(2)}$. For $k'a', k'b' \ll 1$, $\varepsilon'(k_L')$ is found from Eq. (8.12) to be

$$\varepsilon'(k_L') = \frac{1}{k_L'} \frac{\epsilon_r^{(1)}}{a'^3}, \tag{8.32}$$

which together with Eq. (8.30) gives

$$V_{x0} = a^{\frac{3}{2}} \sqrt{\frac{\sigma \pi^2}{\epsilon_r^{(1)} \epsilon_0\, L_x^2} + \frac{(\rho^{(2)} - \rho^{(1)}) g}{\epsilon_r^{(1)} \epsilon_0}}. \tag{8.33}$$

When $L_x \to \infty$, the above result goes into the familiar Eq. (8.9).

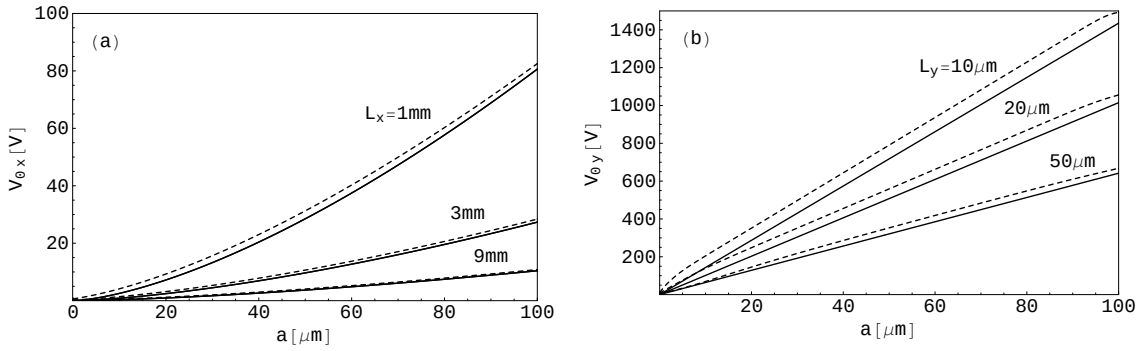

Figure 8.5: Instability voltages as function of the oil-thickness a. Instability is easier to induce in a longer dimension. The full solution, Eq. (8.30), is plotted with dashed line. (a) The voltage $V \sim a^{3/2}$ in the long-wavelength limit. (b) The voltage $V \sim a$ in the short wavelength limit.

The voltage dependence on the oil-thickness a is shown in Fig. 8.5 (a). For $L_x = 1\,\mathrm{mm}$ and $L_0 = 2a = 100\,\mu\mathrm{m}$, $V_{\mathrm{x0}} = 28.5\,\mathrm{V}$. This is two orders of magnitude higher than the pure Bond number contribution of 0.17 V for the instability when $L_x \to \infty$ (Eq. (8.9) or second term in Eq. (8.33)). We now see if $V_{x0} = 10\,\mathrm{V}$ is applied across $L_0 = 2a = 100\,\mu\mathrm{m}$, the instability of the $(1,0)$ mode will happen for $L_x > L_c = 2.9\,\mathrm{mm}$.

To find V_{y0} we proceed as follows. The $(0,1)$ mode represents a disturbance in y-direction. If the channels are such that $L_y < a$ we are in the limit $k'a', k'b' \gg 1$ and $\varepsilon' = \epsilon_r^{(1)}/a'^2$. We finally get

$$V_{y0} = a\sqrt{\frac{\sigma\pi}{\epsilon_r^{(1)}\epsilon_0 L_y}}, \tag{8.34}$$

where we have neglected the Bond number. For a choice, say $L_y = a = 50\,\mu\mathrm{m}$, Eq. (8.34) gives $V_{y0} = 321\,V$. Even smaller L_y lengths will lead to higher voltages. This conclusion, as well as the linear dependence of V_{y0} on a is shown in Fig. 8.5 (b). As expected, the disturbances in the smaller dimension are more stable (higher instability voltages needed) since the shorter wavelengths are stabilized by the surface tension.

When $\epsilon_r^{(1)} \ll \epsilon_r^{(2)}$ we have seen that the voltage primarily depends on the thickness a of the "weaker" dielectric 1 (the characteristic length in such systems is really a). Therefore, Eqs. (8.33) and (8.34) can be used to predict the voltages also in the asymmetric cases, $a \neq b$. To confirm that, the full voltage solution from Eq. (8.30) is plotted next to the approximate solutions in Fig. 8.5 (dashed line). If L_0 is held fixed, e.g. $100\,\mu\mathrm{m}$, the impending voltages for $0 < a < L_0$ can be read directly from the figure[5]. The graphs from Fig. 8.5 complement Fig. 8.3 (b).

One final remark about the voltages. Eq. (8.30) is an important result. In deriving it, we did not put any restrictions on the Bond number. Indeed, if k'_L in Eq. (8.30) is replaced

[5]The results obviously do not hold at $a = 0$ or $b = 0$ since this corresponds to one dielectric being present i.e. when the EHD term vanishes.

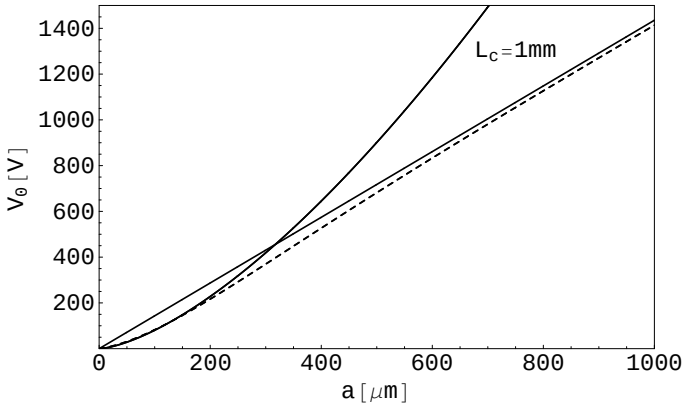

Figure 8.6: Instability voltage from Eq. (8.30) as function of the oil-thickness a. The length of the system (channel) is $L_c = 1$mm. The general expression (dashed line) goes into the limiting cases of Eqs. (8.33) and (8.34) for small and large a respectively.

by one of the limiting values, 0 or $\sqrt{Bo}$ from Eqs. (8.16) and (8.17), we recover the voltages for the onset of instability for large and small Bo, Eqs. (8.21) and (8.22), respectively. From Eq. (8.30) therefore, we can find the impending voltages for any Bond number and any finite size system having an arbitrary liquid-thickness ratios. To emphasize this, a graph is shown for a larger range of thicknesses a in a separate Fig. 8.6. As mentioned earlier, Eq. (8.30) does not account for the capillary (meniscus) effects.

8.1.8 Low aspect-ratio microchannels, $L_y \gg L_0$

For many applications, microfluidic channels are of small height-to-width aspect ratios, Fig. 8.4 (b). When two streams of liquid go into such a channel they will adjust to flow next to each other rather than on top of each other. By energy argument, surface will position itself to minimize the free energy; by instability argument, the smallest dimension allows (relatively) the most stable disturbances.

The question is whether the two liquids could at all be forced on top of each other, so that the meniscus effect is less pronounced. This could in fact be achieved in the two-liquid viscous pump described in Chap. 4. The conducting liquid introduced at the top (or bottom) is driven by EOF producing a sheet of width L_y as sketched in Fig. 8.7. By a connection to a reservoir with a non-conducting liquid, the non-conducting liquid could then be dragged by the boundary layer as explained before. Such system will be more prone to the instabilities not only in the x but also in the y direction. If there is a normal component of the **E**-field inside the non-conducting liquid, the voltage in Eq. (8.30) could then be used as an estimate for the impending instability in the x or y direction.

However, in the configuration of Fig. 8.7 the more significant contribution will be from the tangential component of the **E**-field,[6] and this is what we investigate next.

[6]On the boundary between two conductors with conductivities σ_1 and σ_2, the current normal to the boundary is conserved i.e. $\sigma_1 E_{1n} = \sigma_2 E_{2n}$. Therefore, on the interface between a conductor and a perfect

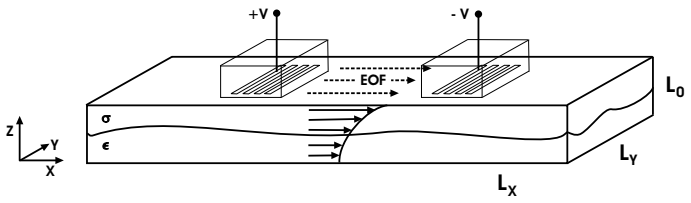

Figure 8.7: A modification of two viscous-liquid pump, Chap. 4, enabling two liquid layers to slide on top of each other in a low-aspect-ratio microfluidic channel. With $L_y \gg L_0$, the capillary effects at the boundaries in the y-direction are less pronounced, and the instability-voltage estimate from Eq. (8.30) can be applied.

8.2 Zero viscosity and parallel E-field

The influence of a parallel **E**-field on a two-dielectric system can be found by considering the lower values in the curly brackets of Eqs. (7.50a) - (7.50d). For a tangential **E**-field in the x-direction, we arrive at

$$\omega^2 = k^2 \left[V_g^2 + V_c^2 + \cos^2\theta V_e^2 \right], \tag{8.35}$$

where V_g and V_c are the gravitational and capillary phase velocity from Eq. (8.3), $\theta = k_x/k$ is the angle between the direction of the wave propagation and the **E**-field, while V_e^2 is now

$$V_e^2 = \frac{1}{\rho} \frac{(\epsilon_2 - \epsilon_1)^2}{\epsilon_1 + \epsilon_2} E_{x0}^2. \tag{8.36}$$

From Eq. (8.35) we see that the influence of a tangential **E**-field on the waves depends on the direction of the waves. The waves travelling perpendicular to the field, $\theta = 0$, are not affected by it; the waves travelling in the direction of the field, $\theta = 1$, will have the phase velocity *increased* by V_e^2. In addition, V_e is dispersionless due to the fact that boundaries where the field perturbations vanish are at infinity, see Eq. (7.27). A typical wave front for a radial disturbance will be an ellipsoid elongated in the direction of the **E**-field. Such wave fronts were confirmed experimentally in Ref. [43].

Because of the positive EHD term in Eq. (8.35) the frequency will not acquire any negative values (within the linear approximation). Unlike a normal **E**-field, a tangential field acts to enhance the interface stability.

With regard to the two-liquid viscous pump, the above analysis gives an idea that at least in a (fictitious) "stationary" pump-mode, instability of the waves travelling down the main channel will be suppressed. Instability of the waves propagating in the y-direction will not be influenced by the tangential field. However, for these waves $L_c = L_y \ll L_x$ and substantially larger normal fields are needed to induce the flow disruption.

A valid criticism of the above analysis is that the conductivities of the liquids (particularly water) were neglected. Such treatment is much more involved, especially in the case of an applied tangential field, as it has to properly account for the charge movement. It is planned for the future work.

---

dielectric, the normal **E**-field inside the conductor vanishes.

Chapter 9

Conclusion

The following report serves to highlight a variety of relevant topics in the field of microfluidics, from a theoretical and a simulation perspective. I hope that my investigations, in collaboration with my colleagues, helped to resolve some of the multidisciplinary "mysteries" behind lab-on-a-chip systems.

The thesis consists of essentially two parts. Chapters 1-4 give a general introduction to microfluidic systems and a brief description of microfluidic applications further developed in the research papers (Appendices A,B,C,D,E). In the second half, chapters 4-8, a detailed description of electrohydrodynamic (EHD) effects is presented with the accent on the instability between two immiscible dielectric liquids.

Chapter 1 is an outline of the manuscript. Chapter 2 underlines the important physics at work in microfluidic systems, and a section of it is adapted from my chapter published in a text-book (under references). Chapter 3 gives a thorough introduction to steady-state electroosmosis, an important phenomenon of driving liquids at the microscale. In chapter 4, the three different micro applications further analyzed in appendices A, C+D and E, are briefly reviewed.

Appendix A reports a study of the focusing effect of a chimney-like structure in a microchannel geometry, a system used in micro cell-sorters. Experimental PIV measurements are compared to the CFD simulations for a similar geometry, showing reasonable agreement. The small discrepancies are mainly due to numerical diffusion.

In Appendix B, an EOF micropump, recently built by Takamura et al., has been analyzed by means of equivalent electric and hydraulic circuits, backed by CFD simulations. The results of the combined theory/simulation technique are confronted to the experimental findings and suggest a need for stronger theoretical efforts in microfluidics.

Appendix C investigates a quasi-statical motion of a bubble in microfluidic axisymmetric contractions, based on the interplay between the surface energies and geometry. Capillary forces and partial-wetting concept were further used in a CFD simulation in Appendix D, where a passive bubble-trap is designed to ease the bubble removal from microchannels.

In Appendix E a preliminary study is presented on performance of patented two-liquid viscous pump. The pump uses a conducting liquid driven by the electroosmotic flow,

to drag a nonconducting liquid. A pressure/flow-rate characteristics are calculated using CFD and equivalent circuit theory.

The second part of the thesis starts with a general theoretical description of electric fields in dielectrics and how they couple to hydrodynamics. Next, a general discussion of hydrodynamic stability is presented.

The equations are then applied to study EHD instability of a flat interface between two perfect dielectric liquids in an electric field (perpendicular and parallel to it). The liquids are described by Stokes' equation with the electrical forces acting on the interface. The expansion of linearized perturbations into normal Fourier modes allows a description in terms of dispersion relations, which easily discriminate the unstable modes. The main generalization from the previous work lies in the inclusion of viscous terms, finite-size effects and the long-wavelength limit relevant for instabilities in microfluidics.

It was found that gravity is completely irrelevant in microsystems and that finite-size of microchannels can significantly suppress a number of unstable modes. In addition, normal electric fields always act to destabilize, while tangential fields act to stabilize the interface between two dielectrics (within linear stability approximation). Because of small dimensions of microfluidic systems, relatively small applied voltages ($\sim$ 10 V) can induce EHD instability and cause flow disruption.

Finally, all of my research details and more, including the thesis in PDF format, can be obtained from the group's web-page: $http://www.mic.dtu.dk/research/MIFTS$.

9.1 Outlook

The work in the immediate future will be focused on several topics that were not treated in the thesis. In brief, they are:

(1) Viscous streaming liquids.
The convective terms in Navier-Stokes equations will give first-order contributions in the linear stability analysis of two streaming viscous liquids. For parallel flows, the analysis involves solving of the Orr-Sommerfeld equation

$$\partial_z^4\psi - 2k^2\partial_z^2\psi + k^4\psi = ikRe\left[(U - \frac{\omega}{k})(\partial_z^2\psi - k^2\psi) - \partial_z^2 U\psi\right], \tag{9.1}$$

where $\psi(x,z)$ is the stream function and $U(z)$ the velocity of a primary flow. My attempt will be to find the solutions when electric fields are included. The work in this direction applied to the microfluidics will extend the existing literature, e.g. [54], and will give a definite answer on the stability of the two-liquid viscous pump.

(2) Finite conductivities.
We notice from Table 8.1 that the liquid conductivities, although small in comparison with metals, are finite i.e. the liquids are leaky dielectrics. As stated before, this will have an impact in balancing the shear stresses. Inclusion of the conductivities requires a proper treatment of the charge relaxation. In the case of a perpendicular field applied to a system where charges reside on the interface effectively all the time (short charge-relaxation times), the stress conditions Eqs. (7.50j) and (7.50k) can still be used if the

condition on **D**-field is modified to include the surface charge density, as in Eq. (5.44). The full treatment, however, involving the Nernst-Planck equation for charged species, is needed in the case of tangential fields acting on the streaming fluids. Such study will answer the problems of the so-called electrokinetic instability.

(3) Electrowetting effects.
The effects of a finite contact angle on the electric stresses need to be examined.

(4) Electrostriction term.
The electrostriction, Eq. (5.26), which has been put as a redefined pressure, plays a more important role in case of tangential fields, [43]. In combination with the Clausius-Mossotti dependence, Eq. (5.32), the contribution actually makes V_e^2 negative. However, in the experiments made by Melcher [43], large electrostriction causing negative phase velocity V_e^2 has not been observed. Whether such a conclusion is valid in microfluidics, remains an open question.

Appendix A

Paper published in J. Micromech. Microeng.

Title
PIV measurements in a microfluidic 3D-sheathing structure with three-dimensional flow behavior

Authors
Henning Klank, Goran Goranović, Jörg P. Kutter, Henrik Gjelstrup, Jess Michelsen, Carsten Westergaard

Reference
J. Micromech. Microeng. **12**, 862-869 (2002)

INSTITUTE OF PHYSICS PUBLISHING JOURNAL OF MICROMECHANICS AND MICROENGINEERING
J. Micromech. Microeng. **12** (2002) 862–869 PII: S0960-1317(02)37632-0

PIV measurements in a microfluidic 3D-sheathing structure with three-dimensional flow behaviour

H Klank[1], G Goranović[1], J P Kutter[1], H Gjelstrup[2], J Michelsen[2] and C H Westergaard[3]

[1] MIC-Mikroelektronik Centret, μTAS Project, Technical University of Denmark, 2800 Lyngby, Denmark
[2] Department of Mechanical Engineering, Fluid Mechanics Section, Technical University of Denmark, 2800 Lyngby, Denmark
[3] Dantec Dynamics A/S, Tonsbakken 16-18, 2740 Skovlunde, Denmark

E-mail: hk@mic.dtu.dk and carsten.westergaard@dantecdynamics.com

Received 31 May 2002, in final form 2 September 2002
Published 3 October 2002
Online at stacks.iop.org/JMM/12/862

Abstract
The design and production time for complex microfluidic systems is considerable, often up to several months. It is therefore important to be able to understand and predict the flow phenomena prior to design and fabrication of the microdevice in order to save costly fabrication resources. The structures are often of complex geometry and include strongly three-dimensional flow behaviour, which poses a challenge for the micro particle image velocimetry (micro-PIV) technique. The flow in a microfluidic 3D-sheathing structure has been measured throughout the volume using micro-PIV. In addition, a stereoscopic principle was applied to obtain all three velocity components, showing the feasibility of obtaining full volume mapping (x, y, z, U, V, W) from micro-PIV measurements. The results are compared with computational fluid dynamics (CFD) simulations.

(Some figures in this article are in colour only in the electronic version)

1. Introduction

Along with the requirements for more advanced liquid handling capabilities, the layout of microstructures becomes more and more complex. Computer modelling can accelerate and help in the labour intensive and time consuming process of intuitive design, fabrication and testing. However, in order to use simulations reliably as a design tool, the software used for modelling must initially be validated experimentally, e.g. with particle image velocimetry (PIV).

A microstructure that allows coaxial sheathing of a sample stream with a buffer stream was chosen as a demonstrator and is shown in figures 1 and 2. This so-called chimney structure is a crucial part of a micro cell sorter (Wolff *et al* 2000). The purpose of the cell sorter is to select cells according to specific biochemical and physical properties, e.g. whether they are leukaemia cells, or according to their size. For the cells to be recognized and selected, they have to be marked with fluorescent labels before they can be detected by the system. The detection system is typically organized like an epi-fluorescent microscope.

In a conventional cell sorter the sample fluid containing the labelled cells enters the sorter centrally in such a way that a buffer stream surrounds the sample. This sheathing of the sample ensures that cells are only travelling within the very narrow field of view of the detection system. Sheathing can only work under laminar flow conditions, which prevents the premature mixing of buffer and sample.

The type of sample sheathing as described above is difficult to achieve within micro cell sorters due to the two-dimensional, planar character of the fabricated devices. First-generation micro cell sorters therefore reverted to using two-dimensional sample sheathing. Such sample sheathing, however, has the disadvantage of signal and speed variations. Since the sample is neither sheathed on top nor sheathed on the bottom, cells can travel at any height within the fluidic

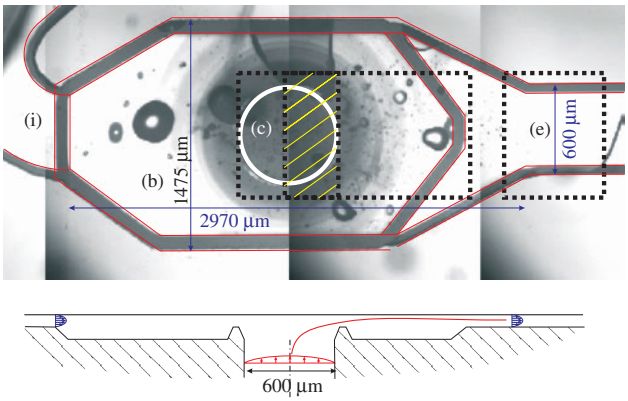

Figure 1. Overview of the chimney structure. The laminating buffer flow is entering the basin (b) from the left through the inlet (i), while the sample flow is entering the basin through the centre of the chimney (c). The total flow is leaving the basin over a step into the exit channel (e), where the lamination of the samples is completed. PIV measurements were performed in the outlined dashed areas. Stereoscopic PIV recombination was performed in an overlapping area from two camera positions over the chimney entrance, as indicated by shading.

channel of the micro cell sorter. Cells travelling outside the focal plane of the detection system will generate a lower signal than those travelling within the focal plane. Cells will also travel at different speeds due to the parabolic flow profile that develops in the channel. These speed differences diminish the accuracy of the cell sorter. To overcome these two disadvantages, second-generation micro cell sorters were developed that were able to sheath the sample three dimensionally, for example by Larsen (2000) and Tashiro *et al* (2000). The chimney structure, which has been developed at MIC (Larsen 2000) and is discussed in this paper, used only one input for the buffer to achieve coaxial sheathing of the sample. The chimney structure was described in more detail by Goranović *et al* (2001). It should be noted that the flow within a microfluidic system is always laminar under all practical conditions due to the extraordinary low Reynolds numbers. The above mentioned condition for a cell sorter that the sheathing flow should always be laminar is therefore fulfilled in all microfluidic cell sorters.

As shown in figures 1 and 2, the chimney structure consists of an inlet channel, the chimney itself, a basin and an exit channel. The sheathing buffer flow enters the basin through the inlet channel, where it merges with the sample flow entering through the chimney. The sheathing of the sample is gradually completed as the fluids exit through the outlet channel. The chimney basin was designed to take care of the laminating part of the buffer stream underneath the sample stream. At the end of the basin, the reduction in cross sectional area leads to an increase in flow velocity, which is especially high just at the basin corner. This layer of high-velocity buffer stream ensures sheathing at the bottom of the sample stream. Sheathing at the top of the sample stream is ensured as long as the buffer stream is fast enough to avoid being pushed backwards by the incoming sample stream.

Particle image velocimetry (PIV) has been applied in a number of microscopic devices with nozzle- or channel-like shapes, for instance by Meinhart *et al* (1999). In micro-PIV, where microscopes are used for imaging, all three important variables, spatial resolution, the equivalent of the light sheet thickness and field of view, are intertwined. The micro-PIV technique therefore has to balance these variables. Especially, the chimney structure provides additional challenges, since the structure is characterized by a complex geometry with a strongly three-dimensional flow.

The flow is visualized in figure 2 by introducing a tracer into the sample flow. The strongest out-of-plane movement is found near the outlet of the chimney and at the exit of the basin.

2. Experimental set-up

The chimney structure was fabricated in silicon by reactive ion etching. The top of the structure was closed with a glass cover, which was bonded directly to the silicon. The thickness of the cover glass was 0.75 mm. The fluid was purified water, which for the purpose of the PIV measurement was seeded with 1.0 μm 'orange fluorescent' polystyrene particles (Fluospheres, Molecular Probes). The excitation maximum of these particles was at around 540 nm, while the emission maximum was at around 560 nm. Sample and buffer were infused with one syringe pump (Pump 22, Harvard Apparatus) each. The flow rate for the sample flow through the chimney was kept constant at 0.02 ml min^{-1}, while the flow rate of the laminating flow was varied. Three flow cases were investigated giving a volume flow ratio of $R = 0.5$, 5 and 25, where R is the ratio of the laminating flow over the sample flow, also shown in table 1. The coordinates were placed with their origin in the centre of the chimney and the z-axis pointing out of the structure. The y-axis was positive in the main flow direction.

A Dantec HiSense camera with a 1280 by 1024 pixel array was used in conjunction with a NewWave Solo Nd:YAG

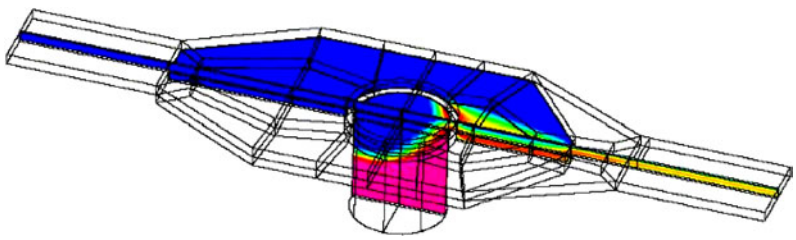

Figure 2. Outline of the chimney structure as modelled with the buffer fluid coming from the left. The shaded contours represent concentration of tracer fluid injected through the chimney illustrating how the buffer fluid laminates the sample fluid in the middle of the exit channel. The buffer to sample volume flow ratio was $R = 25$.

Table 1. Flow setting and key parameters for the cases investigated.

Flow ratio	Inlet flow (ml min^{-1})	Flow in chimney (ml min^{-1})	Flow in exit (total flow) (ml min^{-1})	Maximum velocity in exit (mm s^{-1})	Time between light pulses (μs)
$R = 0.5$	0.01	0.02	0.03	≈24	250
$R = 5$	0.1	0.02	0.12	≈90	60
$R = 25$	0.5	0.02	0.52	≈400	12

laser emitting at $\lambda = 532$ nm. The maximum energy used was 10 mJ. The light from the laser was delivered into the microscope illumination path with an optical fibre fitted to the microscope. The seeding was sufficiently efficient to apply an adaptive (multi-pass) PIV algorithm with 32 by 32 pixel interrogation areas. Only average velocities are presented in the paper. Ensemble correlation, as presented by Meinhart *et al* (1999), was also tested. Although the ensemble correlation is known to provide better results in a sparsely seeded flow, this technique did not provide additional information in our case, apparently because the flow was efficiently seeded.

The imaging was done using an epi-fluorescent microscope (DMLB, Leica) with a 20× /0.40 planachromatic objective and a 0.5× relay lens, resulting in a tenfold magnification and a field of view of 857 by 686 μm. Complementary measurements were also made with a 63 × /0.7 semi-apochromat objective. Both objectives were designed to have a relatively long working distance of up to 3.2 mm and 2.6 mm, respectively, which allowed practical room for the clamping of the holder of the chimney structure. The comparatively thick cover glass of 0.75 mm could be compensated for with adjustable optics integrated in both objectives.

Although oil-immersion objectives are beneficial to the light budget and to the quality of the imaging, these were not applicable in this case due to the fact that the working distances of the oil-immersion objectives were limited to a maximum of 0.22 mm.

With a magnification of 10, the 32 by 32 pixel interrogation area corresponded to 21 by 21 μm. This was a satisfactory size compared to the width of the channel. The focal depth of the microscope objective defines the thickness of the measurement plane. This was calculated to be 16 μm according to Meinhart (2000), which then gives a measurement volume of $21 \times 21 \times 16$ μm^3. Although the 16 μm present a relatively large fraction of the 60 μm channel depth, this was part of a practical trade-off.

The uncertainty of the measurement is estimated to be 0.45 mm s^{-1} for the flow case $R = 5$. The value is justified by observing the rms velocity of the U-velocity component of 50 vector maps in an area of the flow, which can be expected to be undisturbed by actual flow phenomena, i.e. in the vicinity of the walls in the exit channel, where disturbance from the shedding process is small. The value of 0.45 mm s^{-1} corresponds to an absolute uncertainty of 0.04 pixel displacement based on 50 samples. For one single measurement realization, this corresponds to 0.28 pixel ($0.04 \times \sqrt{50}$). This is slightly higher than ordinary PIV experiments, where a typical absolute uncertainty between 0.1 and 0.2 pixel displacement on a single measurement realization can be found. The uncertainty for the two other flow cases in table 1 is estimated to be 0.11 mm s^{-1} and 2.3 mm s^{-1} for the cases $R = 0.5$ and $R = 25$, respectively. The absolute accuracy of the measurement depends on a number of scaling factors, i.e. the optical magnification. A direct indication of the absolute accuracy is seen in table 2 by the fine agreement between the flow rates shown.

Table 2. Volume flow in the exit channel from PIV data and nominal volume flow of the syringe pumps. The PIV based volume flow was derived by integration of the velocities over the area of the exit channel.

Nominal flow rate (ml min^{-1})	Flow rate from PIV data (ml min^{-1})
0.030	0.028
0.12	0.12
0.52	0.48

The PIV measurements were done in two regions as outlined in figure 1. In the exit channel, the measurements were performed at five planes spaced 10 μm apart with the 857 by 686 μm field of view, as shown in figure 3. The first plane was estimated to be located approximately 10 μm below the glass surface, placing the volume that was mapped in the vertical centre of the channel. The 10 μm spacing provides a vertical overlap of 40%, given the focal depth of the microscope of 16 μm. Hence, the vertical overlap was similar to the overlap used for the in-plane PIV processing. Using the velocities from each measurement plane, velocities were extracted in the x–z-plane, as illustrated in figure 3.

The measurement area outlined in figure 1 in the central region around the chimney and upstream towards the step into the exit channel is composed of images originating from several camera positions. From each camera position, the field of view was 857 by 686 μm, resulting in a combined area of 857 by 1646 μm.

3. Stereoscopic micro-PIV measurements

A translation stage was used to map a larger area of the microstructure outlined in figure 1. The stage could also be used to obtain stereoscopic information from the flow in the same manner as cartographic information is gathered by flying over a terrain. In the shaded area of figure 1, two successive camera positions have significant overlap. The translation between these two positions was 320 μm or approximately half of the field of view. Inside the overlapping area, it was possible to perform stereoscopic recombination of the results, assuming the flow was stationary or more precisely that the average of several realizations was stationary. In this case, the flow measured at each camera position was an average of 50 samples, each sample recorded at statistical unrelated times.

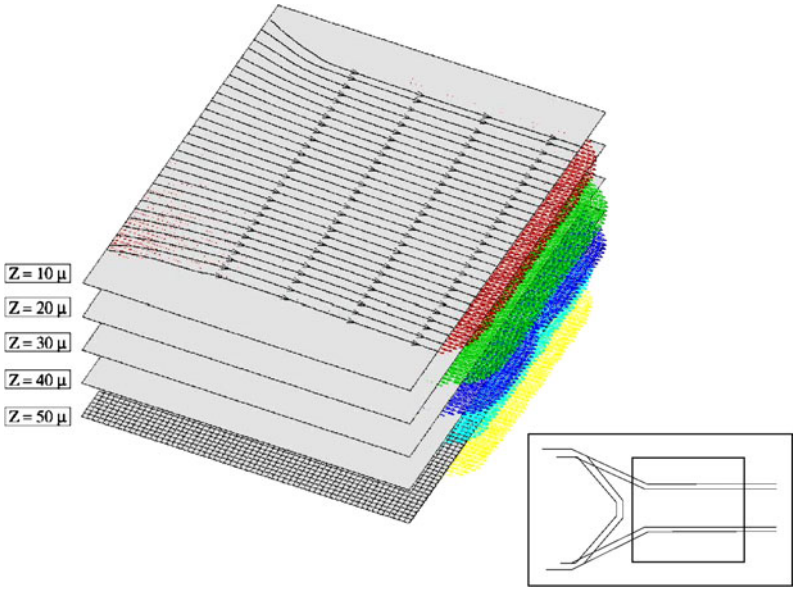

Figure 3. PIV measurements in the exit channel were performed in five x–y-planes spaced 10 μm in depth (z-direction). The measurement area is indicated in the inset. There were 63 by 79 vectors in each plane originating from an interrogation area of 21 by 21 μm. The thickness of the measurement plane was defined by the focal depth of the microscope objective to be 16 μm. Stream traces on the top plane indicate the end of the contraction and the beginning of the exit channel.

The most common technique used to compute stereoscopic PIV results is to pre-calibrate the two camera views with a known calibration target placed at different z-positions. From the calibration a transfer function is generated, which is often a direct linear transform. This approach would also have worked satisfactorily for this application, except for the obvious access problems, making it impossible to position a calibration target *in situ*. Alternatively, an analytical approach could be chosen as described by Prassad and Adrian (1993). The two main parameters are the translation between the camera positions and the optical path from the measurement plane to the principal plane of the optical imaging system. Although the translation was accurately known, the optical path was only known in coarse details.

Mapping the entire parameter set needed for the stereoscopic combination would have been a complicated task. It requires that refraction of light in the air/glass interface of the cover glass on the microstructure be taken into account. In particular, the orientation of the microstructure surface must be well known in order to determine the refraction of light in the cover glass. A scheme to map the various parameters failed in the measurement campaign presented here and therefore a more pragmatic approach was chosen. Ignoring the air/glass interface and pretending the set-up to appear in a medium with a uniform refractive index, the equations for recombination were significantly reduced. Ignoring the interface and cover glass (750 μm thick) seemed reasonable, since it was less than one-third of the optical path from the objective to the measurement plane. Further, the stereo view angle was less than 6° and the imaging was sharp all over the field of view of the camera. Prassad and Adrian (1993) present three equations for fluid displacement in air (equations (11)–(13)). Of these we work with the equation for the z-velocity component:

$$W = \frac{\Delta z}{\Delta t} = \frac{1}{\Delta t}\frac{-d_0(\Delta X_1 - \Delta X_2)}{M_0 S - (\Delta X_1 - \Delta X_2)} \qquad (1)$$

where Δz is the displacement, Δt is the time between the two laser pulses, S is the displacement between the two camera positions, d_0 is the object to lens distance, M_0 is the magnification and ΔX_1 and ΔX_2 are the displacements measured by the camera in the two view positions.

Observing that $M_0 S \gg (\Delta X_1 - \Delta X_2)$, equation (1) may be simplified to

$$W = \frac{d_0}{S}\frac{(\Delta X_2 - \Delta X_1)}{M_0 \Delta t} = \frac{d_0}{S}(U_2 - U_1). \qquad (2)$$

Hence the W-velocity component may be expressed as the difference between the velocities measured from each camera in the translation direction (x-direction) scaled with a factor (d_0/S). This means the W-component may always be visualized qualitatively, and additionally be quantitatively estimated, except for the scaling factor. For this case using a qualified guess, an absolute velocity magnitude was obtained. Compared to the result from computational fluid dynamics shown in figure 7, the factor was underestimated by at least 20%. The correction was included in the PIV plot shown in figure 7.

4. Simulations

Flow in the chimney structure was simulated using the commercial software package CFD-ACE+ 6.4 from CFD Research Corporation, Huntsville, AL, for computational fluid dynamics (CFD). This piece of software is a multi-physics package based on the finite-volume method. The program was run on an 800 MHz Pentium III processor with 512 MB of RAM. Although the experiments were carried out in the laminar flow regime, simulations were done on a fine mesh of about 100 000 cells to account for the complex geometry of the fabricated design. The geometry used in the simulations included some simplifications compared to the actual microstructure used for the experiments. The sidewalls

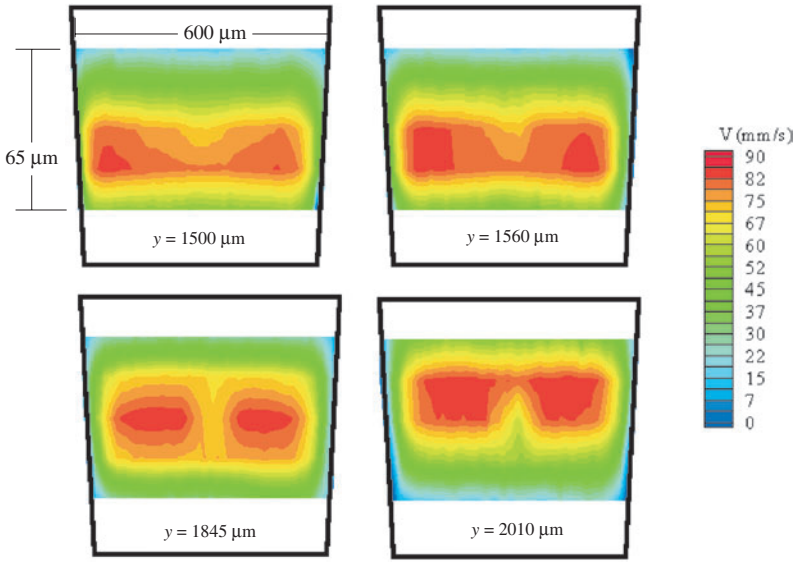

Figure 4. V-velocity component shown in x–z-planes. The data were extracted from the PIV results shown in figure 3 at four y locations. Note that channel height and width are scaled differently. Colour coding of V-component was the same in figures 4 and 6.

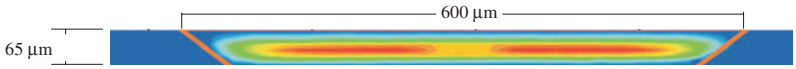

Figure 5. Realistic dimensions of the x–z-planes of figure 4.

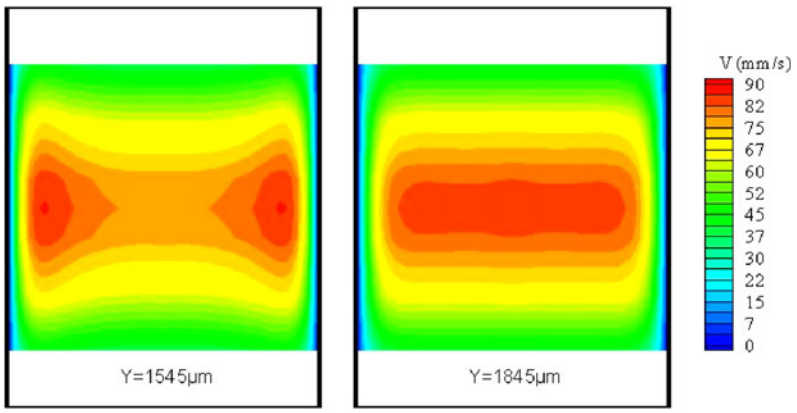

Figure 6. V-velocity component shown in x–z-planes. The data were extracted from the CFD results shown in figure 3 at two y locations. Colour coding of V-component was the same in figures 4 and 6.

of the structure have a slope originating from the underetching during the manufacturing process. This slope was not taken into account in the simulations; i.e. the exit channel was modelled as being rectangular. Furthermore, the width to depth ratio in the exit channel was 7.8, whereas the actual ratio was 9.5. The actual channel dimensions are depicted in figure 5.

The CFD-ACE+ 6.4 software offers several different boundary conditions for the buffer and sample streams to be set, the initial flow rate, the average velocity or the velocity profile. The small dimensions of microsystems usually mean that velocity profiles do not develop fully within the microsystem. Therefore, we chose to run the simulations with both the set flow rates and the average velocities instead of the fully developed profile. Since the results using a set average velocity boundary condition were far more stable, only these are presented in this paper. The known flow rates for buffer and sample stream listed in table 1 were used to derive one set of boundary conditions. The initial velocity of the sheathing stream was set to 44 mm s^{-1} and the velocity of the sample stream was set to 11 mm s^{-1}. Results from the simulations can be seen in figures 6 and 7.

5. Results and discussion

As mentioned above, the measurement volume was about $21 \times 21 \times 16\ \mu m^3$ ($H \times W \times D$). The horizontal dimensions, i.e. the dimensions of the interrogation area, are given by the number of pixels chosen, their size and the magnification of the microscope. The vertical dimension was given by the depth of field of the microscope and depends on the

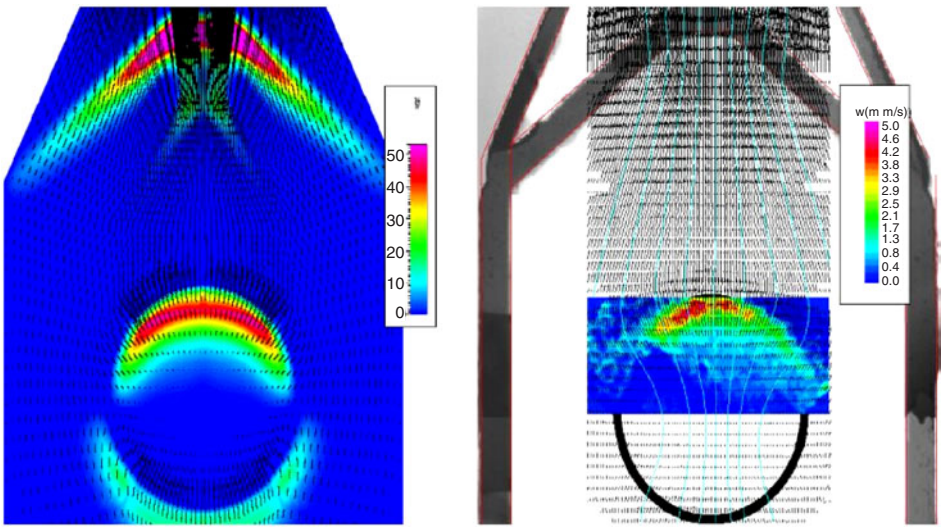

Figure 7. All three velocity components are shown in a plane 30 μm above the chimney. CFD results are shown to the left and PIV to the right. The colour indicates the magnitude of the W-velocity component. In the PIV results, the U, V-velocity vectors were obtained from several camera positions. Stream traces of the U, V-component were shown. The W-component was obtained by combining the results from two overlapping camera positions with a stereoscopic technique.

magnification and the numerical aperture. The higher the magnification of the system the smaller both the interrogation area as well as the depth of field. This means that an increase in magnification produces in principle an overall decreased measurement volume, which would increase the resolution of the PIV measurements.

Nevertheless, opting for an objective with a low magnification has several practical advantages over choosing a high-magnification objective. Low magnification objectives have larger working distances and provide a larger field of view as well as a stronger irradiance onto the light detector. In our set-up it was not easily possible to use a high-magnification objective due to the thick cover glass of the chimney. Apart from this, a second reason for not choosing a high magnification was that the field of view of the system is decreasing with increasing magnification. In our case, the field of view was chosen to cover the entire exit channel width of 600 μm conveniently within one measurement. Therefore, the system magnification for the PIV measurements was set to be tenfold.

This magnification was achieved using a 20 $\times$ /0.40 objective in combination with a 0.5$\times$ relay lens, which is better than using the 10$\times$ /0.25 objective of the microscope, since the higher numerical aperture of the 20$\times$ objective provides a smaller depth of field and an image of higher contrast. The signal strength measured by the detector is given by the irradiance of an imaged particle within the image plane. This irradiance is proportional to the square of the ratio of the numerical aperture to the linear magnification of the chosen objective (Schröder 1998). At a given magnification, a higher numerical aperture value results, therefore, in increased signal strength, which makes the 20$\times$ objective/0.5$\times$ relay lens combination superior to the 10$\times$ objective.

The reliability of the PIV results was examined by comparing the volume flow of the PIV data in the exit channel to the nominal volume flow given by the syringe pumps.

The flow rate was calculated by integration of the velocities over an exit channel cross section, where a standard numerical method (Simpson's rule) was used. A systematical error of about 10% was found, as presented in table 2. The error probably originates from uncertainty in the magnification of the system, since it was not calibrated, and the limited number of planes used for the integration. During all PIV measurements, the flow in the chimney structure was observed to be laminar and without separations, i.e. no convection due to flow separation in the microsystem could be found.

Figures 4 and 6 show the axial velocity in the exit channel at different y locations for $R = 5$. Note that the z-axis in the images is stretched in comparison to the x-axis. A more realistic view of the dimensions is depicted in figure 5.

The PIV data presented in figure 4 show a pair of higher axial velocity streams at all four y locations. The stream pair moves from the bottom of the channel upward passing through the channel. At the same time the two streams were approaching each other slowly up to the point where they begin to join in the last x–z-slice.

The high-velocity stream pair was a result of the five times higher volume flow rate of the sheathing stream interrupted by the sample stream. The highest measured speed of the pair is about 84 mm s^{-1} as indicated by the colour code in figure 4. At first the stream pair flows low in the exit channel, since the sheathing stream acceleration was a result of the reduced cross section at the end of the chimney basin. Within the basin the maximal V-component of the stream velocity was measured to be 78 mm s^{-1}, which is 8% less than the highest speed in the exit channel. Further along the channel, the sheathing stream pair accelerated the sample stream until an equilibrium velocity distribution was reached. This equilibrium profile was not yet fully developed within the measurement range.

The simulated data show similar axial velocity profiles. The cross section at $y = 1545$ μm, in figure 6, contains the high-velocity stream pair, while the downstream cross section

shows the already merged pair. The colour codes that were used in figures 4 and 6 are equal and it can be seen that in both cases the maximum V-component of the stream velocity is the same, about 84 mm s^{-1}. In contrast to the measured cross sections, the high-velocity areas in the simulated cross sections are closer to the sidewalls. Measuring between the highest speed and a speed of about 20 mm s^{-1}, the distance to the sidewall is 40 and 70 μm in the simulations and about 90 μm in the measurements.

There are two main differences between the PIV and simulation results, the facts that the PIV data show a certain asymmetry and that the stream pair merges earlier in the simulations than in the PIV results. The simulated data are necessarily symmetric, since they have been computed in a symmetrical way to save computing power. The measured data on the other hand reflect the fact that the sheathing buffer stream is pushed up at the end of the basin.

The second main difference between the PIV and simulation results was that the stream pair merged about 300 μm earlier in the simulations. While the simulated cross section at $y = 1545$ μm can best be compared to the measured cross section at $y = 1560$ μm, the simulation results show an equilibrium already at $y = 1845$ μm, where the measurements still show two distinct high-speed streams. The reason for the early stream merger in the simulations was due to numerical diffusion.

The speeds of the two sheathing streams and the sample stream differ where the two streams meet. The slower sample stream exerts a viscous drag on the sheathing streams, which flow next to it on both sides. The resulting acceleration of the sample stream can be described as a diffusion of momentum from the high-speed sheathing streams to the slow sample stream. The numerical computing method used in the presented simulations adds an additional equalizing term, which can also be described as a diffusion. This numerical diffusion is an intrinsic part of all numerical calculations. It can only be alleviated by defining a finer mesh or by choosing a different, more complex, method. In both cases a smaller numerical diffusion is bought at the cost of either longer computing time or increased instability. We therefore decided to accept a certain numerical diffusion, which can be found in our results.

The velocity cross sections shown in figure 4 provide information that would otherwise not be easily obtainable without PIV. Although the distribution of the sample flow concentration can be visualized by injecting a dye (Perch-Nielsen *et al* 2001), it is not straightforward to measure the concentration quantitatively. It is even more difficult to make a statement about the flow velocities in the microstructure. PIV on the other hand is designed to measure the flow velocities and with a slight modification of the experiment, the concentration information can be extracted. To achieve this, only the sample flow is seeded with tracer particles, after which it is possible to observe the sample stream qualitatively and quantitatively using the PIV system components.

Observing the chimney structure at different locations with overlapping field of view allowed the construction of a three-dimensional vector field in the area of the actual chimney as shown in figure 7. Both CFD simulation results and PIV measurement results are shown in the figure, where the U- and V-velocity components are rendered as streamlines while the W-velocity components, normal to the plane shown, are encoded in colour. The in-plane velocities were almost zero inside the area of the chimney. In the vicinity of the chimney, the in-plane velocities were in the range of 10 – 20 mm s^{-1} and the flow through the plane (W-component) had a maximum of about 5 mm s^{-1}. The forward flow sped up towards the exit of the basin and reached about 70 mm s^{-1} within the area shown in figure 7.

Since the absolute value of the W-velocity components was adjusted following the CFD results, only the relative PIV measurement results for the W-velocity components can be compared. These results compare reasonably, with the medium W-velocity components between approximately 13 and 30 mm s^{-1} coming up from the chimney in a roughly 530 μm broad and 190 μm long area in the simulation image, while being 480 μm broad and 120 μm long in the measurement image.

Outside the stereoscopic area, the two-dimensional data were also in agreement. From the chimney structure one would expect the average flow velocity to rise somewhere above the actual chimney due to the increase in volume flow and also at the end of the chimney basin, where the cross sectional area decreases. Both speed increases are observed in both the simulation and PIV results. An interesting result of both simulation and PIV measurement was that the highest sample flow velocity was concentrated at the exit-facing rim of the chimney.

In section 3, stereoscopic recombination was discussed and a method was presented to find the scaling factor between the difference in U-component velocities and the W-component velocity. Another approach to find the scaling factor would be to integrate the volume flow over the entire chimney, since the volume flow is known from the pump settings given in table 1. Within the area presented in figure 7, the volume flow is computed to be 0.011 ml min^{-1}. However, the field of view does not cover the entire exit. Using the CFD result, it is seen that the majority (about 80%) of the volume flow exits the chimney within the field of view from the measurement area. Using this fact confirms that the assumed scaling factor was underestimated by more than 20%.

Observing figure 7, it is fairly obvious that the accuracy of the W-velocity component was only limited, given that it was based on the average of 50 samples. The main sources for this large uncertainty are the very small stereoscopic view angles used. The translation of 320 μm corresponds to a stereoscopic view angle of approximately 2×6 degrees, which challenges the accuracy of the measurement. The measurement could be significantly improved by using a higher magnification with shorter working distance, including larger stereo view angles into the measurement. Additionally, a large-format CCD camera could be used to increase the stereoscopic viewing angle, since it allows exploitation of the full viewing capability of the objectives. Finally, more advanced recombination schemes, which take into account the image distortion introduced by the thick cover glass, could be included in the computation of the W-velocity components.

The most desirable measure for improvement of the experimental results would be to equip the examined

microfluidic structure with a thinner cover glass. This would decrease the distortions and make it possible to use objectives with higher numerical aperture. A cover glass thickness of 170 μm would be desirable, since most objectives are designed to be used with such cover glasses.

6. Conclusion

The flow velocities of a microstructure used in cell sorting were mapped in several planes using PIV. The PIV measurements had an adequate resolution and a good field of view. The quantitative results from measurements and simulations were in reasonable agreement, considering the difference in geometry. Furthermore, it was possible to expand the micro-PIV technique to stereoscopic viewing. Combining the stereoscopic technique with mapping of several planes, the possibility of full volume mapping (x, y, z, U, V, W) micro-PIV was demonstrated.

Micro-PIV results can be used to evaluate and validate the simulation results of micro-fluidic flows. In case of the chimney basin, the PIV results support the simulation results. While comparing simulation and PIV data of the exit channel, a certain difference was found, which was helpful as it points out the care that has to be exercised when simulating flow. To improve the agreement between simulation and measurement, the simulation can in principle be improved by using more complex algorithms or by defining a denser mesh at the cost of increased instability or computation time. The measurement can be improved by employing a higher aperture objective, which would increase the viewing angle as well as collect more light. One crucial step towards this end would be the use of a thinner cover glass.

In general, the good agreement between simulation and PIV will allow the simulation software to be used as an efficient tool to speed up the microstructure design cycle.

Acknowledgment

We acknowledge Ulrik Darling Larsen, whose chimney structure we used in our PIV measurements.

References

Goranović G, Perch-Nielsen I P, Larsen U D, Wolff A, Kutter J P and Telleman P 2001 *Proc. 4th Int. Conf. on Modeling and Simulation of Microsystems (March, Hilton Head Island, USA)* pp 242–5

Larsen U D 2000 Micro liquid handling—passive microfluidics *PhD Thesis* Technical University of Denmark, Lyngby, Denmark pp 93–104

Meinhart C D, Wereley S T and Gray M H B 2000 *J. Fluids Eng.* **122** 285–9

Meinhart C D, Wereley S T and Santiago J G 1999 *Exp. Fluids* **27** 414–9

Perch-Nielsen I P, Goranović G, Klank H, Larsen U D, Wolff A, Kutter J P and Telleman P 2001 *Proc. 5th Int. Conf. on Miniaturized Chemical and Biochemical Analysis Systems (October, Monterey, USA)* pp 629–30

Prassad A K and Adrian R J 1993 *Exp. Fluids* **15** 49–60

Schröder G 1998 *Technische Optik* 8th ed (Würzburg: Vogel) p 77

Tashiro K, Sekiguchi T, Shoji S, Funatsu T, Masumoto W and Sato H 2000 *Proc. 4th Int. Symp. on Micro Total Analysis Systems (May, Enschede, The Netherlands)* (The Hague: Kluwer) pp 209–12

Wolff A, Larsen U D, Friis P and Telleman P 2000 *Proc. 14th European Conf. on Solid-State Transducers (August, Copenhagen, Denmark)* pp 235–8

Appendix B

Paper published in Sens. Actuators B Chem.

Title
Theoretical analysis of the low-voltage cascade electroosmotic pump

Authors
Anders Brask, Goran Goranović, and Henrik Bruus

Reference
Sens. Actuators B Chem. **92**, 127-132 (2003)

Available online at www.sciencedirect.com
SCIENCE DIRECT®
Sensors and Actuators B 92 (2003) 127–132
SENSORS AND ACTUATORS B CHEMICAL
www.elsevier.com/locate/sensorb

Theoretical analysis of the low-voltage cascade electro-osmotic pump

Anders Brask, Goran Goranović, Henrik Bruus*

Mikroelektronik Centret (MIC), Technical University of Denmark, DK-2800 Kongens Lyngby, Denmark

Received 11 July 2002; received in revised form 19 December 2002; accepted 17 January 2003

Abstract

The recently published experimental results obtained by Takamura et al. [Y. Takamura, H. Onoda, H. Inokuchi, S. Adachi, A. Oki, Y. Horiike, in: J.M. Ramsey, A. van den Berg (Eds.), Proceedings of the μTAS 2001, Monterey, CA, USA, Kluwer Academic Publishers, Drodrecht, 2001, p. 230], on their low-voltage cascade electro-osmotic pump are analyzed using two different theoretical approaches. One is the semi-analytical equivalent circuit theory involving hydraulic resistances, pressures, and flow rates. The other is a full numerical simulation using computational fluid dynamics. These two approaches give the same results, and they are in good qualitative agreement with the published data. However, our theoretical results deviate quantitatively from the experiments. The reason for this discrepancy is discussed.

PACS: 47.11.+j; 47.60.+i; 47.85.Dh; 82.45

Keywords: Electro-osmotic pump; Equivalent circuit model; CFD simulation

1. Introduction

Micropumps play a key role in the quest for fabricating versatile, cheap, and highly efficient microfluidic lab-on-a-chip devices. In this growing field especially micropumps based on electroosmotic flow (EOF) [1–3] are becoming important [4–9]. They contain no moving parts and are compact. Moreover, they are relatively easy to integrate in microfluidic circuits during fabrication.

One major drawback in the conventional design of EOF micropumps is the use of high voltage to drive the pump. The invention in 2001of the low-voltage cascade EOF pump by Takamura et al. [5] therefore marks an interesting development in the field. In the future, EOF pumps may be powered by battery; and hence, portable.

The aim of our work is two-fold. (1) We want to provide the first theoretical analysis of the experimental results obtained by Takamura et al. [5,10]. (2) Using computational fluid dynamics (CFD) we want to demonstrate that the complex EOF pump is adequately described by the semi-analytical equivalent circuit theory involving hydrodynamic resistances, pressures, and flow rates. Both calculational methods are approximate, but since they are independent and yield comparable results, we have gained confidence in our theoretical results.

2. Principles of the EOF pump

To set the stage for our analysis we briefly recapitulate the working principles of the low-voltage cascade EOF pump [5]. The pump is designed to work as an effective pressure source for low applied voltages. The layout of the pump is shown in Fig. 1.

The main principle is to connect multiple EOF pumps in series in order to accumulate pressure. Each elementary EOF pump (denoted a step) consists essentially of a narrow channel section, marked B in Fig. 1, containing 10 parallel channels, followed by a wide channel section, marked C in Fig. 1, containing a single channel. The EOF in the narrow channel section acts as a high pressure pump with forward electric field. In the wide channel section the electric field is reversed, but here the channel is so wide that the induced back pressure is small compared to the previous pressure. After flowing through one such pump step the accumulated voltage is thus zero, while an appreciable pressure is maintaining a net flow. This ensures EOF pumping using a low operating voltage, indeed an attractive feature allowing the pump to be operated with a battery and thus to be portable. Furthermore, it is more safe to use low voltages.

* Corresponding author. Tel.: +45-4525-6399; fax: +45-4588-7762.
E-mail address: bruus@mic.dtu.dk (H. Bruus).

0925-4005/03/$ – see front matter
doi:10.1016/S0925-4005(03)00130-8

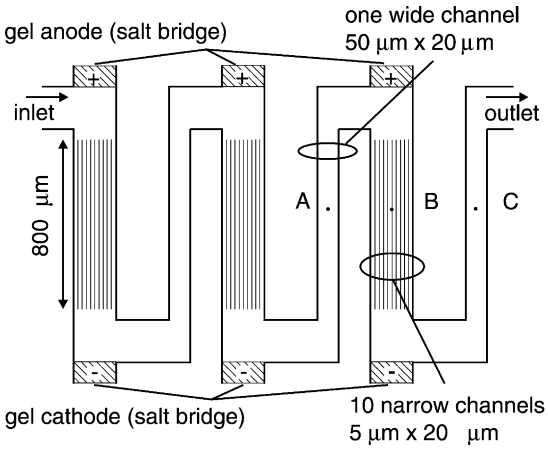

Fig. 1. Top view of the low-voltage cascade EOF pump with three steps (adapted from Fig. 3 in [5]). The total pressure is proportional to the number of steps. The EOF is driven through many parallel narrow channels by a forward electric field and through one wide channel with a reversed electric field. A net flow is thus generated without accumulation of voltage.

The disadvantage of a cascade pump is the extra complexity of the many electrodes.

We begin our analysis by noting that water at room temperature has the kinematic viscosity $v = 10^{-6}$ m^2/s, and when, as in the experiment, it flows with the velocity $u \approx 10^{-3}$ m/s through a channel of width $D = 50$ µm, the Reynolds number, Re, is minute:

$$Re = \frac{uD}{v} = 0.05. \tag{1}$$

For such a low Reynolds number the flow is laminar and the viscous forces are dominant. In the case of uniform flow, i.e. zero spatial derivatives in the flow direction, the Navier-Stokes equation becomes linear.

In this limit, for a steady-state flow through a channel with a hydraulic resistance R_{hyd}, the flow rate Q_{hyd} induced by the pressure drop Δp_{hyd} is

$$Q_{hyd} = \frac{\Delta p_{hyd}}{R_{hyd}}. \tag{2}$$

Polar liquids offer another possibility beyond pure hydrodynamics to generate a flow: namely the electrically driven EOF [1–3]. Ions in the liquid form a thin (<100 nm) electric double layer, the Debye layer, at the walls of the channel, and when an electric potential drop $\Delta\phi_{eo}$ is applied along the channel an EOF is initiated. In the limit of infinitely thin Debye layers, the flow velocity u_{eo} at the walls is given by the Smoluchowski expression

$$u_{eo} = \mu_{eo}\frac{\Delta\phi_{eo}}{L}, \tag{3}$$

where μ_{eo} is the so-called electroosmotic mobility, and L the length of the channel. For a pure EOF, the flow rate Q_{eo} in a channel with cross-sectional area A is given by

$$Q_{eo} = u_{eo}A = \mu_{eo}\frac{\Delta\phi_{eo}}{L}A\frac{R_{hyd}}{R_{hyd}} \equiv \frac{\Delta p_{eo}}{R_{hyd}}, \tag{4}$$

where R_{hyd} and the EOF pressure Δp_{eo} is introduced in the second and third equality, respectively, so that Q_{eo} appears as Q_{hyd} in Eq. (2). In accordance with [6], Δp_{eo} is thus defined by:

$$\Delta p_{eo} = \mu_{eo}\,\Delta\phi_{eo}R_{hyd}\frac{A}{L} = \mu_{eo}\,\Delta\phi_{eo}R_{hyd}\frac{\rho_{el}}{R}, \tag{5}$$

where the geometry ratio A/L equals the ratio between the electric resistivity ρ_{el} of the liquid phase and the electric resistance R of the channel.

Equivalently, Δp_{eo} can be defined as the hydraulic back pressure needed to balance an EOF, i.e. $|Q_{eo}| = |Q_{hyd}|$. The total flow rate Q of a channel with both a pressure-driven flow and an EOF is simply

$$Q = Q_{eo} + Q_{hyd} = \frac{\Delta p_{eo} + \Delta p_{hyd}}{R_{hyd}}. \tag{6}$$

Likewise, the resulting velocity profile is given by a superposition of the velocity profiles of the EOF and the pressure-driven flow, respectively [2].

Consider a pump in a fluidic network. If the back pressure Δp_{hyd} is zero, the flow is denoted a ''free run flow'' and the corresponding flow rate is termed Q_{max}. The counter pressure needed to stop the flow (i.e. $Q = 0$) through the entire pump is denoted the maximum back pressure p_{max}.

3. Analysis of the EOF pump

From Eq. (5), it follows that the EOF-induced pressure buildup is very large in the narrow channel section, and thus the flow profile in this section becomes only slightly deformed under the influence of the actual back pressure. The resulting velocity profile u_1, shown in Fig. 2, is a sum of a large, positive

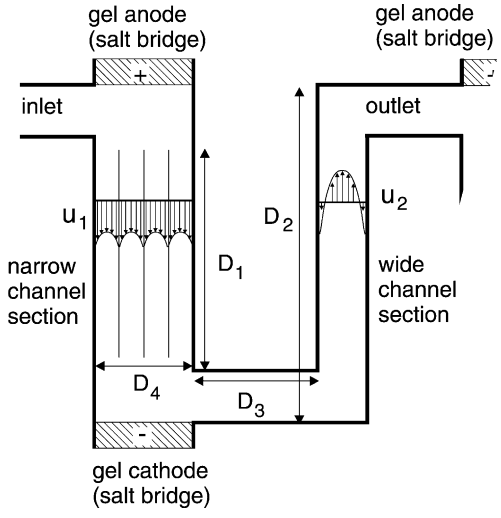

Fig. 2. Simplified schematics of one step of the cascade EOF pump shown in Fig. 1. The flow profiles in both narrow and wide channels are shown. There are 10 channels in the narrow channel section, but for clarity only 4 are depicted. Even though the flow is reversed near the wall in the wide channel, the net flow is still positive. The parameters taken from [5] are: $D_1 = 800$ µm, $D_2 = 1230$ µm, $D_3 = 170$ µm, and $D_4 = 185$ µm.

and flat EOF velocity profile and a small, negative and parabolic back pressure velocity profile. The pressure buildup in the narrow channel section is denoted $\Delta p_{\mathrm{eo}}^{\mathrm{N}}$.

In the wide channel the electric field is reversed. A part of the pressure generated in the narrow section is therefore used both for overcoming the reversed, small, and flat EOF profile and for driving the flow by pressure. The resulting velocity profile is the large, forward parabolic-like velocity profile u_2 shown in Fig. 2. It is evidently imperative to make the channel width considerably larger in this section to keep its back pressure to a minimum. The pressure drop in the wide channel section is denoted $\Delta p_{\mathrm{eo}}^{\mathrm{W}}$.

The final pressure buildup $\Delta p_{\mathrm{step}}^{\max}$ along the whole step is the EOF pressure buildup in the narrow channel section minus the back pressure drop in the wide channel section,

$$\Delta p_{\mathrm{step}}^{\max} = \Delta p_{\mathrm{eo}}^{\mathrm{N}} - \Delta p_{\mathrm{eo}}^{\mathrm{W}}. \tag{7}$$

3.1. Equivalent circuit theory

The concepts from the previous section can be used to analyze the pump using the so-called equivalent circuit theory. In this theory, the hydraulic resistance of a fluidic network is calculated by representing individual sections with equivalent hydraulic resistors using the usual rules for series and parallel resistors. The flow rate and the pressure drop for a hydraulic resistor are related by Eq. (2). For details see [6].

The equivalent circuit theory is only exact for a uniform and laminar flow. Hence, it is not possible to analyze the flow near a bend. In the following analysis the bends are neglected, an approximation justified in Section 3.2 by CFD simulation.

The first step is to find the equivalent diagram for the pump. It consists of a parallel coupling of $N = 10$ identical resistors $R_{\mathrm{hyd},1}$ followed by $R_{\mathrm{hyd},3}$ and $R_{\mathrm{hyd},2}$ in series as shown in Fig. 3b. For a single rectangular channel of width W and height H, R_{hyd} is given by [6],

$$R_{\mathrm{hyd}} = \frac{12\eta L H^{-4}}{(W/H) - \sum_{m=0}^{\infty} (192/(\pi^5(2m+1)^5)) \tanh\left[((2m+1)\pi W)/2H\right]}, \tag{8}$$

where η is the dynamic viscosity. $R_{\mathrm{hyd},1}$ and $R_{\mathrm{hyd},2}$ are then computed using Eq. (8). The short channel connecting the narrow and wide channel sections can safely be neglected,

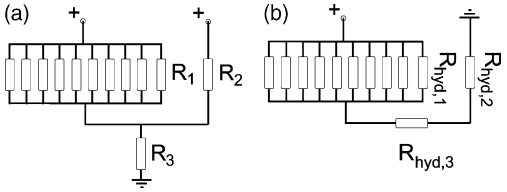

Fig. 3. (a) The equivalent electrical circuit used in the calculation of potential drop across the EO section. (b) The slightly different equivalent circuit for the fluidic network used in the calculation of flow rates. There are $N = 10$ narrow channels each with the hydraulic resistance $R_{\mathrm{hyd},1}$. In our calculations $R_{\mathrm{hyd},3}$ is neglected.

since $R_{\mathrm{hyd},3} \ll R_{\mathrm{hyd},1}, R_{\mathrm{hyd},2}$. The total hydraulic resistance $R_{\mathrm{hyd}}^{\mathrm{total}}$ is therefore given as

$$R_{\mathrm{hyd}}^{\mathrm{total}} = N^{-1} R_{\mathrm{hyd},1} + R_{\mathrm{hyd},2}. \tag{9}$$

To drive the EOF an external electrical potential, $\Delta\phi_{\mathrm{ch}}$, is applied to the resistor network (Fig. 3a). Only a fraction α of $\Delta\phi_{\mathrm{ch}}$ is dropped over the EOF channels. This effective potential drop is denoted $\Delta\phi_{\mathrm{eo}}$,

$$\Delta\phi_{\mathrm{eo}} = \alpha\, \Delta\phi_{\mathrm{ch}}. \tag{10}$$

Using the circuit diagram we determine α. The electrical resistance of a single rectangular channel with length L, width W, and height H is given by

$$R = \rho_{\mathrm{el}} \frac{L}{HW}. \tag{11}$$

Combining this with the actual geometry of Fig. 1, it follows that

$$\alpha = \frac{(N/R_1 + 1/R_2)^{-1}}{(N/R_1 + 1/R_2)^{-1} + R_3} = 0.885. \tag{12}$$

The actual applied potential $\Delta\phi_{\mathrm{app}}$ does not equal $\Delta\phi_{\mathrm{ch}}$ because further potential drops occur in the gel electrodes. Hence, $\Delta\phi_{\mathrm{eo}}$ is unknown but could have been estimated if the electrical current and conductivity of the liquid had been measured experimentally.

At this point the EOF pressures $\Delta p_{\mathrm{eo}}^{\mathrm{W}}$, $\Delta p_{\mathrm{eo}}^{\mathrm{N}}$, and Δp_{step} can be found for a given potential. However, it remains to verify the validity of the approximate equivalent circuit theory. This is done by numerical simulations in the following.

3.2. Computational fluid dynamics

A full numerical simulation was performed using the commercial computational fluid dynamics program Coventor 2001.3. The program can simulate EOF in the limit of infinitely thin Debye layers. The electric potential is calculated first, and by the Smoluchowski relation Eq. (3) it is used to establish the boundary conditions for the velocity field at the walls. The accuracy of the CFD could be measured for straight channels with rectangular cross-section, since there the equivalent circuit model gives analytical answers.

In order to save calculation time, it is important to identify the minimal computational domain. Only one pump step needs to be analyzed. Further simplifications can be achieved by symmetry considerations. Clearly, the pump is symmetric about the horizontal plane at half the channel depth. Due to the very low Reynolds number, $Re < 0.05$, the flow is said to be creeping. Numerical investigation by Yang

et al. [11] showed that for a 90° bend, inertial effect was negligible for $Re < 5$. Consequently, it does not matter which way the liquid flows. The flow pattern in the first half of a pump step (e.g. between A and B in Fig. 1) therefore equals that in the second half (e.g. between B and C in Fig. 1). Hence, only half of the computational domain needs to be considered. This was verified by a full-geometry simulation. The flow rate and pressure buildup for the complete pump step are twice the values obtained using the symmetry-reduced geometry.

The CFD simulation was done with various grids to find those yielding grid-independent results. We focused especially on problems at the corners, since they are known to be problematic [12]. We ended using a grid containing 10^5 rectangular cells with 14×7 cells in each cross-section. The CFD results for this grid matched the analytical circuit model within 5%.

4. Results and discussion

4.1. Velocity profiles

A simulation of the low-voltage cascade EOF pump gave the velocity profiles depicted in Fig. 4. There is one profile for the wide channel, and one for a single narrow channel. The profiles have been extracted from the symmetry plane. The CFD program solves the Poisson equation for a given potential drop $\Delta\phi_{ch}$ and finds that the electric fields are slightly different in the wide and narrow channels. In the circuit model they are assumed to be the same. The calculated velocity profiles at two positions are sketched in Fig. 2.

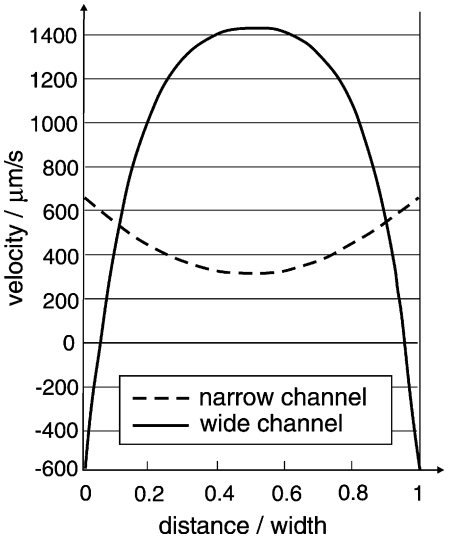

Fig. 4. CFD simulated velocity profiles at the symmetry plane in a wide and a narrow channel. The velocity at the walls is the EOF velocity. The parameters are: $\eta = 1.00 \times 10^{-3}$ Pa s, $\mu_{eo} = 0.06$ mm^2/(V s), and $\Delta\phi_{ch} = 10$ V.

4.2. Comparison with experiments

The circuit model is now used to calculate the back pressure p_{max} and the EOF velocity u_{eo} as a function of the potential drop. Unfortunately, neither the actual potential drop $\Delta\phi_{ch}$ nor the EOF mobility μ_{eo} was measured in the experiment. However, both back pressure and flow velocity depend linearly on the product $\mu_{eo}\,\Delta\phi_{ch}$, and, as we shall see, this makes a comparison between experiments and theory possible.

In the case of a 15-step cascade pump, Takamura et al. [5] measured a max back pressure of 800 Pa and for the same voltage and under free run conditions, a max velocity $u_{max} = 0.50$ mm/s. The velocity measurements were conducted in the last wide section, which had no electric field. Hence, the flow is solely pressure driven.

The relation between the back pressure and the product $\mu_{eo}\,\Delta\phi_{ch}$ is found using Eqs. (5) and (7), and it is plotted in Fig. 5. From the figure, it is found that the measured 800 Pa corresponds to $\mu_{eo}\,\Delta\phi_{ch} = 0.114$ mm^2/s. Using this value the model predicts the flow rate $Q_{max} = 0.110$ nl/s. From this flow rate, the maximum velocity u_{max} may be calculated in the wide channel section.

Using the aspect ratio as a variable parameter, we performed a general analysis of the relation between flow rates and maximal flow velocities in rectangular channels with cross-section area A. For the actual aspect ratio $W/H = 2.5$ we found a numerical factor 0.52:

$$u_{max} = \frac{Q_{max}}{0.52\,A} = 0.21\ \text{mm/s}, \tag{13}$$

where $A = 50 \times 20$ µm^2. This velocity, found both by simulation and by the circuit model, deviates by a factor 2.4 from the measured 0.50 mm/s.

In [5], results from a 6-step and 15-step pump are presented. The back pressure measurements give 380 and 860 Pa for the 6-step and 15-step pump, respectively, at $\phi_{app} = 25$ V. The corresponding ratio is then $860/380 = 2.26$ which should be compared with $15/6 = 2.5$. Hence, it can be concluded that the pressure is not accumulated linearly with the number of steps in contrast to theoretical expectations. The deviation may be within the range of uncertainty for the pressure measurements.

To obtain realistic estimates for the absolute values of the EOF pump parameters, we use some typical values for μ_{eo} and $\Delta\phi_{ch}$. The results for Q_{max}, p_{max}, and R_{hyd} obtained by model calculations and simulations are compared in Table 1

Table 1
Comparisons between equivalent circuit model and numerical simulation for a single pump step

	Q_{max} (nl/s)	p_{max} (Pa)	R_{hyd} (kg/(m^4 s))
Model	0.577	281.0	4.88×10^{14}
Simulation	0.560	274.0	4.89×10^{14}
Deviation	3%	2%	0%

Parameters: $\mu_{eo} = 0.06$ mm^2/(V s), $\eta = 1.0 \times 10^{-3}$ Pa s, $\Delta\phi_{ch} = 10$ V.

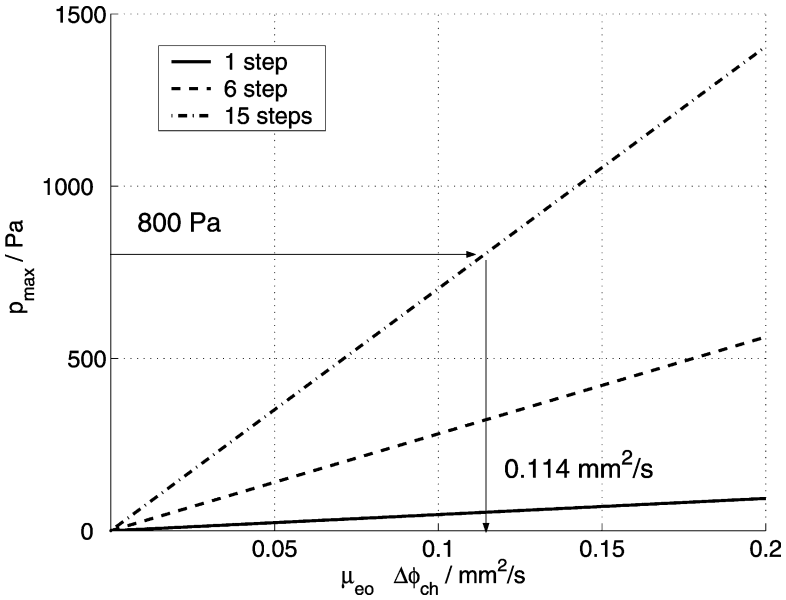

Fig. 5. Maximum back pressure as a function of $\mu_{eo}\,\Delta\phi_{ch}$. The pressures are calculated using the equivalent circuit theory. The one step slope is 468 Pa s / mm^2 for $\eta = 1.00 \times 10^{-3}$ Pa s, $\alpha = 0.885$. The measured pressure of 800 Pa leads to a value $\mu_{eo}\,\Delta\phi_{ch} = 0.114$ mm^2/s.

for a given set of parameters. The two sets of results agree well. Calculations with $\mu_{eo} = 0.06$ mm^2/(V s) give considerably larger pressures than those measured, e.g. 4200 Pa for the 15-step pump with $\Delta\phi_{ch} = 10$ V. This indicates the possibility for improving the performance of the pump.

5. Discussions and conclusions

Discussions with Takamura [10] have led to the following conclusions regarding the discrepancies between experiment and theory.

(1) The velocity mismatch of a factor of 2.4 is probably due to fabrication difficulties. The actual width of the narrow channels may have been as large as 8 μm instead of the design value of 5 μm [10]. Since $\Delta p_{eo} \propto W^{-2}$ for $W \ll H$, the pressure for a 8 μm wide channel is $(8/5)^2 = 2.6$ times smaller than for a 5 μm channel. This would lower the slopes of the lines in Fig. 5 and instead of reading off 0.114 mm^2/s on the abscissa, we would get 0.296 mm^2/s. Using this number for $\mu_{eo}\,\Delta\phi_{ch}$, we obtain $u_{max} = 0.55$ mm/s. This result agrees better with the observed 0.5 mm/s. A source for minor inaccuracies is the actual shape of the channel cross-section.

(2) The pressure does not increase linearly with the number of stages. Two possible explanations of this observation are: (a) due to the design of the pump the individual gel electrodes do not have the same potential; (b) pressure-dependent hydraulic resistances of the gel electrodes, i.e. leaks in the gel electrodes increases with increasing pressure.

(3) The experimental accuracy of the velocity and pressure measurements is 15–30%. Part of the discrepancies could therefore simply arise from inaccurate measurements.

The above explanations can account for the large quantitative deviations between theory and experiment, and the problems will be addressed in coming improved version of the low-voltage cascade EOF pump [10].

In summary, we have presented a simple analytical model for the low-voltage EOF pump obtained by using equivalent circuit theory. This approximate model has proved sufficient for making good estimates of the performance of the pump. Full CFD numerical simulations were made to verify the model and to provide more detailed information about the flow. The model and the simulations agree within 3%. Our theoretical analysis was compared to experimental results obtained by Takamura et al. [5], and good qualitative agreement was observed. However, a considerable quantitative deviation (a factor of 2.4) was found for values of calculated versus measured maximum velocity. The possible sources for this discrepancy were identified as inaccuracies in the measurement of various parameters (channel widths, velocities, and pressures) and pressure leakages.

Our work shows the advantage of theoretical analysis as a supplement to the experimental approach in the study of EOF pumps. Our pressure calculations indicate, for example, that there is room for improving the performance of the pump. We have also shown that, although approximate, the equivalent circuit model is applicable to the cascade EOF pump. This is mainly because the corrections from electrical and hydraulic corner effects are negligible. Use of the circuit model facilitates the analysis of the pump enormously.

Acknowledgements

We are grateful to Yuzuru Takamura and his colleagues at the University of Tokyo for their openness and great help in our discussions by email during this work and for providing us with experimental details not presented in [5]. We also thank our colleagues from the μTAS project at Mikroelektronik Centret, especially Jörg Kutter, for support and stimulating discussions. This work was partly supported by the Danish Technical Research Council, μTAS Frame Program Grant No. 9901288.

References

[1] J.F. Osterle, J. Appl. Mech. 31 (1964) 161.
[2] C.L. Rice, R. Whitehead, J. Phys. Chem. 69 (1965) 4017.
[3] A. Manz, C.S. Effenhauser, N. Burggraf, D.J. Harrisson, K. Seiler, K. Fluri, J. Micromech. Microeng. 4 (1994) 257.
[4] P.H. Paul, D.W. Arnold, D.J. Rakestraw, Proceedings of the μTAS 1998, Banff, Canada, 1998, p. 49.
[5] Y. Takamura, H. Onoda, H. Inokuchi, S. Adachi, A. Oki, Y. Horiike, in: J.M. Ramsey, A. van den Berg (Eds.), Proceedings of the μTAS 2001, Monterey, CA, USA, Kluwer Academic Publishers, Drodrecht, 2001, p. 230.
[6] W.E. Morf, O.T. Guenat, N.F. de Rooij, Sens. Actuators B-Chem. 72 (2001) 266.
[7] O.T. Guenat, D. Ghiglione, W.E. Morf, N.F. d Rooij, Sens. Actuators B-Chem. 72 (2001) 273.
[8] S. Zeng, C.-H. Chen, J.C. Mikkelsen Jr., J.G. Santiago, Sens. Actuators B-Chem. 79 (2001) 107.
[9] D.R. Reyes, D. Lossifidis, P.-A. Auroux, A. Manz, Anal. Chem. 74 (2002) 2623.
[10] Experimental parameters not quoted in the original experimental paper were kindly provided by Dr. Y. Takamura, Univ. Tokyo.
[11] R.-J. Yang, L.-M. Fu, Y.-C. Lin, J. Colloid Interf. Sci. 239 (2001) 98.
[12] N.A. Patankar, H.H. Hu, Anal. Chem. 70 (1998) 1870.

Appendix C

Paper published in J. Micromech. Microeng.

Title
The clogging pressure of bubbles in hydrophilic microchannel contractions

Authors
Mads Jakob Jensen, Goran Goranović, and Henrik Bruus

Reference
J. Micromech. Microeng. **14** (2004)

INSTITUTE OF PHYSICS PUBLISHING JOURNAL OF MICROMECHANICS AND MICROENGINEERING

J. Micromech. Microeng. **14** (2004) 1–8 PII: S0960-1317(04)72206-8

The clogging pressure of bubbles in hydrophilic microchannel contractions

Mads Jakob Jensen, Goran Goranović and Henrik Bruus

MIC - Department of Micro and Nanotechnology, Technical University of Denmark, Oersteds Plads, Bldg. 345 East, DK-2800 Kgs. Lyngby, Denmark

E-mail: mjj@mic.dtu.dk

Received 19 November 2003
Published DD MMM 2004
Online at stacks.iop.org/JMM/14/1 (DOI: 10.1088/0960-1317/14/0/000)

Abstract
We present a theoretical and numerical study of the quasi-static motion of large wetting bubbles in microfluidic channels with contractions. In most cases the energy of a bubble increases when it is moved from a wide channel to a narrow one, and the bubble thus tends to clog the flow of the fluid. A certain pressure, the so-called clogging pressure, is needed to push the bubbles out of the contraction. However, we show that in the case of a hydrophilic channel contraction there exists a range of parameter values where the bubble actually gains energy by moving into the narrow part. For these specific cases we analyze how the clogging pressure depends on channel geometry, surface tension and contact angle. Based on our analysis we establish design rules for minimizing the clogging pressure of microchannel contractions.

1. Introduction

Many microfluidic networks on modern lab-on-a-chip devices contain channel contractions. These tend to become problematic if, as is often the case, gas bubbles are introduced into the liquid at the inlets or by electrochemical processes. Due to the small channel dimensions gas bubbles can easily be large enough to span the entire channel cross-section. Such 'large' bubbles are prone to get stuck at the channel contraction, whereby they can clog the flow and disturb measurements or functionality of the system in an uncontrolled manner. To clear the clogged channel an external pressure, the so-called clogging pressure, has to be applied to push the clogging bubble out of the system. Although already identified nearly a decade ago [1, 2], this important problem in microfluidic systems has not been studied theoretically to a wide extent, a situation we would like to amend with this paper. The present work is a substantial extension of a preliminary and specialized study presented at the NanoTech 2003 conference, [3] now including an analysis of the bubble energies in general cases, inclusion of compressibility effects and the use of different parameter values.

A complete analysis of the motion of a large bubble through a microchannel contraction involves many different physical effects, some which are not completely understood. Any comprehensive analysis would at least require detailed modeling of the liquid–gas, liquid–solid and solid–gas interfaces as well as the dynamics in the bulk fluids. But also more complicated processes near the contact lines need to be addressed, e.g. wetting [4–6], contact line pinning and hysteresis [4, 7], dynamic contact angles and contact lines [8–10] and static and dynamic friction [11–13]. It should be stressed that many of these surface effects are hard to control precisely, therefore dynamical systems where the lubrication assumption is used are also widely analyzed [14, 15].

In this work, however, we will restrict our analysis to quasi-static motion of bubbles. By this we mean that the velocity of the bubble is nearly zero and that the entire model system remains arbitrarily close to equilibrium for all bubble positions. All dynamic aspects are thus neglected, and basically the model involves only the free energy of the internal interfaces of the system and external pressures. This is motivated by the fact that it is difficult to experimentally control surface related properties. We thus only study geometry related effects. We also choose to work only with axisymmetric channels of smooth (but otherwise arbitrary) contraction geometries free from any sharp corners and other singularities. With these simplifications the forces or pressures needed to push a bubble through the system can be calculated accurately without losing the essential physics of the problem. This in turn enables us to formulate design rules for microchannel contractions to prevent or reduce clogging.

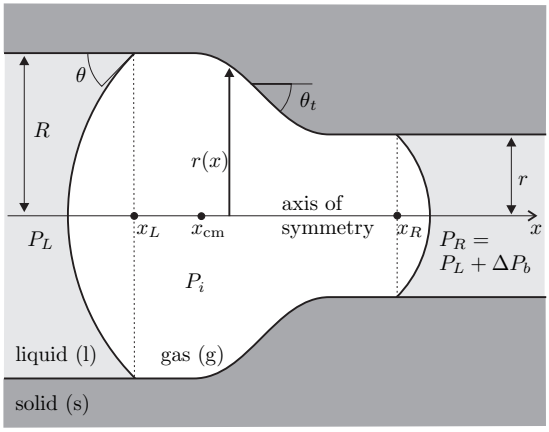

Figure 1. A bubble with internal pressure P_i and center of mass $x_{\rm cm}$ in a hydrophilic axisymmetric channel. The left (right) contact line has the coordinate $x_{\rm L}$ ($x_{\rm R}$) and contact angle θ. The channel is contracting from a straight part of radius R to one of radius r. The specific channel profile is defined by some function $r(x)$. Throughout this paper we have chosen $r(x)$ to be a sloped straight line joined to the straight parts by two circle arcs. The tapering angle $\theta_{\rm t}$ is given by $\tan\theta_{\rm t} = -r'(x)$. The pressure left (right) of the bubble is denoted as $P_{\rm L}$ ($P_{\rm R}$) and the pressure difference across the bubble is $\Delta P_{\rm b}$.

To our knowledge similar analyses have only been made on channels of constant cross-sections [16] and for the special case of sudden contractions [17].

2. The model and basic physical assumptions

Consider a hydrophilic microfluidic channel or capillary, such as the one depicted in figure 1, which is axisymmetric about the x axis with a position dependent channel radius $r(x)$. The channel is filled with a liquid. A large bubble of some other fluid (we think mainly of a gas such as air) is present in the liquid. By large we mean that the volume of the bubble is larger than the volume $V_{\rm sph}^{\rm max}$ of the largest inscribed sphere that can be placed anywhere in the microchannel. A large bubble divides the liquid into two disconnected parts, left and right of the bubble. The bubble itself consists of a bulk part in direct contact with the walls of the channel and of two menisci, in contact with the liquid, capping the ends of the bubble.

The bubble is assumed to be in quasi-static equilibrium. In that case it is relatively simple to combine mass conservation with geometric constraints to determine, as a function of the bubble position, the pressure drops over the two menisci needed to maintain this equilibrium. We define our central concept, the clogging pressure, as the maximum of the position dependent pressure drop across the bubble, i.e. the minimal external pressure that must be supplied to push the bubble through the microchannel.

2.1. The Young and Young–Laplace equations

Our model system consists of a solid channel containing a liquid and one large gas bubble. Therefore, the essential physical parameters are the three surface tensions (surface free energy per area) $\sigma_{\rm lg}$, $\sigma_{\rm sl}$ and $\sigma_{\rm sg}$ for the liquid–gas, solid–liquid and solid–gas interfaces, respectively. In equilibrium the contact angle θ is determined by the surface tensions through the Young equation [18, 19]

$$\sigma_{\rm sg} - \sigma_{\rm sl} = \sigma_{\rm lg}\cos\theta. \tag{1}$$

In the following the contact angle is taken as the equilibrium angle or rather as an average contact angle. Because contact angle hysteresis is very sensible to surface effects, we do not address these questions in this work.

To sustain a curved interface with the main radii of curvature R_1^c and R_2^c between a gas of pressure $P_{\rm g}$ and a liquid of pressure $P_{\rm l}$, the pressure difference $\Delta P = P_{\rm g} - P_{\rm l}$ must obey the Young–Laplace equation [20]

$$\Delta P = \sigma_{\rm lg}\left(\frac{1}{R_1^c} + \frac{1}{R_2^c}\right) = 2\sigma_{\rm lg}\,\frac{\cos\theta}{r}, \tag{2}$$

where the last equation is applicable for a constant circular cross-section of radius r. We use the standard convention that these radii are taken as positive if the interface is concave when seen from the gas.

2.2. Isothermal motion and compressibility

In the rest of the paper we consider a 'large' bubble having the initial position '1' in the widest part of the channel. The initial volume is $V_1 = \gamma V_{\rm sph}^{\rm max}$, where $\gamma > 1$ and $V_{\rm sph}^{\rm max} = 4\pi r_1^3/3$, and the corresponding internal pressure is $P_{i,1}$. At a later stage the bubble is moved to a position '2', where the volume is V_2 and the internal pressure is $P_{i,2}$. In the quasi-static case the bubble motion is isothermal and hence the compressibility condition applies,

$$P_{i,1}V_1 = P_{i,2}V_2. \tag{3}$$

The pressure P_i within the bubble is given as the external pressure P_0 plus the pressure change ΔP across the curved interface, given by equation (2).

The most extreme compression is obtained by pressing a large bubble, which floats without geometrical constraints in a bulk liquid of pressure P_0, into a narrow circular channel of radius r. Combining equations (2) and (3) yields

$$\frac{V_1}{V_2} = \frac{P_{i,2}}{P_{i,1}} \approx \frac{P_{i,2}}{P_0} = 1 + \frac{2\sigma_{\rm lg}\cos\theta}{rP_0}. \tag{4}$$

For example, moving a large spherical air bubble in water ($\sigma_{\rm lg} = 0.0725\,{\rm J\,m^{-2}}$) at the ambient pressure $P_0 = 10^5\,{\rm Pa}$ into a channel of radius $r = 25\,\mu{\rm m}$ leads to $V_1/V_2 \approx 1.06$, i.e. a volume compression of 6%. Moving, as in section 6, a bubble from a $300\,\mu{\rm m}$ to a $190\,\mu{\rm m}$ wide channel yields a compression of about 0.2%.

In the case of laser ablated microchannels in plastic chips, compressibility effects are negligible as the smallest dimensions typically are greater than $100\,\mu{\rm m}$. However, for silicon based micro- or nanofluidic devices, compressibility may play a significant role.

2.3. Quasi-static motion and geometry

For a bubble positioned in a microchannel contraction, the total internal energy $E_{\rm tot}$ is the sum of the surface free energy, gravitational energy, kinetic energy and frictional energy. We regard the surrounding pressures as external energy. By our definition quasi-static motion of an incompressible bubble implies that the kinetic energy is zero and friction is also

zero because of hydrostatic and thermodynamic equilibrium. Finally, we treat channels of characteristic dimensions $2r$ less than 300 μm, which is significantly smaller than the capillary length of water, $\Delta_c = \sqrt{\sigma_{\rm lg}/\rho_{\rm l} g} \approx 2700\,\mu$m, where $\rho_{\rm l} = 10^3$ kg m^{-3} and $g = 9.82$ m/s^2. So the gravitational energy can also be neglected, which ensures that the menisci may be approximated by spherical caps.

The total internal energy $E_{\rm tot}$ of the microchannel containing a quasi-statically moving bubble is given only by the surface free energy, i.e. the sum of interfacial energies σ_i times interfacial areas A_i,

$$E_{\rm tot} = \sum_i \sigma_i A_i = \sigma_{\rm lg} A_{\rm lg} + \sigma_{\rm sg} A_{\rm sg} + \sigma_{\rm sl} A_{\rm sl}. \tag{5}$$

The pressure-related applied external force F needed to balance the bubble is given by the gradient of the total internal energy with respect to the center of mass coordinate of the bubble $x_{\rm cm}$. Hence

$$F = \frac{{\rm d}E_{\rm tot}}{{\rm d}x_{\rm cm}}, \tag{6}$$

which thus depends on the bubble position $x_{\rm cm}$ and, through the areas A_i, on the geometry of the channel.

2.4. The clogging pressure

The Young–Laplace pressure drops (cf equation (2)) at the menisci are given by,

$$\Delta P_{\rm L} = P_i - P_{\rm L}, \tag{7a}$$

$$\Delta P_{\rm R} = P_i - P_{\rm R}. \tag{7b}$$

The total pressure drop $\Delta P_{\rm b}(x_{\rm cm})$ over the bubble as a function of its center of mass $x_{\rm cm}$ is given by

$$\Delta P_{\rm b}(x_{\rm cm}) = P_{\rm R} - P_{\rm L} = \Delta P_{\rm L}(x_{\rm cm}) - \Delta P_{\rm R}(x_{\rm cm}). \tag{8}$$

The clogging pressure $P_{\rm clog}$ is defined as the maximal position dependent pressure drop across the bubble,

$$P_{\rm clog} = \max\{-\Delta P_{\rm b}(x_{\rm cm})\}. \tag{9}$$

The clogging pressure expresses the minimal amount by which the left-hand-side pressure $P_{\rm L}$ must exceed the right-hand-side pressure $P_{\rm R}$ to push the bubble through the contraction quasi-statically from left to right.

3. General energy considerations for axisymmetric microchannels

Consider a bubble placed in a cylindrical channel of radius R. We want to determine the change in energy resulting from moving it into a smaller channel of radius $r < R$, e.g. by moving it from left to right in the channel depicted in figure 1. Intuitively, we would expect the energy to increase as a result of the movement. In most cases this intuition is correct; however, we shall see that in some cases the system gains energy by the move, solely due to geometric conditions.

The bubble has the initial volume $V_1 = \gamma V_{\rm sph}^{\rm max}$, where $\gamma > 1$ and $V_{\rm sph}^{\rm max} = 4\pi R^3/3$. With this constraint the bubble is forced to touch the walls regardless of its position. According to equations (2) and (7*b*) the internal pressure of the bubble is

$$P_{i,1} = P_{\rm R} + 2\sigma_{\rm lg}\frac{\cos\theta}{R}. \tag{10}$$

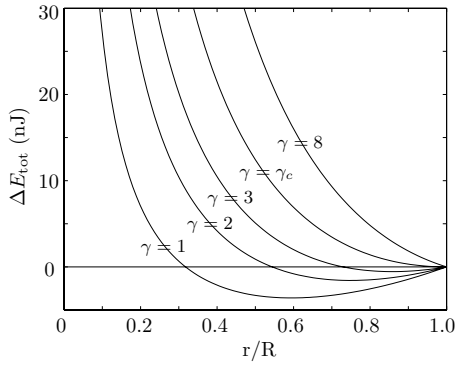

Figure 2. Plot of the energy change $\Delta E_{\rm tot}$ as a function of the ratio r/R. The bubble is moved from a wide channel of radius $R = 150\,\mu$m to a narrow channel of radius r. Five curves are shown corresponding to the volume ratio $\gamma = 1, 2, 3, \gamma_{\rm c}$ and 8, respectively, $\gamma_{\rm c} \approx 4.75$. For 'small' volumes $1 \leqslant \gamma < \gamma_{\rm c}$ the system can gain energy by moving the bubble to the narrow channel, if the width of the latter is not too small. For $\gamma > \gamma_{\rm c}$ the movement requires energy in all cases.

The volume of the bubble is the sum of two spherical cap volumes and the volume of a cylinder of initial length L. Once the length L is known, the relevant interfacial areas $A_{\rm lg}$ and $A_{\rm sg}$ may be found.

The gas bubble is now moved to the cylindrical channel of radius r, and according to equations (2), (3) and (7*b*) the pressure $P_{i,2}$ and volume V_2 are

$$P_{i,2} = P_{\rm R} + 2\sigma_{\rm lg}\frac{\cos\theta}{r}, \tag{11}$$

$$V_2 = \frac{P_{i,1}}{P_{i,2}}\,V_1. \tag{12}$$

By solving equation (12) it is straightforward to find the change in total free surface energy,

$$\Delta E_{\rm tot} = E_{\rm tot,2} - E_{\rm tot,1} = \sigma_{\rm lg}(A_{\rm lg,2} - A_{\rm lg,1}) + \sigma_{\rm lg} 2\pi\cos\theta(rl - RL), \tag{13}$$

where l is the length of the bubble in the channel of radius $r < R$ (situation 2). In equation (13) the Young relation (1) has been used to eliminate the solid–liquid and solid–gas interfacial energies.

Based on equation (13) we can analyze the energy change when moving the bubble from the wide channel of radius R to the narrow channel of radius r. First we give the limiting values of $\Delta E_{\rm tot}$. In the limit $r/R \to 1$ we obviously get $\Delta E_{\rm tot} \to 0$. In the opposite limit, $r/R \to 0$, the compressibility of the bubble results in convergence of $\Delta E_{\rm tot}$,

$$\lim_{\frac{r}{R}\to 0} \Delta E_{\rm tot} = \frac{\pi R^3}{3}\left(4\gamma R P_{\rm R} - \sigma_{\rm lg}\,\frac{4 + \sin(3\theta) - 3\tan\theta}{\cos^2\theta}\right). \tag{14}$$

To discuss $\Delta E_{\rm tot}$ for general values of r/R we use a numerical example: an air bubble in a water filled PMMA channel for which we have the parameter values $P_{\rm R} = 10^5$ Pa, $\sigma_{\rm lg} = 72.5$ mJ and $\theta = 72^\circ$. The radius ratio r/R and the volume parameter γ are then varied.

In figure 2 the energy $\Delta E_{\rm tot}$ (equation (13)) is plotted as a function of the ratio r/R for given values of γ. The

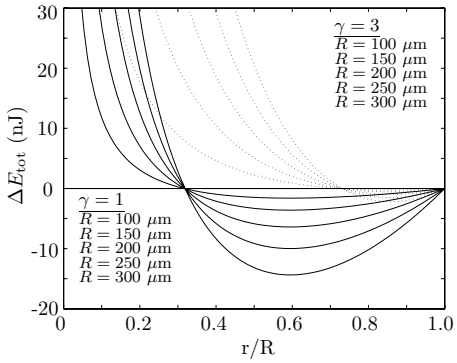

Figure 3. The energy $\Delta E_{\rm tot}$ as a function of the ratio r/R for different values of the wide channel radius, $R = 100, 150, 200, 250$ and $300\,\mu$m. The plain curves correspond to the smallest bubble for $\gamma = 1$ and the dotted curves correspond to a larger bubble with $\gamma = 3$.

figure shows that for large values of γ, i.e., large bubbles, it requires energy ($\Delta E_{\rm tot} > 0$) to move the bubble from the wide to the narrow channel. However, there exists a critical value $\gamma_{\rm c} \approx 4.75$ below which the system can gain energy by moving the bubble, if the radius ratio r/R is not too small. This behavior is generic for a bubble in a contracting channel, but the specific shape of the curve and the optimal minimum depend on the material parameters and the external pressure $P_{\rm R}$.

The critical value $\gamma_{\rm c}$, above which energy gain is impossible, is given by $\partial \Delta E_{\rm tot}/\partial(r/R) = 0$ at $r/R = 1$,

$$\gamma_{\rm c} = \frac{(3 - \cos(3\theta) + 2\sin\theta)(2\sigma_{\rm lg}\cos\theta + RP_0)}{2RP_{\rm R}\cos\theta(1 + \sin\theta)}. \qquad (15)$$

Figure 3 depicts the energy $\Delta E_{\rm tot}$ as a function of the ratio r/R for $\gamma = 1$ and $\gamma = 3$, and for five values of the wide channel radius, $R = 100, 150, 200, 250$ and $300\,\mu$m. From equation (13) it may be seen that $\min\{\Delta E_{\rm tot}\} \propto R^2$ as the area is proportional to R^2 and L is proportional to R. Deviations from this proportionality arise for small values of R because of compressibility. For $\gamma = 1$ in figure 3 we find $\max\{-\Delta E_{\rm tot}\} = kR^2$ with $k = 0.159\,{\rm J\,m^{-2}}$. This proportionality is illustrated as the energy at a given r/R point is increased by a factor 4 when R is doubled, e.g. from $R = 150\,\mu$m to $R = 300\,\mu$m.

The previous calculations clearly show that for some geometries it is favorable to place the bubble in the narrow rather than in the wide part of the channel. In the following we shall address the question of whether for such geometries the bubble will move spontaneously or it must cross an energy barrier to arrive at the low-energy state in the narrow channel.

4. Analytical results for contractions with energy gain

Combining the geometry defined in figure 1 with equations (2) and (8), the central expression of our analysis is easily derived,

$$\Delta P_{\rm b} = 2\sigma_{\rm lg}\left(\frac{\cos[\theta - \theta_{\rm t}(x_{\rm L})]}{r(x_{\rm L})} - \frac{\cos[\theta + \theta_{\rm t}(x_{\rm R})]}{r(x_{\rm R})}\right). \qquad (16)$$

From the discussion in section 2.4 it follows that if $\Delta P_{\rm b} < 0$ then the contraction causes bubble clogging, whereas for

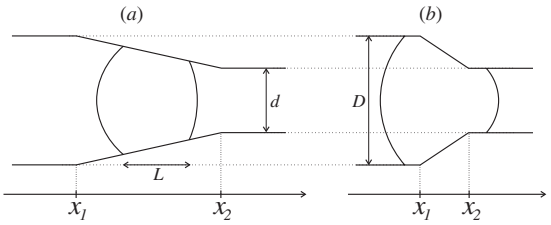

Figure 4. Two generic situations for a bubble of length $L = x_{\rm R} - x_{\rm L}$ near a microchannel contraction of length $x_2 - x_1$. (*a*) The contraction is long enough to contain the entire bubble, i.e. $x_{\rm R} - x_{\rm L} < x_2 - x_1$. (*b*) The contraction is so short that the bubble can span it completely, i.e. $x_{\rm R} - x_{\rm L} > x_2 - x_1$, which is a class β_4 bubble.

$\Delta P_{\rm b} > 0$ the bubble tends to move spontaneously through the contraction toward the narrow part.

Based on equation (16) a number of design rules may be established specifying the geometric features that may prevent or decrease clogging. Consider a bubble that starts out in the wide straight section left of the contraction, where it has a length $L_0 = x_{\rm R} - x_{\rm L}$. The pressure drop $\Delta P_{\rm b}$ is zero to begin with, but depending on the shape of the contraction, such as the two examples shown in figure 4, $\Delta P_{\rm b}$ changes as the bubble advances quasi-statically through the contraction.

The first part of any contraction can always be approximated by a circle with an arc angle which is the local tapering angle $\theta_{\rm t}$. As the right contact line $x_{\rm R}$ just enters the contraction, equation (16) can be expanded to first order in $\theta_{\rm t}$ yielding

$$\Delta P_{\rm b} \approx \frac{2\sigma_{\rm lg}\sin\theta}{R}\,\theta_{\rm t} > 0. \qquad (17)$$

Thus initially the bubble tends to move spontaneously into the contraction. The physical reason for this is that the local tapering angle allows the meniscus to flatten a little, which reduces the costly gas–liquid interface energy.

Once the bubble moves inside the contraction defined in figure 1, a complicated interplay between the initial bubble length L_0, the contact angle θ, the channel radii $r(x_{\rm L})$ and $r(x_{\rm R})$ at the contact lines and the local tapering angle $\theta_{\rm t}(x)$ decides whether bubble clogging occurs or not. We classify our systems into two main classes:

Class α comprises all cases where no clogging occurs, i.e. where the bubble can move spontaneously through the contraction without applying an external pressure.

Class β contains all cases with clogging, i.e. where $\Delta P_{\rm b} < 0$ at some point or, equivalently, where $P_{\rm clog} > 0$.

For class β four sub-classes can be identified depending on where the bubble is when $\Delta P_{\rm b}$ becomes negative and clogging occurs. This bubble position is classified by the position of the contact lines $x_{\rm L}$ and $x_{\rm R}$ relative to the beginning x_1 and the end x_2 of the contraction region (see figures 1 and 4):

$$\begin{array}{lrcl} \text{class } \beta_1: & x_{\rm L} < x_1 & \text{and} & x_1 < x_{\rm R} < x_2, \\ \text{class } \beta_2: & x_1 < x_{\rm L} < x_2 & \text{and} & x_1 < x_{\rm R} < x_2, \\ \text{class } \beta_3: & x_1 < x_{\rm L} < x_2 & \text{and} & x_2 < x_{\rm R}, \\ \text{class } \beta_4: & x_{\rm L} < x_1 & \text{and} & x_2 < x_{\rm R}. \end{array} \qquad (18)$$

A detailed analysis of equation (16) yields important relations for some of the clogging classes.

Table 1. Physical parameters for air bubbles in water flowing through PMMA microchannels.

Parameter values	Reference
$\sigma_{lg} = 72.5 \times 10^{-3}\,\mathrm{J\,m^{-2}}$	[21]
$\sigma_{sg} = 38.9 \times 10^{-3}\,\mathrm{J\,m^{-2}}$	[21]
$\sigma_{sl} = 16.5 \times 10^{-3}\,\mathrm{J\,m^{-2}}$	[21]
$\theta = 72^{\circ}$	[18]

A β_2 clogging only occurs if the bubble can move entirely within the tapered region as shown in figure 4(a), and if at some point it has a length $L = x_L - x_R$ such that

$$L > \frac{r(x_L)}{\tan\theta_t}\left[1 - \frac{\cos(\theta - \theta_t)}{\cos(\theta + \theta_t)}\right]. \tag{19}$$

In β_4 where the bubble in fact spans the entire contraction as sketched in figure 4(b), there is always clogging and the clogging pressure is maximal. The value for ΔP_b is negative and independent of the shape of the contraction. From equation (16) we get

$$\Delta P_b = 2\sigma_{lg}\cos\theta\left(\frac{1}{R} - \frac{1}{r}\right) < 0. \tag{20}$$

The nonclogging class α will in general occur if the bubble is small enough. According to the class β_4 analysis a necessary (but not sufficient) condition for avoiding clogging is that the bubble is small enough to be completely contained in the contraction region. An analysis of the β_2 and β_3 classes shows
Q1 that it should also be short enough to avoid clogging while the left meniscus is still in the tapered region. The β_1 class furthermore puts upper limits on tapering angles that allow for clog-free flow. Examples from class α and β_4 are treated further by detailed numerical analysis in sections 5.2 and 5.3.

5. Numerical simulations

To illustrate the analysis given above a detailed simulation is made in the following. The aim is to minimize the clogging
Q2 pressure ΔP_b with respect to a given parameter. We are limiting our analysis so that the variation comprises only one parameter: the tapering angle θ_t.

5.1. The numerical algorithm

In order to find the force and clogging pressure acting on a large bubble for a given geometry, a semianalytical model of the contracting channel is implemented in MatLab. A numerical Romberg integration scheme is used together with a Newton solver to determine the location of the right and left contacts line (x_R and x_L) for a given position of the center of mass coordinate x_{cm}. The respective interface areas A_i are then found. For a specific geometry defined through $r(x)$, the maximal force is found through equations (5) and (6) and the pressure drop ΔP_b is found through equation (16). The heaviest calculation ran for approximately 4 h on a standard PC.

To be specific we use the geometry defined in figure 1 and take PMMA as the solid material, water as the liquid and air as the gas. This configuration has the physical parameters given in table 1.

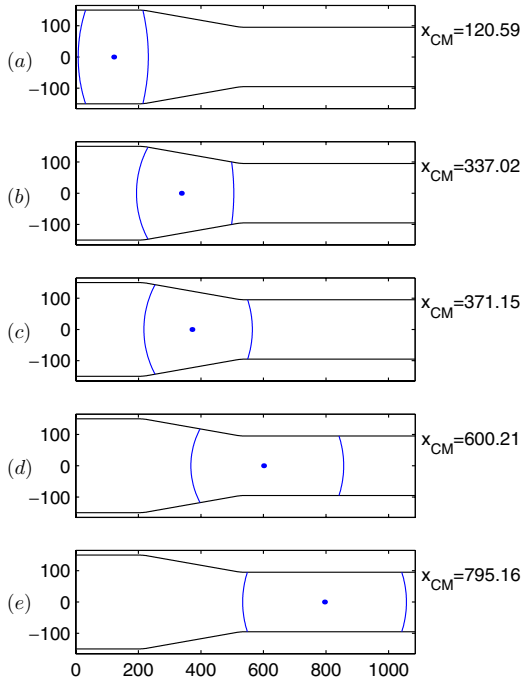

Figure 5. Five positions (a)–(e) of a large bubble with $\gamma = 1.02$ inside a 1000 μm long hydrophilic channel with a tapering angle $\theta_t = 10^{\circ}$. The black dots indicate x_{cm}. The contact angle is $\theta = 72^{\circ}$.

5.2. A specific system without clogging, class α

The first example is the system with a bubble placed in a relatively gentle contraction depicted in figure 5. The total length of the channel is 1000 μm. The wide straight channel to the left has a radius $R = 150$ μm and length 200 μm. The contraction has a length $x_2 - x_1 = 350$ μm and circle arc lengths of 30 μm, which results in a tapering angle $\theta_t = 10^{\circ}$. The narrow straight channel to the left has a radius $r = 95$ μm and length 500 μm. The bubble starts out in the wide channel to the left. It has a relative volume of $\gamma = 1.02$ (cf section 3) and an initial length $L_0 = 180$ μm.

Figure 5 shows the bubble at five different positions (a)–(e). As the bubble advances through the channel it is seen how its length $x_R - x_L$ changes and how the curvatures of the menisci vary. The black dots inside the bubble indicate the center of mass x_{cm}.

In figure 6(a) the total internal energy of the system is plotted as a function of center of mass position x_{cm}. The zero point of the energy is chosen as the energy of the system when the entire bubble is positioned completely within the narrow part of the channel. The five positions (a)–(e) in figure 5 are also marked here.

It is seen that the energy decreases monotonically. This means that without a negative external pressure holding it back, it would move spontaneously through the channel from the left to the right. As long as the bubble moves completely within the wide part of the channel, the energy is constant (about 4 nJ). Then as the right edge enters the contraction, position (a), the energy drops rapidly in accordance with the pressure drop equation (17). This trend continues as the entire bubble moves inside the contraction, as is the case in position (b). The energy continues to drop, but now less rapidly, as the right edge of the

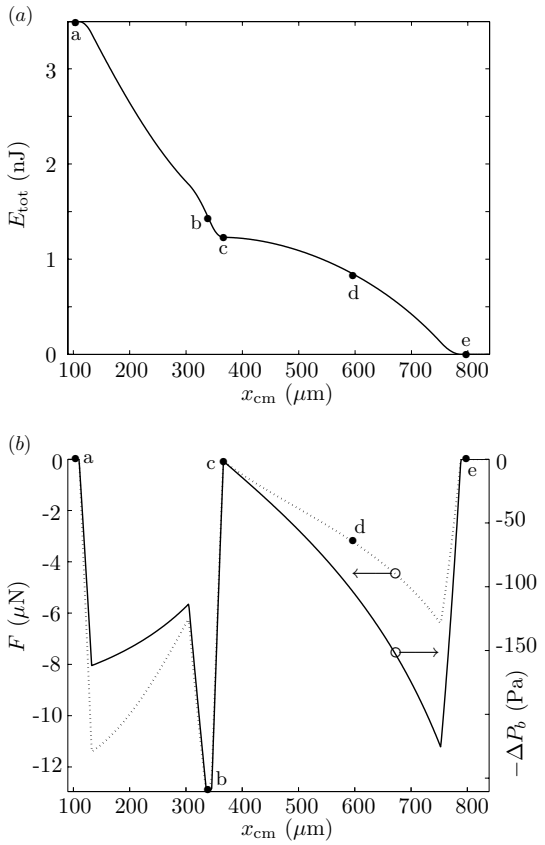

Figure 6. (*a*) A plot of the total internal energy $E_{\rm tot}$ versus the center of mass coordinate $x_{\rm cm}$ for the same bubble as in figure 5. (*b*) The balancing external force F and the pressure drop across the bubble $\Delta P_{\rm b}$ versus $x_{\rm cm}$. The five dots correspond to the five bubble positions in figure 5. Note that $-\Delta P_{\rm b} < 0$ for all positions, i.e. no clogging occurs (a class α system).

bubble enters the narrow channel, see position (*c*). However, as the left bubble edge approaches the narrow channel, the energy drop picks up again, see position (*d*). Finally, the bubble moves completely inside the narrow section and the energy becomes zero (per definition), see position (*e*).

In figure 6(*b*) the corresponding balancing external force F from equation (6), and the clogging pressure across the bubble $-\Delta P_{\rm b}$, equation (16), are plotted as functions of $x_{\rm cm}$. The balancing external force is seen to be negative, which means that to maintain the bubble at quasi-static equilibrium, it is necessary to hold it back. Without this force, the bubble would of course, as mentioned above, move spontaneously toward the narrow segment. At position (*c*) where the right edge of the bubble enters the narrow channel, both force and pressure reach local maxima, but even here they are both negative. No clogging occurs in this system, and it therefore belongs to class α as defined in section 4.

5.3. A specific channel with clogging, class β_4

The second example is nearly the same as the first. Only the length of the contraction region has been reduced from 350 μm to 180 μm. This leads to an increase of the tapering angle from 10° to $\theta_{\rm t} = 20°$. In figure 7 four positions (*a*)–(*d*) of the large bubble are depicted. Note that since $\theta + \theta_{\rm t} = 92°$,

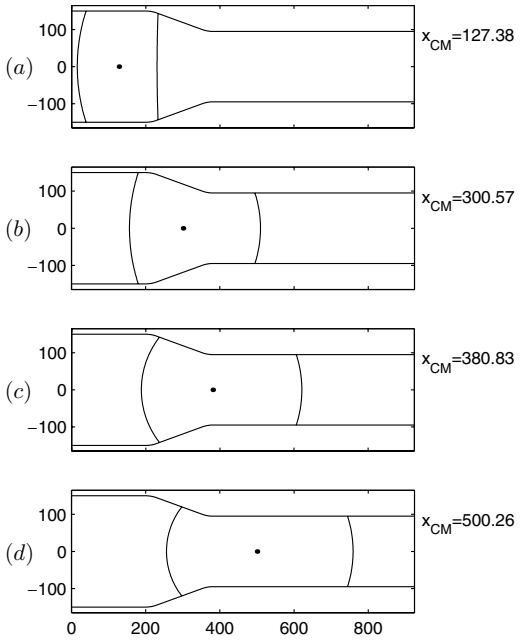

Figure 7. Four positions (*a*)–(*d*) of a bubble with $\gamma = 1.02$ inside a 1000 μm long hydrophilic channel with the tapering angle $\theta_{\rm t} = 20°$. The black dots indicate $x_{\rm cm}$. The contact angle is $\theta = 72°$.

the right meniscus in the tapered section of the channel in panel (*a*) is nearly flat. In fact it has a slight inward bend.

In figure 8(*a*) the energy is shown as a function of $x_{\rm cm}$. The four positions (*a*)–(*d*) are also marked. We immediately note a qualitative difference between this graph and that in figure 6(*a*). The energy no longer drops monotonically but exhibits a marked increase between positions (*b*) and (*c*). This corresponds to the case where the bubble spans the entire contraction, i.e. the left bubble edge is still in the wide channel segment when the right edge enters the narrow segment.

This effect is of course also visible in figure 8(*b*) where the balancing external force F and the clogging pressure $-\Delta P_{\rm b}$ are plotted as functions of $x_{\rm cm}$. Around position (*b*) both F and $-\Delta P_{\rm b}$ become positive, which means that external pressure forces need to be applied to move the bubble through the system. Using equation (20) the clogging pressure is found to be 173 Pa. Without this external force the bubble would tend to move backwards out of the channel, i.e. the system is clogging, and in fact it is an example of class β_4 clogging. Q3

5.4. Clogging pressure versus tapering angle θ_t

The previous two examples showed the behavior for a particular channel contraction from $R = 150\,\mu$m to $r = 95\,\mu$m with tapering angles $\theta_{\rm t} = 10°$ and 20°, respectively. We now extend this analysis to the entire interval $0° < \theta_{\rm t} < 60°$. For each tapering angle we calculate the maximal external force F and the clogging pressure $P_{\rm clog}$. The result is shown in figure 9.

The graph clearly shows that some tapering angles ease the passage of bubbles. For the geometrical configuration defined by $R = 150\,\mu$m, $r = 95\,\mu$m and $C = 30\,\mu$m a small window, the interval $9.5° < \theta_{\rm t} < 11°$, with optimal tapering angles can

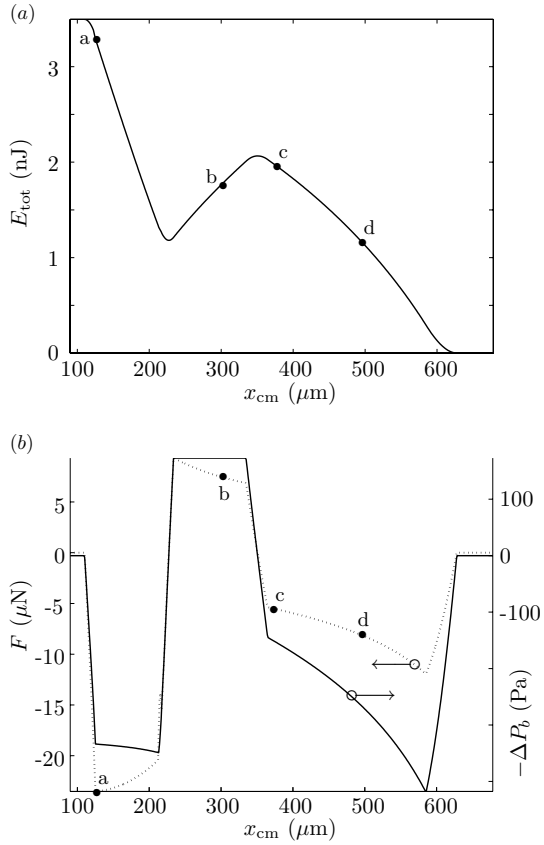

Figure 8. (*a*) A plot of the total internal energy $E_{\rm tot}$ versus the center of mass coordinate $x_{\rm cm}$ for the same bubble as in figure 7. (*b*) The balancing external force F and the pressure drop across the bubble $\Delta P_{\rm b}$ versus $x_{\rm cm}$. The four dots correspond to the four bubble positions in figure 7. Note that $-\Delta P_{\rm b} > 0$ for $x_{\rm cm}$ around 300 μm, i.e. clogging occurs (a class β system).

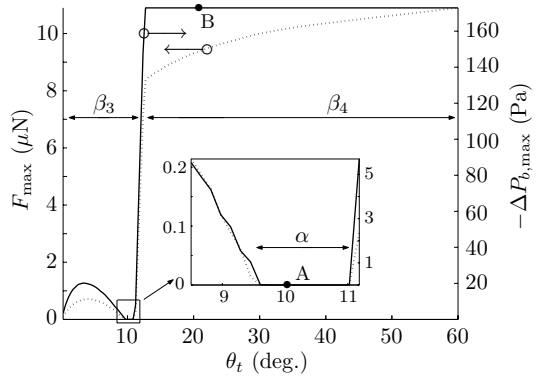

Figure 9. The maximal balancing force $F_{\rm max}$ and clogging pressure $P_{\rm clog} = -\Delta P_{\rm b,max}$ plotted as functions of the tapering angle $\theta_{\rm t}$. Detailed figures illustrating the situation for $\theta_{\rm t} = 10^\circ$ (marked A) are given in figures 6(*a*) and (*b*), and for $\theta_{\rm t} = 20^\circ$ (marked B) in figures 8(*a*) and (*b*). The β_3, β_4 and α classes are described in section 4. The maximal clogging pressure occurs in class β_4. It is found by equation (20) to be $P_{\rm clog} = 173$ Pa.

be identified. In this window $P_{\rm clog} < 0$ corresponding to the clogging-free class α behavior.

For angles greater than about 11° the maximal force is seen to increase dramatically. This transition corresponds to a configuration where the bubble can span the entire contraction region, i.e. class β_4. We clearly see that once the bubble is able to span the entire contraction, the specific geometry of the contraction (in this case the tapering angle) plays no role. We get the same clogging pressure, $P_{\rm clog} = 173$ Pa.

Finally, we note, that class β_3 behavior sets in for small tapering angles below 9.5°. A small clogging pressure is observed, less than 30 Pa.

6. Conclusion

The effects of geometry on the quasi-static motion of large bubbles through a hydrophilic microchannel (capillary) contraction are modeled. The simplicity of the model leads to a good physical understanding of bubble clogging. We have shown that in most cases it requires energy to move a bubble from a wide to a narrow channel. However, we have also found that certain bubble sizes and specific channel geometries lead to a gain in energy.

We have specifically studied the contractions where such an energy gain is achieved. Using the central equation for the pressure drop $\Delta P_{\rm b}$ across the bubble, equation (16), we analyzed a specific contracting axisymmetric hydrophilic channel, and we identified four different classes, denoted as β_1 to β_4, leading to bubble clogging, and one clogging-free class denoted as α. The details of the analysis are quite complicated due to the large number of parameters: the tapering angle $\theta_{\rm t}$, the contact angle θ, the initial bubble length L_0, the radii R and r of the wide and narrow channel segments, etc. However, one general trend is clear. The tendency for clogging increases as the bubbles become larger.

Based on our analysis, some important design rules can be established for making microchannel contractions with minimal or even vanishing clogging pressures. These rules only apply for channel contractions where the energy is lowest in the narrow part.

First, if the typical size L_0 of the bubbles present in the microfluidic system is known, it is important to design contractions which are larger than L_0. The highest clogging pressures occur namely for bubbles spanning the entire contraction, the so-called β_4 class.

Second, the combined effect of the tapering angle and contact angle has to be taken into account to make sure that L_0 is shorter than the critical length leading to clogging of class β_2 being entirely within the tapered region.

Third (not presented here), to smoothen out and lower any unavoidable positive clogging pressure, it helps to make the curved parts of the contraction as large as possible, thus decreasing their curvature.

The method of analyzing the bubble clogging problem in microchannels presented in this paper is very general. It is straightforward to extend it to other geometries (such as nonmonotonic contractions) and to hydrophobic microchannels. With the presented design rules at hand it is possible to design a system that may filter or sort bubbles of different volumes—one simply places contractions with different tapering angles in properly arranged series. A comparable system designed to sort bubbles is presented in [17]. The model may also be extended to include wetting layers as used in [16], and it may be used to model two phase

flows in porous media as in [22, 23]. Some of the dynamical effects such as those briefly mentioned in the introduction may be included as well.

Acknowledgments

This work is partly supported by the Danish Technical Research Council, μTAS Frame Program Grant no 26-00-0220.

References

[1] Gravesen P, Branebjerg J and Søndergård Jensen O 1993 *J. Micromech. Microeng.* **3** 168
[2] Elwenspoek M, Kannerubj T S, Miyake R and Fluitman J H J 1994 *J. Micromech. Microeng.* **4** 227
[3] Jensen M J, Goranović G and Bruus H 2003 *Proc. NanoTech 2003* (*San Francisco, USA, Feb. 2003*) vol 1 258–61
[4] de Gennes P G 1985 *Rev. Mod. Phys.* **57** 827
[5] Brochard-Wyart F and de Gennes P G 1992 *Adv. Colloid Interface Sci.* **39** 1
[6] Stoev K, Ramé E, Leonhardt T and Garoff S 1998 *Phys. Fluids* **10** 1793
[7] Raphaël E and de Gennes P G 1989 *J. Chem. Phys.* **90** 7577
[8] Dussan E B, Ramé V E and Garoff S 1991 *J. Fluid Mech.* **230** 97
[9] de Gennes P G, Hua X and Levinson P 1990 *J. Fluid Mech.* **212** 55
[10] Pismen L M and Rubinstein B Y 2001 *Langmuir* **17** 5265
[11] Tenan M A, Hackwood S and Beni G 1982 *J. Appl. Phys.* **53** 6687
[12] Parlange J-Y 1983 *J. Appl. Phys.* **54** 6744
[13] Schwartz A M, Rader C A and Huey E 1964 *Adv. Chem. Ser.* vol 43 ed R F Gould (Washington, DC: American Chemical Society) p 250
[14] Bretherton F P 1961 *J. Fluid Mech.* **10** 97
[15] Ratulowski J and Chang H -C 1989 *Phys. Fluids* A **1** 97
[16] Bico J and Quéré D 2002 *J. Fluid Mech.* **467** 101
[17] Tordeux C and Fournier J -B 2002 *Europhys. Lett.* **60** 875
[18] Adamson A W and Gast A P 1997 *Physical Chemistry of Surfaces* 6th edn (New York: Wiley)
[19] Probstein R F 1994 *Physiochemical Hydrodynamics: An Introduction* 2nd edn (New York: Wiley)
[20] Batchelor G K 2000 *An Introduction to Fluid Dynamics* (Cambridge: Cambridge University Press)
[21] Jańczuk B, Bialopiotrowicz T and Zdziennicka A 1999 *J. Colloid Interface Sci.* **211** 96
[22] Zha F F, Fane A G, Fall C J D and Schofield R W 1992 *J. Membr. Sci.* **75** 69
[23] Bear J 1998 *Dynamics of Fluids in Porous Media* (New York: Dover)

Appendix D

Paper published in Proc. microTAS 2002

Title
Dynamics of bubbles in microchannels

Authors
Mads Jakob Jensen, Goran Goranović, and Henrik Bruus

Reference
microTAS 2002, Nara, Japan, November 2002, proc. vol. 2, p. 733-735

DYNAMICS OF BUBBLES IN MICROCHANNELS

Mads Jakob Jensen, Goran Goranović, and Henrik Bruus
Mikroelektronik Centret, Technical University of Denmark, DK-2800 Lyngby
(group web-page: www.mic.dtu.dk/research/MIFTS)

Abstract
We present a thorough theoretical study of quasi-static motion and dynamics of bubbles in microchannels. We investigate the effects of geometry and surface physics on the behavior of bubbles, and we propose a set of design rules to minimize the clogging of the channels by bubbles.

Keywords: bubble dynamics, microchannels, CFD simulations

1. Introduction

Due to the large surface to volume ratio, surface effects become very pronounced and even dominant in microchannels. One important example is the formation of gas bubbles in microfluidic systems. Such bubbles present a significant problem: they can block the microchannels, disrupt the flow, and disturb measurements in an uncontrolled manner. For that reason, the sample liquids are usually pretreated by various methods before they enter a microfluidic chip. Examples of pretreatment methods are degassing, control of surface tension or high-frequency sound vibrations. However, in spite of such efforts gas bubbles may still be present, and once there it often requires large driving pressures to push them out of the system [1].

In this paper, based on the interplay between geometry, surface tension, and contact angle, we propose and analyse two designs: one that eases the motion of big bubbles through contracting microchannels, and one that traps the bubbles aside from the main fluid flow.

2. Theory of bubblemotion in a microchannel constriction

The first design concerns contraction of a channel. In order to push a bubble through the sudden and the tapered contractions shown in Fig. 1(a) and 1(b), respectively, a total pressure drop ΔP_{tot} is needed to overcome the sum of two pressure drops: (1) ΔP_{surf} arising from the solid-gas interface at the walls as well as from the curved liquid-gas surface, and (2) ΔP_{fric} due to friction. For the quasi-static motion studied here, the friction is vanishingly small, and the total pressure drop over the bubble in the sudden contraction and the tapered contraction is given by the surface contribution alone.

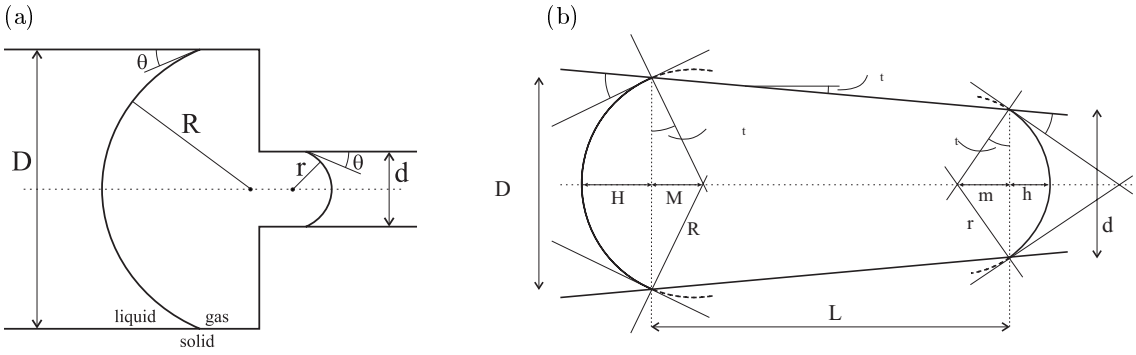

Figure 1: (a) A bubble passing through a sudden contraction. The curvatures at both ends are different and constant while the bubble is in the contraction. (b) A bubble in a tapered channel. Appropriate names have been given to different lengths and angles in use. The curvatures depend on the position of the bubble because of the tapering.

Using two different analytical methods, total energy considerations and the Young-Laplace equation, respectively, we have derived the following expressions for the pressure drop over bubbles in the two constrictions:

$$\Delta P_{\text{surf}}^{\text{sudden}} = 4\sigma \cos\theta \Big(\frac{1}{d} - \frac{1}{D}\Big), \tag{1}$$

$$\Delta P_{\text{surf}}^{\text{tapered}} = 4\sigma \Big(\frac{\cos(\theta + \theta_t)}{d} - \frac{\cos(\theta - \theta_t)}{D}\Big). \tag{2}$$

Here σ is the gas-liquid surface tension and θ is the contact angle describing the influence of the walls on the bubble dynamics. For any taper angle θ_t the driving pressure $\Delta P_{\text{surf}}^{\text{tapered}}$ for the tapered channel is smaller than the driving pressure $\Delta P_{\text{surf}}^{\text{sudden}}$ for the sudden contraction, hence lowering the threshold pressure to drive bubbles out of the contraction. It may thus be beneficial to use tappered constrictions in microfluidic networks where the presense of bubbles poses a problem.

3. A bubbletrap design

Sometimes it is beneficial to collect the bubbles in one place away from the main flow. For this purpose a special passive bubble trap is developed, using a combination of geometry and surface tension effects. Figs. 2a-2d show a 2D CFD simulation of a bubble-trapping process allowing unhindered flow. In a real system, several bubble traps could be placed at locations where there is a tendency of bubble creation. Using special semi-permeable materials (e.g. Gore-Tex), the bubbles could then be extracted from the region and out of the system.

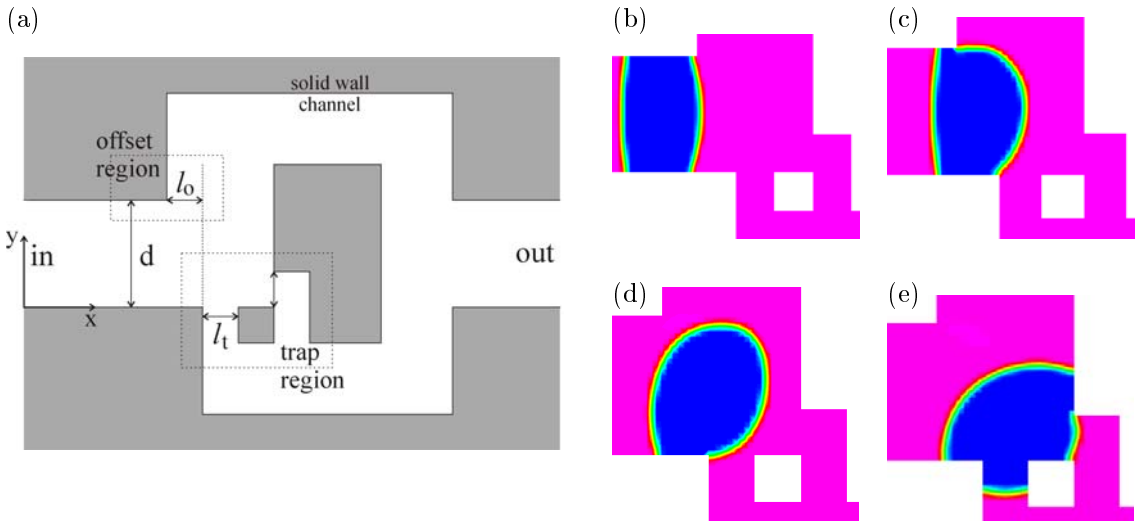

Figure 2: (a) A sketch of the trap geometry where the central length scales are marked: the width d of the main channel, the size l_0 of the offset between the upper and lower wall, and the width l_t of the narrow trapping channels. (b)-(e) Four snapshots of the simulated trapping procedure near the offset and trap regions. (b) A bubble moving towards the offset region. (c) Detaching of one side of the bubble by the offset effect. (d) The bubble is pushed towards the trapping region. (e) The bubble gets trapped.

4. Results and discussion

In our study of bubble dynamics in microchannels, theoretical concepts based on surface tension, geometry, and contact angle are considered. Numerical simulations are performed using commercial software CFD-ACE+ ver. 6.6 containing a specialized Volume-Of-Fluid (VOF) module. They are in good agreement with analytical results and are thus a reliable tool for analyzing bubble behavior in microchannels. The simulation approach is particularly useful for optimization and development of more complicated designs aiming at diminishing the problem of bubbles.

Acknowledgments

We thank our μTAS-colleagues at Mikroelektronik Centret, especially Jörg Kutter, for support and stimulating discussions. This work is partly supported by the Danish Technical Research Council, μTAS Frame Program Grant No. 9901288.

References

[1] P. Gravesen, J. Branebjerg, and O. Søndergård Jensen
J. Micromech Microeng., **3**, 168-182 (1993).

Appendix E

Paper published in Proc. NanoTech 2003

Title
Electroosmotic pumping of nonconducting liquids by viscous drag from a secondary conducting liquid

Authors
Anders Brask, Goran Goranović, and Henrik Bruus

Reference
NanoTech 2003, San Francisco, USA, February 2003, proc. vol. 1, p. 190-193

Electroosmotic Pumping of Nonconducting Liquids by Viscous Drag from a Secondary Conducting Liquid

Anders Brask, Goran Goranović, and Henrik Bruus

Mikroelektronik Centret (MIC), Technical University of Denmark (DTU)
DK-2800 Lyngby, Denmark
abr@mic.dtu.dk

ABSTRACT

A novel electroosmotic pump design relying on two-liquid viscous drag to pump nonconducting liquids is presented and analyzed theoretically. We denoted the pump a two-liquid viscous EOF pump. A conducting pumping liquid driven by electroosmotic flow (EOF) drags a nonconducting working liquid by viscous forces. In particular liquids such as oil, which normally cannot be moved by EOF, may be pumped. This allows for new types of analysis in the field of micro Total Analysis Systems (μTAS) which may prove important in the drug industry and for environmental monitoring. The characteristic flow rate Q and pressure p of the pump is in the range nL/s and kPa, respectively, but depends largely on achievable geometrical dimensions and applied voltage. This paper presents a theoretical and modeling study of the novel design.

Keywords: electroosmotic pump, viscous drag, two-phase flow, circuit modeling, CFD simulation

1 INTRODUCTION

Electroosmotic pumps are suitable for microfluidic applications since (1) they do not have moving parts, (2) they do not produce pulsating flows, and (3) they are easier to integrate. The liquids are pumped by applying an electric field to the electric double layer which forms in the liquid by Debye screening of the immobile charges on the pump walls. In order for such a double layer to form, the liquid needs to have significant electrical conductivity i.e. a sufficiently high concentration of dissociated ions. Nonpolar liquids with very low conductivity ($< 10^{-6}$ S/m), such as oil, cannot form the necessary double layer and therefore cannot be pumped in this way [1]. However, this problem is circumvented in our design by introducing a secondary conducting liquid.

2 DESCRIPTION

The aim is a to have a thin layer of conducting liquid surrounding and dragging the nonconductive liquid. A schematic view of the novel viscous pump is shown in Fig. 1. To realize this we have developed three new features that are essential for the design: pressure valves, reduced flow, and optimized potential drop.

2.1 Pressure Valves

Two pressure valves, the two sets of four narrow channels shown in Fig. 1, prevent the working liquid from entering the electrode reservoirs. The electrode reservoirs are open and thus bubble formation from electrolysis is not a problem. Furthermore the pressure valves allow for placing the pump anywhere in a fluidic network, which is usually not possible. The pressure valves have a width a, and the design utilizes the fact that the electroosmotic flow rate $Q_{\rm eo} \propto a^2$, whereas the hydraulic flow rate $Q_{\rm hyd} \propto a^4$. Hence the pressure driven flow will be effectively reduced for small values of a. Reactive ion etching systems can deliver narrow and deep channels with aspect ratio as high as 40. So if a valve channel is 1 μm wide it can be 40 μm deep.

2.2 Reduced Flow

The flow from the side channels must be reduced compared to that of the main channel in order to enable pumping between Inlet A and Outlet B in Fig. 2. The reduced flow may be obtained in two different ways.

(1) A lower EOF mobility can be present in the pressure valves in comparison to the main channel to optimize the amount of the working liquid going through the pump, see Fig. 1.

(2) A flow reduction can also be achieved by making the channel dimensions so small that the Debye layers overlap. Typically the Debye layers are 1-100 nm wide.

2.3 Electric Potential Drop

One narrow valve channel have a large flow resistance but also a large electrical resistance. This means that the main potential drop would occur in the valve channels and thus not contribute to any pressure build up. The electrical resistance is inversely proportional to the area of the cross section. So by making many short, and narrow channels a low electrical resistance and high hydraulic resistance is obtained.

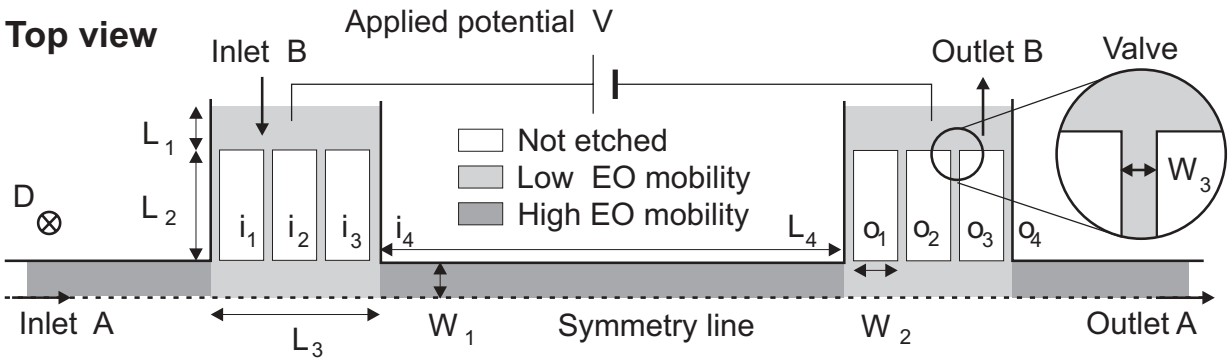

Figure 1: Layout of one half of a two-liquid viscous EOF pump. The pump is mirror-symmetric around the central vertical plane, and only one half is shown. The working liquid A is driven by the pumping liquid, B. The pumping liquid enters at inlet B, goes through the narrow valves, moves along the wall, and exits through the valve and finally through outlet B. The two electrode compartments each have four narrow channels of width W_3. The channels/valves ensure that the working liquid does not enter inlet or outlet B. Two regions with different EO mobilities are identified. The ratio between the mobilities roughly governs the layer thickness of the pumping liquid. The high EO mobility area between the valves is the EO section. The valve regions should be given a coating with low EO mobility.

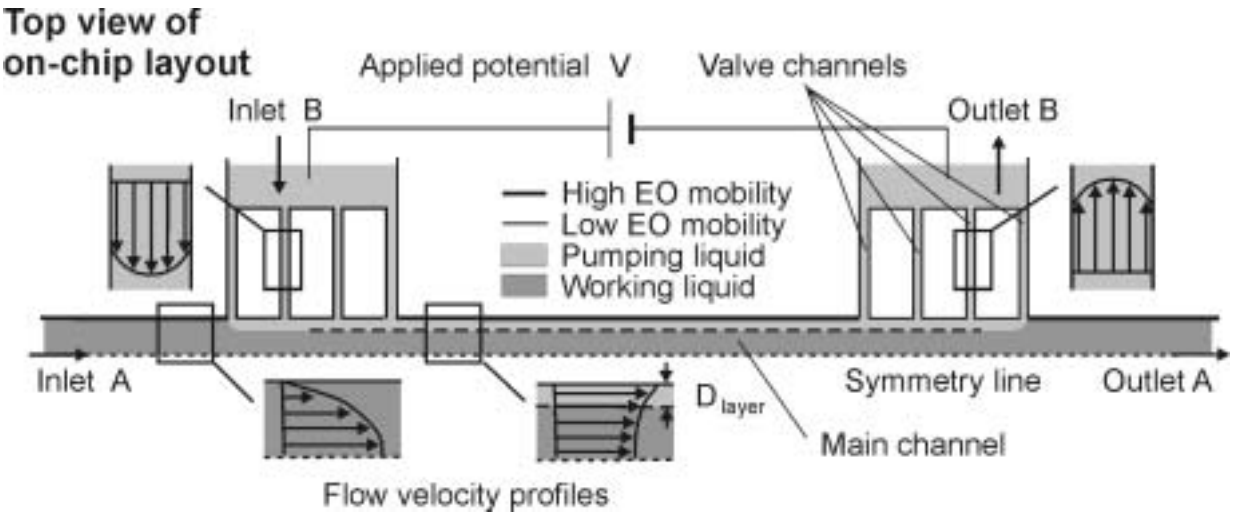

Figure 2: The working liquid is shown in dark gray. It is being dragged by the EOF driven pumping liquid (shown in light gray) that flows along the edge of the main channel. The pump is mirror-symmetric around the central vertical plane, and only one half is shown. The following specific parameters are chosen to predict the performance of the pump. The displayed micro-channels are all etched 40 μm down into the substrate (either siliconoxide or plastic), and after etching the entire structure is closed with a lid. The main channel were the working liquid flows is 150 μm long and 10 μm wide. The narrow valve channels are 1 μm wide and 42 μm long. The uncoated walls are marked as the thick edges of the main channel. Coated walls are marked with thin edges (see also Fig. 1).

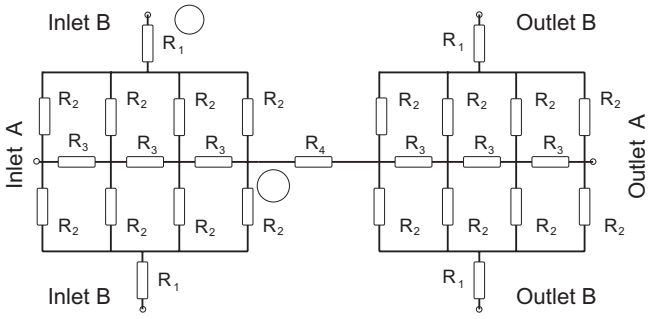

Figure 3: The equivalent electric circuit of the two-liquid viscous EOF pump. Note that the whole pump/circuit is depicted. The overall resistance is calculated as $R_{\text{total}} = 2R_{\alpha\beta} + R_4$, where $R_{\alpha\beta}$ is the electrical resistance between node point α and β. R_4 is the resistance of the EO section.

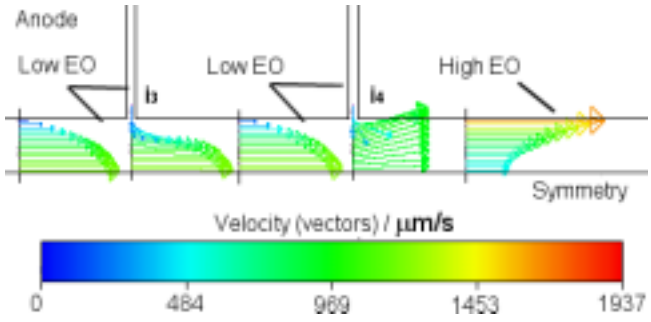

Figure 4: The velocity field in the pump near inlet B calculated by use of CFD. The velocity vectors are positioned in the symmetry plane. The transition from pressure driven flow to EOF is clear: in the regions with low EO mobility, the flow profile is a positive parabolic, but after the last junction, inlet i_4, the EOF drags the liquid, which results in a negative parabolic profile.

2.4 Flow Profiles

The resulting flow will be a superposition of an EOF and a pressure driven flow. Since the Debye layer is roughly 10^4 times smaller than the total width of the channel, we do not resolve it in the following modeling of the pump. The EO velocity appears simply as a non-zero velocity u_{eo} at the walls. In the absence of any backpressure the velocity would simply be constant u_{eo} across the channel. However the presence of pressure gradients induces the characteristic parabolic velocity profiles in the laminar regime, $Re \sim 0.01$. For such low Reynolds numbers the flow is said to be creeping, i.e., inertia can be neglected. Some velocity profiles are shown in Fig. 2. A characteristic feature for creeping flow is that it is free of vorticity. This means that the valve channels may be positioned perpendicular to the main channel without generating any eddies. For a more detailed discussion see Ref. [2].

3 RESULTS

We have analyzed the performance of the pump using two methods. The pressure and flow rates have been calculated by equivalent circuit theory, and in addition, a set of computational fluid dynamics (CFD) simulations was carried yielding more detailed information about the distribution of pressures and velocities. The two methods, which yield the same results within a few percent, were applied to the cases of both immiscible and miscible liquids.

3.1 Equivalent Circuit Model

The aim is to establish a model that can predict the Q-p characteristic. In this respect, the pumping layer thickness, D_{layer}, is important. The EOF depends on the electric field, which depends on the flow in the case of different conductivities. A rigorous model of the two-liquid pump is therefore a complex matter. In this context only an outline will be presented.

The first step is to find the effective potential drop across the EO section. The procedure is to analyze the equivalent electric circuit shown in Fig. 3. The result is that 52% of the applied voltage is dropped over the EO section, R_4 in Fig. 3.

The next step is to find the hydraulic resistance R_{hyd} of each of the channel segments. The channel cross sections are all rectangular with width W and height H. The channel length is denoted L.

$$R_{\text{hyd}} = 12\mu L \left\{ H^3 W - \frac{192}{\pi^5} H^4 \times \sum_{m=0}^{\infty} (2m+1)^{-5} \tanh\left[\frac{(2m+1)\pi W}{2H}\right] \right\}^{-1}, \quad (1)$$

where μ is the dynamic viscosity. R_{hyd} is calculated using Eq. (1), remembering that there are four channels in the valves. For the present geometry, the overall hydraulic resistance of the valves is 26 times larger than that of the EO section, implying that the unintended cross flow is small.

The electroosmotic pressure buildup Δp_{eo} is given by

$$\Delta p_{\text{eo}} = \alpha_{\text{eo}} V_{\text{eff}} R^{\text{eo}}_{\text{hyd}} \frac{HW}{L}, \quad (2)$$

where α_{eo} is the electroosmotic mobility, V_{eff} the effective potential drop, and $R^{\text{eo}}_{\text{hyd}}$ the hydraulic resistance of the EO section. In Eq. (2) the Debye layer is assumed infinity thin.

3.2 Computational Fluid Dynamics

To obtain more detailed information a more advanced tool such as CFD is advantageous. The presented simulations are made with Coventor 2001.3. The program

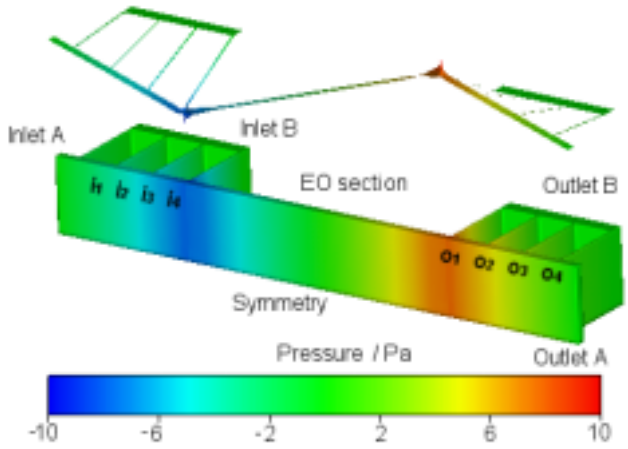

Figure 5: Visualization of the pressure distribution. The floating figure above the pump also displays the pressure. The float shows that the pressure varies linearly from junction to junction, implying uniform flow. There are no external pressure difference. So the pressure gradients originate from internal friction in the pump. Parameters: dimension as in Fig. 2, $\alpha_{\text{eo}}^{\text{low}} = 5000\ \mu\text{m}^2\ (\text{V s})^{-1}$, $\alpha_{\text{eo}}^{\text{high}} = 50000\ \mu\text{m}^2\ (\text{V s})^{-1}$, $p_{\text{in}} = p_{\text{out}} = 0$, $V = 10$ V.

solves the Laplace equation for the potential and the Navier-Stokes equation for the velocity field.

In Fig. 4 the simulated velocity vectors are shown near the inlets to the main channel i_3 and i_4, see Fig. 1.

If the pumping liquid is chosen to be water the EOF mobility along uncoated walls is typically 0.05 $\text{mm}^2/(\text{V s})$. In the valve channels the walls are coated to lower the EOF mobility by a factor 10. With these parameters numerical simulations yield a maximal flow rate per volt of 0.03 nL/(s V) and a backpressure capacity per volt of 3 Pa/V. The value for the flow rate is specific for the given geometry whereas the backpressure is independent of the length of the pump, refer Eq. (2). Visualizations of the pressure distribution and the streamlines are shown in Figs. 5 and 6 respectively.

4 CONCLUSION

The Q-p characteristic of the two-liquid viscous EOF pump largely depends on the geometrical factors and can be significantly enhanced by advanced etching techniques. The pump still works for miscible liquids, but here the working liquid gets mixed with the pumping liquid.

With these parameters numerical simulations yield a maximal flow rate per volt of 0.03 nL/(s V) and a backpressure capacity per volt of 3 Pa/V. These values are quite small and the pump is therefore suited for precise flow manipulation rather than pumping bulk volumes.

Future work involves time dependent two-phase simulations. Such work could perhaps give valuable information about stability and position of the pumping layer, and how to make the initial filling of the pump. Finally a prototype should be manufactured. Because of the possibility to pump all types of liquids in a precise and controlled manner, the described concept seems very promising.

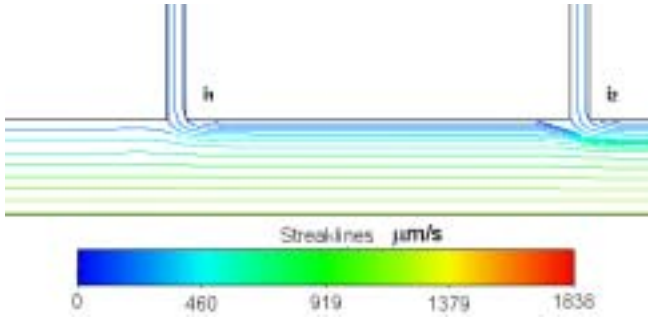

Figure 6: Streamlines at the anode junctions. Even though the channels are orthogonal, the lamination is clear. The Reynolds number is very small $Re \sim 0.01$, thus indicating creeping flow. In the case of immiscible two-liquid flow, the expected pumping layer thickness would be about 20% of the half-width. Please note that the figure is composed of three figures, so the density of the streamlines is not meaningful. The parameters are as in Fig. 5.

5 ACKNOWLEDGEMENTS

This work is partly supported by the Danish Technical Research Council, μTAS Frame Program Grant No. 9901288.

REFERENCES

[1] C.H. Chen, S. Zeng, J. C. Mikkelsen, and J. G. Santiago, "Development of planar electrokinetic micropump", ASME International Mechanical Engineering Congress and Exposition, Orlando, FL, Nov. 7, 2000.

[2] N. A. Patankar and H. H. Hu, Analytical Chemistry, 70, pp. 1870-1881, 1998.

Chapter 1

Introduction

Microfluidics is fluid dynamics on the micrometer (10^{-6} m) scale. A microfluidic system has at least one characteristic length of that order.

The revival of microfluidics began in early '90s with the attempts to miniaturize systems for use in analytical chemistry. The terms lab-on-chip or μTAS (micro-Total-Analysis-Systems) emerged indicating the trend of shrinkage in bio/chemical sciences, as well as the intention to make *integrated* systems capable of performing desirable analyses. The integration has, however, brought forward a whole spectrum of problems and the need for a true multidisciplinary research involving process specialists, chemists, biologists, material scientists and physicists.

In such a colorful community, it is not surprising that microfluidics is many times regarded, erroneously, as a new field. The fundamentals of microfluidics have been laid in 19th century with works of Stokes, Rayleigh and others. The true novelty, however, lies in application prospects which are indeed wide, in particular within the fields of environmental and medical monitoring.

The accent in this report will be put on understanding how do electric fields couple to hydrodynamics in microfluidic regime. Also, various aspects of two-fluid interfaces in microfluidic devices will be examined. Both fundamental (theory) and applied (simulation) angles will be shown. In combination, the two approaches lead to a good understanding of microfluidic systems.

In Chap. 2 a descriptive overview of the features of microfluidic systems is given, after which the fundamental flow equations and relevant dimensionless numbers follow.

In Chap. 3 the microscopic theory of the electroosmotic flow is presented on a thorough, but introductory level. EOF is the driving principle behind electroosmotic pumps. The advanced topics of non-equilibrium thermodynamics are out of the scope of this report.

In Chap. 4 examples are described of how two-fluid systems behave in microsystems and can be advantageously applied: miscible streams in case of micro cell-sorters, bubble behavior in microchannels, and particularly interesting viscous-drag between two immiscible liquids.

Chap. 5 gives a general, in depth analysis on the interaction between electric fields and dielectrics. The electric force is described in terms of the Maxwell stress tensor.

Appendix F

Book chapter published by Wiley-VCH 2003

Title
Simulations in microfluidcs

Authors
Goran Goranović, and Henrik Bruus

Reference
Chap. 5 (38 pages, 21 figs., 25 refs.) in
Microsystem Engineering of Lab-on-a-Chip Devices.
Eds. O. Geschke, H. Klank, and P. Telleman, (Wiley-VCH, New York, 2003)

Oliver Geschke, Henning Klank,
Pieter Telleman

WILEY-VCH

Microsystem Engineering of Lab-on-a-Chip Devices

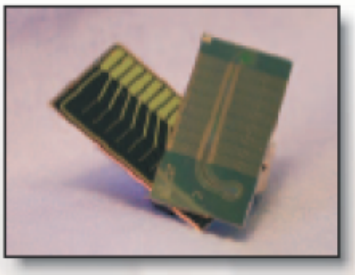

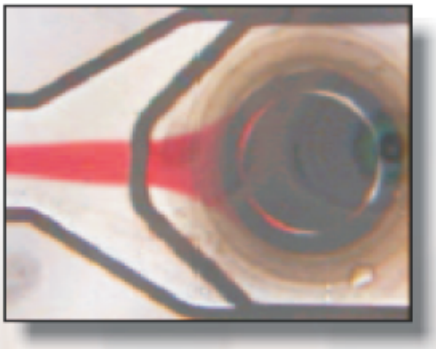

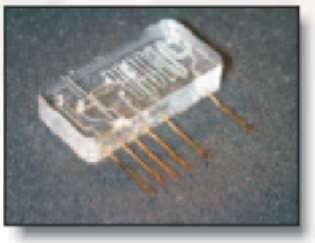

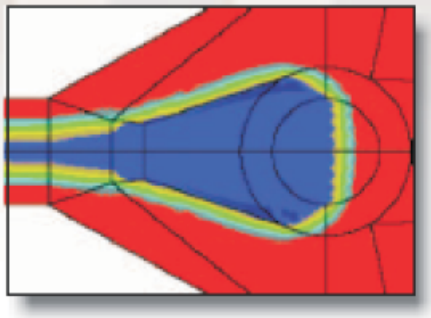

Bibliography

[1] *PIV measurements in a microfluidic 3D-sheathing structure with three-dimensional flow behavior*,
Henning Klank, Goran Goranović, Jörg P. Kutter, Henrik Gjelstrup, Jess Michelsen, Carsten Westergaard,
J. Micromech. Microeng. **12**, 862-869 (2002).

[2] *Integrating advanced functionality in a microfabricated high-throughput flourescent-activated cell sorter*,
A. Wolff, I.R. Perch-Nielsen, U.D. Larsen, P. Friis, G. Goranović, C.R. Poulsen, J.P. Kutter, P. Telleman,
Lab. Chip **3**, 22-27 (2003).

[3] *Theoretical analysis of the low-voltage cascade electroosmotic pump*,
Anders Brask, Goran Goranović, and Henrik Bruus,
Sens. Actuators B Chem. **92**, 127-132 (2003).

[4] *The clogging pressure of bubbles in hydrophilic microchannel contractions*,
Mads Jakob Jensen, Goran Goranović, and Henrik Bruus,
J. Micromech. Microeng. **14** (2004).

[5] *Three-dimensional single step flow sheathing in micro cell sorters*,
Goran Goranović, Ivan R. Perch-Nielsen, Ulrik D. Larsen, Anders Wolff, Jörg P. Kutter, Pieter Telleman,
Proc. MSM 2001, Hilton Head Island (SC) USA, March 2001, p. 242-245.

[6] *Computer modeling as a design tool for microfluidic structures*,
Ivan R. Perch-Nielsen, Goran Goranović, Henning Klank, Ulrik D. Larsen, Anders Wolff, Jörg P. Kutter, Pieter Telleman,
Proc. μTAS 2001, Monterey (CA) USA, October 2001, p. 629-630.

[7] *Characterization of flows in laser-machined polymeric microchannels*,
Goran Goranović, Henning Klank, Carsten Westergaard, Oliver Geschke, Pieter Telleman, and Jörg P. Kutter,
Proc. μTAS 2001, Monterey (CA) USA, October 2001.

[8] *Electroosmotically driven two-liquid viscous pump for nonconducting liquids*,
Anders Brask, Goran Goranović, and Henrik Bruus,
Proc. μTAS 2002, Nara, Japan, November 2002, vol. **1**, p. 45-47.

[9] *The low-voltage cascade EOF pump: comparing theory with published data*,
Anders Brask, Goran Goranović, and Henrik Bruus,
Proc. μTAS 2002, Nara, Japan, November 2002, vol. **1**, p. 79-81.

[10] *Dynamics of bubbles in microchannels*,
Mads Jakob Jensen, Goran Goranović, and Henrik Bruus,
Proc. μTAS 2002, Nara, Japan, November 2002, vol. **2**, p. 733-735.

[11] *Electroosmotic pumping of nonconducting liquids by viscous drag from a secondary conducting liquid*,
Anders Brask, Goran Goranović, and Henrik Bruus,
Proc. NanoTech 2003, San Francisco (CA) USA, March 2003, vol. **1**, p. 190-193.

[12] *Quasi-static motion of bubbles in microchannel contractions*,
Mads Jakob Jensen, Goran Goranović, and Henrik Bruus,
Proc. NanoTech 2003, San Francisco (CA) USA, March 2003, vol. **1**, p. 258-261.

[13] *Simulations in microfluidcs*
Goran Goranović and Henrik Bruus,
Chap. 5 (38 pages, 21 figs., 25 refs.) in *Microsystem Engineering of Lab-on-a-Chip Devices*. Eds. O. Geschke, H. Klank, and P. Telleman, (Wiley-VCH, New York, autumn 2003)

[14] *Fluid Mechanics 2nd edition Course in Theoretical Physics, Volume 6*
L. D. Landau and E. M. Lifshitz
Institue of Physical Problems, USSR Academy of Sciences, Butterworth-Heinemann, 2000

[15] *Classical Electrodynamics Second Edition*
J. D. Jackson
John Wiley and Sons, USA, 1975

[16] *Conditions for Similitude between the Fluid Velocity and Electric Field in Electroosmotic Flow*
E.B. Cummings, S. K. Griffiths, R. H. Nilson, P. H. Paul
Analytical Chemistry, Vol. **72** No. 11, June 1, (2000)

[17] *Principles of electroosmotic pumps*
A. Brask
M.Sc. thesis, MIC, DTU, 2002

[18] *Physicochemical Hydrodynamics, An Introduction 2nd. Edition*
R. F. Probstein
John Wiley and Sons, Massachusetts Institute of Technology, 1994

[19] J. F. Osterle, J. Appl. Mech. **31**, 161 (1964).

[20] C.L. Rice and R. Whitehead, J. Phys. Chem. **69**, 4017 (1965).

[21] A. Manz, C. S. Effenhauser, N. Burggraf, D. J. Harrisson, K. Seiler, and K. Fluri, J. Micromech. Microeng. **4**, 257 (1994).

[22] P. H. Paul, D.W. Arnold, D. J. Rakestraw, *proc. μTAS 1998, Banff, Canada*, p. 49 (1998).

[23] Y. Takamura, H. Onoda, H. Inokuchi, S. Adachi, A. Oki, and Y. Horiike, *proc. μTAS 2001, Monterey CA, USA*, p. 230, J. M. Ramsey and A. van den Berg (eds.), Kluwer Academic Publishers (2001).

[24] W.E. Morf, O.T. Guenat and N.F. de Rooij, Sensor. Actuat. B-Chem. **72**, 266 (2001).

[25] O.T. Guenat, D. Ghiglione, W.E. Morf, and N.F. de Rooij, Sensor. Actuat. B-Chem. **72**, 273 (2001).

[26] S. Zeng, C.-H. Chen, J. C. Mikkelsen Jr., and J. G. Santiago, Sensor. Actuat. B-Chem. **79**, 107 (2001).

[27] D. R. Reyes, D. Lossifidis, P.-A. Auroux, and A. Manz, Anal. Chem. **74**, 2623 (2002).

[28] Experimental parameters not quoted in the original experimental paper were kindly provided by dr. Y. Takamura, Univ. Tokyo.

[29] R.-J. Yang, L.-M. Fu, and Y.-C. Lin J. Colloid Interf. Sci. **239**, 98 (2001).

[30] N. A. Patankar and H. H. Hu, Anal. Chem. **70**, 1870 (1998).

[31] *Zeta Potential of Highly Charged Thin Double-Layer Systems* R. J. Hunter., B. R. Midmore and H. Zhang Journal of Colloid and Interface Science **237**, p. 147-149, 2001.

[32] *Physical Chemistry of Surfaces*
A. W. Adamson and A. P. Gast
John Wiley and Sons, Sixth Edition, 1997

[33] *Micro tools for cell handling*
P. Telleman, et al.
SPIE conference on microfluidic devices and systems, Santa Clara, USA, Sep. 2000,

[34] *Bubble Puzzles*
D. Lohse
Physics Today, February 2003

[35] *Microfluidcs - a review*
P. Gravesen, J. Branebjerg and O. S. Jensen J. Micromech. Microeng. **3**, 1993.

[36] *Transport of Gas Bubbles in Capillaries* J. Ratulowski and H.-C. Chang
Physics of Fluids A **1** (10), American Institute of Physics, October 1989.

[37] *Fluid dynamics for physicists*
T. E. Faber
Cambridge University Press, Cambridge, UK, 2001

[38] *Electrodynamics of continuous media Course in Theoretical Physics, Volume 8*
L. D. Landau and E. M. Lifshitz
Institue of Physical Problems, USSR Academy of Sciences, Pergamon Press, 1960

[39] *Electromagnetic Theory*
J. A. Stratton
McGraw-Hill, USA, 1941

[40] *Statistical Physics 3rd Edition Part 1*
L. D. Landau and E. M. Lifshitz
Institue of Physical Problems, USSR Academy of Sciences, Butterworth-Heinemann, 2001

[41] *Vectors, Tensors and the Basic Equations of Fluid Mechanics*
R. Aris
Prentice-Hall International, London, 1962

[42] *Field-coupled surface waves: a comparative study of surface-coupled electrohydrodynamic and magnetohydrodynamic waves*
J. R. Melcher
M.I.T. Press, Cambridge, Massachusetts, 1963

[43] *Electrohydrodynamic and Magnetohydrodynamic Surface Waves and Instabilities*
J. R. Melcher
Phys. of Fluids, **4**, 11 p. 1348-1354 (1961)

[44] *Introduction to Solid State Physics*
C. Kittel
John Willey and Sons, 6ed, 1986

[45] *Electromagnetic fields and energy*
H. A. Haus, J. R. Melcher
Prentice Hall, Englewood Cliffs, New Jersey, 1989

[46] *Electrohydrodynamics: The Taylor-Melcher Leaky Dielectric Model*
D. A. Saville
Annu. Rev. Fluid Mech., **29** p. 27-64 (1997)

[47] *The Theory of Sound Vol.2*
Lord Rayleigh
Dover New York, 1945

[48] *Disintegration of water drops in an electric field*
G. I. Taylor
Proc. Roy. Soc. A 331 p.263-72 1964

[49] *Hydrodynamic and Hydromagnetic Stability*
S. Chandasekhar
Oxford University Press, 1961

[50] *Hydrodynamic stability*
P.G. Drazin and W. H. Reid
Cambridge University Press, 1991

[51] *On the equilibrium of liquid conducting masses charged with electricity*
Lord Rayleigh
Phil. Mag. Ser. **5** 14 p. 184-86, 1882

[52] *Electrohydrodynamics: a review of the role of interfacial shear stresses*
J. R. Melcher and G. I. Taylor
Annu. rev. Fluid Mech. **1** p.111-46 1969

[53] *An active micro mixer using electrohydrodynamic (EHD) convection*
J. W. Choi, Chong H. Ahn
Solid State Sensor and Actuator Workshop, Hilton Head Island, S. Carolina, 2000

[54] *Electrohydrodynamic Stability of Two Superposed Viscous Fluids*
A. A. Mohammed, E. F. Elshehawey and M. F. El-Sayed
J. Coll. Interf. Sci., **169** p. 65-78 (1995)

[55] *Bubbles in microchannels*
M. J. Jensen
M.Sc. thesis, MIC, DTU, 2002

[56] *Blood flow in microchannels*
L. Bitsch
M.Sc. thesis, MIC, DTU, 2002

[57] *Dispersion in electrokinetically and pressure driven microflows*
F. R. Hansen
M.Sc. thesis, MIC, DTU, 2002

[58] *Micro flows Fundamentals and Simulation*
G. E. Karniadakis and A. Beskok
Springer-Verlag, New York, 2002

[59] *Viscous fluid flow 2nd edition*
F. M. White
McGraw-Hill, Singapore, 1991

[60] *An Introduction to Capillary Electrochromatography* D. B. Keith, M. G. Cikalo and M. M. Robson